Karlsruhe Institute of Technology

Jannis Weinacker

Micro-Optical Elements used for Single-Molecule Raman Spectroscopy and as Scintillators

2024
Dissertation

Micro-Optical Elements used for Single-Molecule Raman Spectroscopy and as Scintillators

Zur Erlangung des akademischen Grades eines
DOKTORS DER NATURWISSENSCHAFTEN
von der KIT-Fakultät für Physik des
Karlsruher Instituts für Technologie (KIT)

genehmigte

DISSERTATION

von

M. Sc. Jannis Weinacker
geboren in Bensheim

Tag der mündlichen Prüfung: 29. November 2024
Referent: Prof. Dr. Martin Wegener
Korreferent: Prof. Dr. Carsten Rockstuhl

Contents

Publications

Parts of this thesis have already been published ...
... in scientific journals:

- **J. Weinacker**[1], S. Kalt[1], P. Kiefer[1], P. Rietz[1], and M. Wegener, "On Iterative Pre-Compensation of 3D Laser-Printed Micro-Optical Components Using Confocal-Optical Microscopy", *Advanced Functional Materials*, 2309356 (2023).

- **J. Weinacker**, B. K. Bhandari, A. V. Rodriguez, C. West, F. De Angelis, F. Tantussi, N. Maccaferri, N. Goldman, and M. Wegener, "A protocol using compact 3D printed micro-optical elements for protein identification from low-intensity amino-acid Raman signals", *Advanced Materials Technologies*, (2024), under review.

- **J. Weinacker**, S. Kalt, A. Huber, N. Gutknecht, J. L. G. Schneider, N. M. Bojanowski, T. Geigle, M. Steidl, and M. Wegener, "Multi-Photon 3D Laser Micro-Printed Plastic Scintillators for Applications in Low-Energy Particle Physics", *Advanced Functional Materials*, 2413215 (2024).

... at scientific conferences (only own presentations):

- **J. Weinacker**, B. K. Bhandari, A. V. Rodriguez, C. West, F. De Angelis, F. Tantussi, N. Maccaferri, N. Goldman, and M. Wegener, "Distinction of low-intensity Raman spectra originating from amino-acids using compact 3D printed micro-optical elements", SPIE Photonics West, scheduled for January 2025.

Additional related work has already been published ...
... in scientific journals:

- R. Zvagelsky, P. Kiefer, **J. Weinacker**, and M. Wegener, "In-situ Quantitative Phase Imaging during Multi-photon Laser Printing", *ACS Photonics* **10**, 2901-2908 (2023).

[1]These authors have contributed equally.

Chapter 1

1 Introduction

When I started to learn about the field of optics, I was fascinated by the amount of control scientists gained over light in many different ways. Starting with mirrors or simple lenses that focus or scatter light and enable the creation of images and photographs, I was surprised by the amount of complexity that was about to follow. Later, I learned about research allowing the controlled generation of single photons [1–4], the shaping of field associated with light beyond the well believed resolution limit [5–9], the tomographic information which are retrievable from data stemming from comparably simple experiments [10–12], and many more examples. Since I wanted to learn more about such fascinating topics, I did the research for my doctoral thesis in the field of optics. I was not disappointed to see my colleagues working on micro-lenses [13], diffractive optical elements that shape light in any desired intensity profile [13, 14], and laser interferometers to measure even the smallest displacements in metamaterials [15], to give only a few examples.

Following the third law of the science fiction author Arthur C. Clarke that "any sufficiently advanced technology is indistinguishable from magic", I must say that this experience comes very close to this statement, and I started to feel like being in a group of wizards of light. I was very happy to contribute my part to this research with the development of micro-optical elements that support the spectroscopic identification of molecules or act as scintillators to enable new possibilities in the detection of high-energy particles.

The spectroscopic identification of molecules is an essential mean in different areas of science, like chemistry [16, 17], biology [18–20], and medical applications [21, 22]. One special case of optical spectroscopy is Raman spectroscopy, which is especially popular due to its minimum invasive measurement technique [23–26]. With modern nano-optical approaches combined with plasmonic enhancement, it is possible to collect spectra of single molecules, like single bases in DNA [27–30] or single amino acids in a protein [31–34]. While it is very desireable to be able to sequence proteins or DNA using Raman spectroscopy, there are still some problems with such experiments. Most relevant is the short excitation time of the molecule itself, which is hard to increase. Thus, the number of emitted signal

photons is very low. In this regards, it becomes necessary to use single-photon detectors, which, on the other hand, come at a higher price, especially for large detector arrays. For this reason, it is natural to try to reduce the number of required detectors. In case of the sequencing of proteins, the number of possible outcomes for each amino acid is limited to 20. Thus, it is not necessary to collect the whole Raman spectrum, but gain only enough information to make a decision on which amino acid is present. Therefore, the number of detectors can be reduced drastically. To improve the performance, each detector collects photons from specific optimized spectral regions of the Raman spectrum. By that, the amount of information gained with a small number of detectors is maximized leading to a low-cost high-speed device for the sequencing of amino acids. The selection of the photons from the different optimized spectral regions is thereby done by a custom made segmented refractive optical element (SROE) which leads to the topic of this thesis. The SROE is designed specifically for this task within a Raman spectrometer and fabricated using two-photon lithography [35] with the benefits of two-photon grayscale lithography [36]. Additionally, optimizations [37] will be performed and test experiments on the capabilities of the SROE will be presented within this thesis.

As another example of micro-optical elements presented within this thesis are 3D micro-printed plastic scintillators. The main difference to the elements mentioned before is that the scintillators generate the light themselves and do not just influence it. In general, plastic scintillators have been used for over 5 decades [38] and are still very popular in particle many fields like collider experiments [39–42], neutrino physics [43–45], or medical applications [46–49]. Despite the lower price in comparison to crystalline scintillators, plastic scintillators have the advantage to be easier to structure in a desired shape. A growing number of applications require structured scintillators [50, 51]. This requirement can be fulfilled by 3D printing plastic scintillators, however, state-of-the-art one-photon based printing approaches [52–54] suffer from an insufficient resolution for some applications [55, 56]. Therefore the first commonly known two-photon printable plastic scintillator is presented enabling the fabrication of scintillator structures with a micro-meter resolution. The development of this resin was motivated by an application within the Karlsruhe tritium neutrino (KATRIN) experiment in which the noise reduction of the detector could be reduced by an active-transverse-energy filter (aTEF) [55].

Outline of this thesis

At the beginning of my thesis, starting with Chapter 2, I will give an overview over the theoretical concepts to describe the refractive micro-optical elements that will later be presented in the following chapters. From the concept of constant optical path lengths for incoming parallel rays that should be focused to a focal point, I will derive the shape of an ideal lens or ‚more precisely, a focusing element that performs this task. Going one step further, I will present a theoretical description of refractive freeform surfaces deflecting parallel incoming rays into different controllable directions. I will solve the resulting partial differential equations to obtain the surface profile which deflects the rays in the desired directions. Last, I will explain the concept and necessary formulas to perform a wave-propagation simulation to verify the performance of the derived surface profiles during this thesis.

In Chapter 3, I show the fabrication routine of the micro-optical elements. Starting with the concept of two-photon printing, including the workflow and all necessary technical terms for understanding and reproduceability, I will next present the concept of two-photon grayscale lithography, which promises better surface qualities. Additionally, I will show an iterative precompensation routine, in which the topography of a printed sample is measured leading to an adaption of the design to reduce systematic deviation in the next print. While this is, strictly speaking, not part of the fabrication itself, I still see this precompensation routine as part of the fabrication for all micro-optical elements due to its simplicity and potential for a significant improvement of the shape accuracy..

In Chapter 4, I will first explain the concept of Raman spectroscopy and how it can be used to identify single amino acids in a protein. I will address the typical problems that arise when doing such experiments, mainly the low number of signal photons. Next, I will show two possibilities on how custom-made micro-optical components can help addressing this issue. First, I will show a micro-lens array that increases the efficiency of the detector by focusing the light on the active areas of the detector array. Second, I will present a segmented refractive optical element, which selects a small number of optimized spectral regions out of the continuous (Raman) spectrum and guides the corresponding light towards individual, highly sensitive, detectors. The optimization of the spectral regions are performed in a way that the amount of information gained by one amino acid is maximized. By that, the efficiency of the amino acid identification can be improved with using only a small number of detectors.

In chapter 5, I will switch to a different class of micro-optical elements generating light intrinsically under the incidence of high-energy electrons. Materials showing this behavior are commonly known as scintillators. In the context of this thesis, I will present a two-photon printable plastic scintillator. At first, I will show the ingredients for a scintillator resist followed by the determination of the print parameters, including the parameters necessary for two-photon grayscale lithography. Afterwards, I will show the characterization of the scintillator's light output qualitatively and quantitatively using a scanning-electron microscope including a photodetector in its chamber. Thus, the light yield of the scintillator is found to be around 930 $\mathrm{photons/MeV}$. Last, I will demonstrate the feasibility of the fabrication of a detector system acting as an active-transverse-energy filter by printing a wall-gird structure out of the scintillator material directly on a single photon avalanche diode array.

Finally, in Chapter 6, I will conclude and summarize the topics presented in the chapters before, followed by a brief outlook on what future research might bring to the corresponding topics.

Chapter 2

2 Theoretical description of refractive optical elements

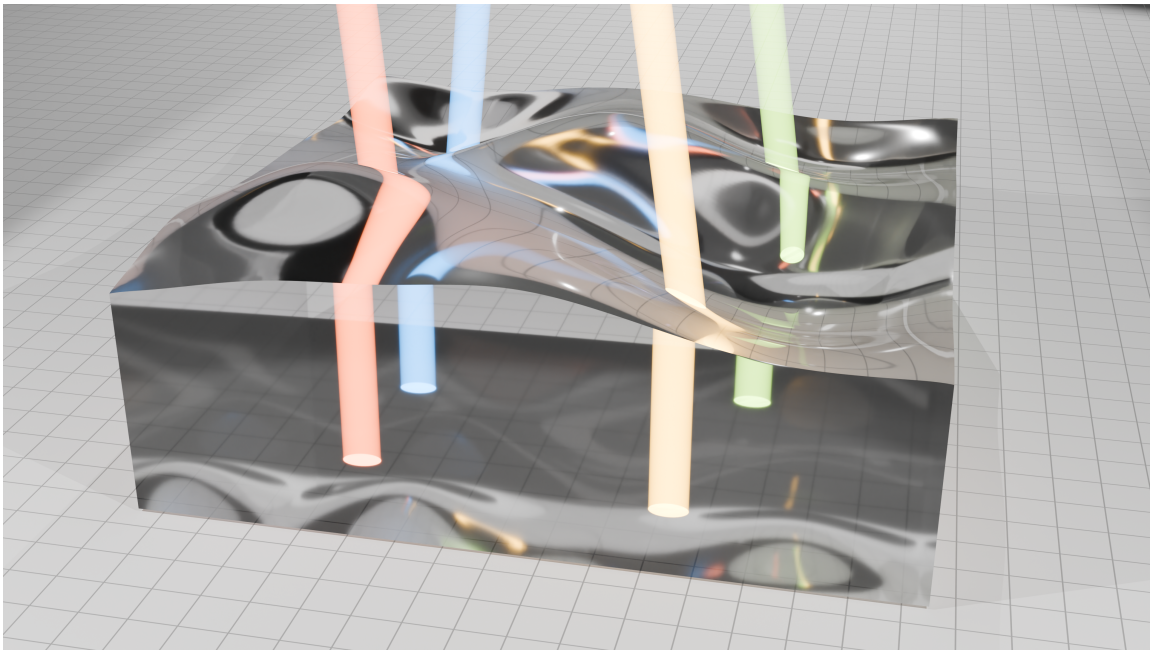

Artistic illustration of a refractive free-form surface deflecting 4 rays in different, controllable directions.

In this chapter, a formalism to describe the relevant refractive optical elements of this thesis is presented. Starting with a simple focusing lens, an equation which calculates the height profile for given geometrical boundary conditions, e.g. the focal length, is be derived based on the concept of constant optical path lengths.
The second approach describes refractive free-form surfaces for directing parallel incident light rays into different, but controllable directions. Here, the surface is calculated based on Snell's law, which delivers, in combination with the geometrical boundaries, a partial differential equation system for the height profile. The solution strategy of this difficult equation system is also discussed and later used for refractive free-form surfaces within this thesis.

2.1 Ideal lenses

One of the most basic refractive optical elements is a focusing lens which is capable of focusing parallel incident rays down to a point, when described in the ray-optics image. To be precisely, a lens is not only capable of focusing incident rays parallel to the optical axis and to a point also on the optical axis. In general, a lens should also be capable to focus rays that hit the lens under an angle to the optical axis. The focus point of these rays should lie at the focal plane too, but with a distance to the optical axis. Since this circumstance is not considered during the derivations, it is not clear, that the presented lens shape is also optimized for this scenario. Most likely, there is a better shape that finds a compromise between focusing rays parallel to the optical axis and rays with a (small) angle with respect to the optical axis. Thus, the presented shape is technically not a lens, but more a focusing element. However, for consistency and simplicity, this circumstance is ignored within this thesis and the focusing element is called lens in the following. In general, despite their simplicity, lenses have a huge number of applications in daily live, e.g. as glasses, and also in science in almost every optical setup. Since in the past fabrication processes were often very complex, simplified but suboptimal surface forms like spherical lenses were used. However, in the recent past, modern technologies like 3D printing enable the easier fabrication of free-form lenses with optimized surface profiles. Especially for the growing interest in micro-lenses and micro-lens arrays [57–64], the boundary condition to spherical lenses is not relevant anymore. Therefore, a derivation is presented in this section explaining how a lens surface is calculated from its geometrical boundaries, like the working distance, focal length, radius, etc.

2.1.1 *Principle of constant optical path-length*

In Figure 2.1a, a sketch of an ideal focusing lens profile is shown focusing two incident rays from the right down to a focal point at position 0. One ray hits the lens exactly at the center position and is, therefore, not deflected. It first travels the distance d inside the lens material and then the back focal length f from the center point of the lens to the focal point. The second ray hits the lens off axis at the coordinate x and travels a shorter distance of $d - (l(x) - f)$ inside the lens, where $l(x)$ is the function that describes the lens profile. When reaching the lens surface, the second ray is deflected so that it hits the focal point as required. The distance, the second ray travels in air, is given by $\sqrt{l(x)^2 + x^2}$. When we assume, that both rays are parallel and in phase on the right side of the image, they have to be also be in phase at the focal point and interfere constructively. This, however, means, that the optical path lengths of both rays from their starting point to the

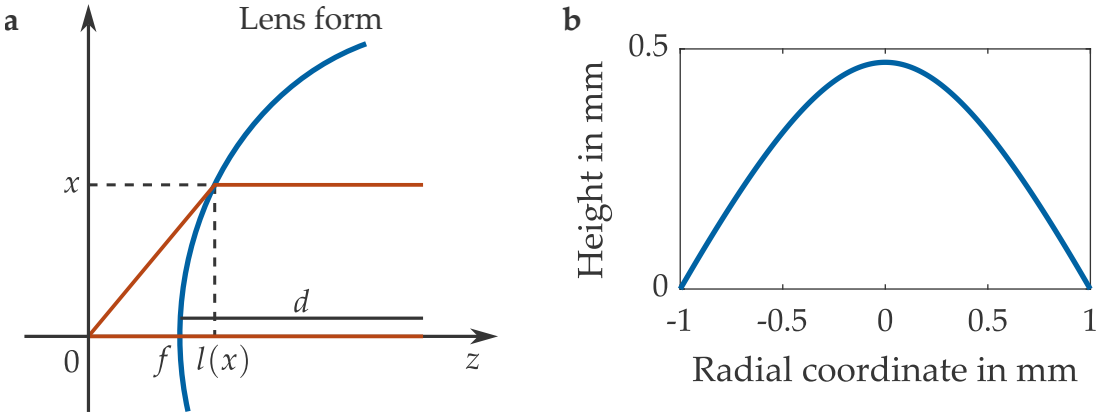

Figure 2.1: Sketch as definition for the geometrical lens parameters to derive an ideal focusing lens shape (**a**). The lens, described by the function $l(x)$, refracts parallel light rays coming from the right onto the focal point in 0. The distance between the focal point and the center point of the lens is the back focal length f. The center ray travels the distance d inside of the lens material before reaching the surface. All other rays inciding at a height x travel a smaller distance inside the lens. In **b**, the curve of an ideal focusing lens with a radius of $r = 1\,\text{mm}$, a refractive index of $n = 1.5$, and a working distance of $\text{WD} = 2\,\text{mm}$ measured from its ground plane, is shown. Panel **a** was adapted from [37].

focal point need to be the same [65]. In form of an equation this means that

$$n(\lambda) \cdot d + f = n(\lambda) \cdot [d - (l(x) - f)] + \sqrt{l(x)^2 + x^2}\,, \tag{2.1}$$

were $n(\lambda)$ describes the refractive index of the lens material which is in general wavelength-dependent. For many applications, the back focal length is not provided. Instead the required working distance WD, measured from the substrate of the lens, and the lens radius r is given. Looking again at Figure 2.1a, this means that $l(r) = \text{WD}$. Putting this into Equation 2.1, we obtain

$$f = \frac{n(\lambda) \cdot \text{WD} - \sqrt{\text{WD}^2 + r^2}}{n(\lambda) - 1}\,. \tag{2.2}$$

This is relevant for the applications presented in this thesis since here the height of the lens is unknown at first, but the distance between the lens substrate and the focal point is given.

2.1.2 *The aspheric lens equation*

Equation 2.1 describes the lens form, however, it is not an explicit formula to calculate the lens profile $l(x)$. While it is possible to derive such an explicit term from the equation, we instead want to apply this solution here to the general aspheric lens equation [66]

$$z(x) = \frac{\rho x^2}{1 + \sqrt{1 - (1+k)(\rho x)^2}}\,, \tag{2.3}$$

where ρ describes the inverse radius of curvature at the center point of the lens and k is the conic constant. To map these parameters with the parameters $n(\lambda)$ and f used before, the first four (implicit) derivatives at $x = 0$ of both equations are compared as follows

1st derivative	$l'(0) = 0$	$z'(0) = 0$
2nd derivative	$l''(0) = \frac{1}{f(n(\lambda)-1)}$	$z''(0) = \rho$
3rd derivative	$l'''(0) = 0$	$z'''(0) = 0$
4th derivative	$l^{(4)}(0) = \frac{3}{f^3(n(\lambda)-1)^3}\left(1 - n(\lambda)^2\right)$	$z^{(4)}(0) = 3\rho^3(1+k)\,.$

(2.4)

These two sets of the first four derivatives are identical if ρ and k fulfill the relations

$$\rho = \frac{1}{f\left(n(\lambda) - 1\right)}\,, \tag{2.5}$$

$$k = -n(\lambda)^2\,. \tag{2.6}$$

With these equations and Equation 2.2, the form of an ideal lens can be calculated when its radius, working distance measured from the substrate, and refractive index are known. One example for the parameters $r = 1\,\text{mm}$, $\text{WD} = 2\,\text{mm}$, and $n = 1.5$ is shown in Figure 2.1b.

2.2 Refractive free-form surfaces

A way more general class of refractive optical elements are refractive free-form surfaces. With refractive free-form surfaces it is, for example, possible to control the angle of deflection for parallel incident rays depending on their lateral coordinate individually. From this point of view, a lens is also a refractive free-form surface, since every ray is deflected in a way, that it reaches the focal point. However, even more complicated deflection functions are possible. In the following, a general approach is presented to calculate a height profile that deflects parallel rays in controllable directions. A similar approach was already developed before [67], but not for a general deflection function for the individual rays.

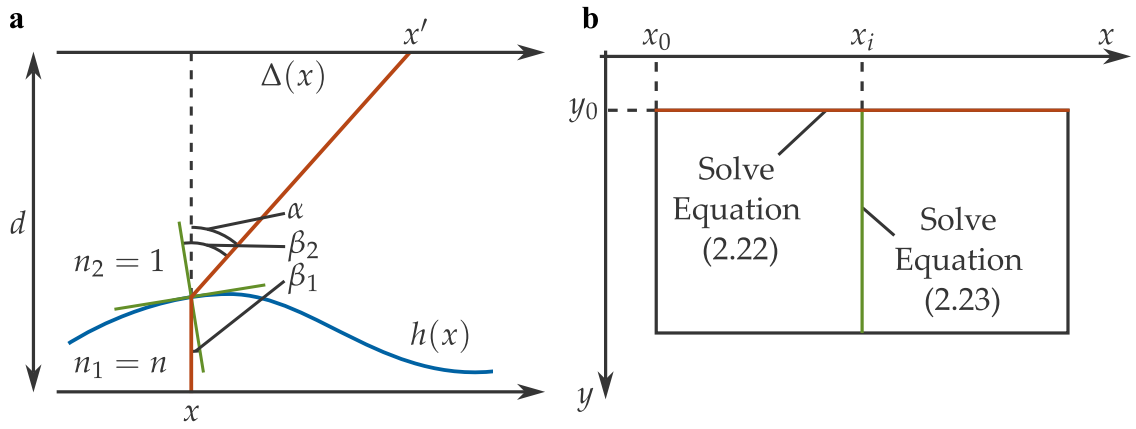

Figure 2.2: Geometrical parameters for refractive free-form surfaces and solution strategy of the coupled partial differential equations. In panel **a**, the light incides from below in parallel rays. A function $h(x)$ describes the height profile of an interface where the refractive index changes from the material ($n_1 = n$) to air ($n_2 = 1$). The angle of incidence between the incident ray and the surface normal is denoted as β_1 whereas the refraction angle at this surface is called β_2. After the refraction, the ray travels further until it reaches the top canvas at the distance d. Due to the refraction, it hits the canvas at the distance $\Delta(x)$ with respect to the point where the ray would have hit the canvas without refraction. The absolute angle of deflection is called α. In panel **b**, the solution strategy for the coupled partial differential equation is illustrated. The equation is split into two equations where the first equation is solved along a line in x-direction with the starting conditions at (x_0, y_0) an the height h_0. Afterwards, this solution function $h(x, y_0)$ is used to generate starting values for each position (x_i, y_0) to solve the second equation along the y-direction. Therefore, the height value can be derived for each point (x, y). The figure was adapted from [68].

2.2.1 *General formulation of the problem*

The setting for the refractive free-form surfaces discussed in this thesis is shown in Figure 2.2a. A parallel incident ray hits the refractive optical element described by the height function $h(x)$ from below at position x. At the interface, it gets deflected by the angle α with respect to its original propagation direction. The refractive index of the material is again called n, but considered to be wavelength independent. The refractive index of the air above the free-form surface is assumed to be 1. The ray then hits a canvas at the distance d to the substrate of the free-form surface at position x'. The difference between the two coordinates is described by the displacement function $\Delta(x) = x' - x$. This displacement function is the input that describes where each ray should hit the canvas. The height function $h(x)$ has to be derived in a way, that it fulfills this displacement for all x-coordinates.

2.2.2 *Derivation of a partial differential equation system describing the free-form surface*

The reason for the ray deflection is the refraction happening at the surface of the height profile. This is described by Snell's law considering the two angles of the incident ray β_1 and the final ray β_2, each with respect to the surface normal. Then, Snell's law leads to

$$n \cdot \sin(\beta_1) = \sin(\beta_2) \ . \tag{2.7}$$

The two introduced angles are put into relation with the total angle of deflection via $\alpha = \beta_2 - \beta_1$. Additionally, due to the direction of the incident ray, β_1 is associated with the slope of the height function

$$\tan(\beta_1) = h'(x) \ . \tag{2.8}$$

Last, the geometry gives a connection between the total angle of deflection and the displacement function

$$\Delta(x) = (d - h(x)) \cdot \tan(\alpha) \ . \tag{2.9}$$

The main goal is now to eliminate all angles and find a relation between the height function $h(x)$, the displacement function $\Delta(x)$, and the remaining, constant parameters n and d. Therefore, first the angle $\beta_2 = \alpha + \beta_1$ is replaced in Equation 2.7, such that

$$\begin{aligned} n \cdot \sin(\beta_1) = \sin(\beta_2) &= \sin(\alpha + \beta_1) && (2.10)\\ &= \sin(\alpha)\cos(\beta_1) + \cos(\alpha)\sin(\beta_1) \ , && (2.11) \end{aligned}$$

which is formed to an expression for the tangent of β_1

$$\begin{aligned} \sin(\alpha)\cos(\beta_1) &= (n - \cos(\alpha))\sin(\beta_1) && (2.12)\\ \Rightarrow \tan(\beta_1) &= \frac{\sin(\alpha)}{n - \cos(\alpha)} \ . && (2.13) \end{aligned}$$

Since this tangent can be identified with the slope of $h(x)$, see Equation 2.8, it is useful to now express the right side in Equation 2.13 with the displacement function and the remaining constant parameters. Therefore, the sine and cosine of the angle α are first expressed with its tangent using

$$\sin(\alpha) = \frac{\tan(\alpha)}{\sqrt{1 + \tan^2(\alpha)}} \ , \tag{2.14}$$

$$\cos(\alpha) = \frac{1}{\sqrt{1 + \tan^2(\alpha)}} \ . \tag{2.15}$$

Putting this into Equation 2.13 together with Equation 2.8, we find an expression for the slope of $h(x)$

$$h'(x) = \frac{\tan(\alpha)}{n\sqrt{1+\tan^2(\alpha)}-1}\,, \tag{2.16}$$

which is transformed into an Ordinary Differential Equation (ODE) by applying Equation 2.9

$$h'(x) = \frac{\Delta(x)}{n\sqrt{(d-h(x))^2+\Delta^2(x)}-(d-h(x))}\,. \tag{2.17}$$

As a side note, if we apply the small angle approximation, the term $\Delta^2(x)$ under the last square root is neglected, leading to a much simpler ODE

$$h'(x) = \frac{\Delta(x)}{(n-1)(d-h(x))}\,, \tag{2.18}$$

which is even solvable analytically by the separation of variables. However, the small angle approximation is too coarse for the later presented scopes of this thesis, which is why the more precise Equation 2.17 is used in the following.

Next, the one-dimensional ODE needs to be generalized for two dimensions in order to be able to derive 2D refractive surfaces deflecting rays onto two-dimensional canvases in a controlled way. Therefore, the displacement function transforms to a vector and becomes depended of two variables

$$\Delta(x) \to \boldsymbol{\Delta}(x,y)\,. \tag{2.19}$$

For the refraction itself, we exploit, that the incident ray, the final ray, and the surface normal all lie in the same plane. This means, that also the displacement vector $\boldsymbol{\Delta}(x,y)$ and the gradient of the surface height function $\boldsymbol{\nabla} h(x,y)$ lie in that exact plane. Therefore, Equation 2.17 holds true for the 2D case and can be written as

$$\boldsymbol{\nabla} h(x,y) = \frac{\boldsymbol{\Delta}(x,y)}{n\sqrt{(d-h(x,y))^2+|\boldsymbol{\Delta}(x,y)|^2}-(d-h(x,y))}\,. \tag{2.20}$$

This equation describes a set of two coupled Partial Differential Equations (PDEs), which has to be solved to obtain the refractive surface height profile $h(x,y)$ for a desired displacement function $\boldsymbol{\Delta}(x,y)$.

2.2.3 *Solution strategy of the partial differential equation system*

The solution of Equation 2.20 is not analytically possible and also numerically difficult. However, a possible solution strategy is presented in this section and used for all cases in this thesis. First, lets define an auxiliary function

$$H(x,y,h) := \frac{1}{n\sqrt{(d-h(x,y))^2 + |\boldsymbol{\Delta}(x,y)|^2} - (d-h(x,y))} , \tag{2.21}$$

which allows us to rewrite and split the PDE into two simplified equations

$$\partial_x h(x,y) = H(x,y,h) \cdot \Delta_x(x,y) , \tag{2.22}$$
$$\partial_y h(x,y) = H(x,y,h) \cdot \Delta_y(x,y) . \tag{2.23}$$

For rectangular definition domains, these two equations are now solved sequentially. In Figure 2.2b, a rectangular area is shown in which the coupled PDEs have to be solved. Lets assume that the height function has a boundary condition in the top left corner as $h(x_0, y_0) = h_0$. This value now serves as a starting value to solve Equation 2.22 for constant $y = y_0$. In that case, Equation 2.22 behaves like a normal ODE and is solved by commonly known numerical algorithms (MATLAB function ode45). As result, the height profile function on the top edge of the rectangle $h(x, y_0)$ is known. For a given x_i, the value $h(x_i, y_0)$ is used as a starting value for Equation 2.23 along y-direction. The result is the height function along the vertical line $h(x_i, y)$. Since x_i is hereby arbitrary the surface height profile can be derived at every point (x, y) and the complete height profile becomes available.

Last, the continuity of the solution $h(x,y)$ is discussed. Due to the solution strategy, the function is continuous along x-direction for $y = y_0$ and along y-direction ($\forall x$). If the displacement function $\boldsymbol{\Delta}(x,y)$ is continuous at position (x,y), then also the height function $h(x,y)$ is continuous at this position. However, for discontinuous displacement functions at $y \neq y_0$, the height topography is not necessarily continuous along x-direction.

2.3 Simulations for validating micro-optical elements designs

After a micro-optical element is designed, it is a good idea to perform a wave-propagation simulation on the height profile to checks its capabilities and also see effects of wave-optics which were neglected so far. Let the micro-optical element be in the xy-plane and the light propagate in positive z-direction. The scalar electric field of the incident light is described by $E_0(x, y)$. This could for example have the shape of a Gaussian beam profile. Next, the influence of the micro-optical element needs to be taken into account. Let $h(x, y)$ be the height profile of the element and n its refractive index. Then $\varphi(x, y) = (n - 1) \cdot h(x, y) \cdot k$ describes the phase difference between the light with an absolute wave vector $k = \frac{2\pi}{\lambda}$ when propagating through the element at position (x, y) in comparison to propagating the same distance in air ($n_{\text{air}} = 1$). Thus, this phase map is applied to the incident electric field to simulate the influence of the (thin) micro-optical element

$$E(x, y, z = 0) = E_0(x, y) \cdot \mathrm{e}^{\mathrm{i}\varphi(x,y)} \ . \tag{2.24}$$

To propagate this electric field to the canvas at distance d, it is first Fourier transformed in the lateral directions to $E(k_x, k_y, z = 0)$. In the Fourier space the propagator is expressed by $\exp(\mathrm{i}k_z d)$ for a propagation along the z-direction. The k_z-component of the wave vector now needs to be expressed by the k_x- and k_y-components, since they are the variables of the Fourier transformed electric field, so $k_z = \sqrt{k^2 - k_x^2 - k_y^2}$. Thus, the propagated electric field is given by

$$E(k_x, k_y, z = d) = E(k_x, k_y, z = 0) \cdot \mathrm{e}^{\mathrm{i} \cdot \sqrt{k^2 - k_x^2 - k_y^2} \cdot d} \ . \tag{2.25}$$

By a back Fourier transformation, the electric field on the canvas $E(x, y, z = d)$ is obtained. Typically, now the intensity $I(x, y, z = d)$ is calculated by taking the absolute square of the electric field.

Summary

Before a micro-optical element can be used or even fabricated, it needs to be designed. Therefore, in this chapter the theoretical description for the relevant micro-optical elements was given. At first the ideal lens form, which is more precisely only a focusing element, however, still described by the general lens equation, was derived. The resulting equations will be used for the design of the micro-lens array presented in Section 4.2.

As a second class of refractive optical elements a formalism was presented to derive a freeform surface which is capable of deflecting incident parallel rays into controlled directions individually. From Snell's law a set of partial differential equations was derived which needs to be solved numerically with a specific solution strategy to obtain the freeform surface profile. This approach will be used to calculate the surface profile of the segmented refractive optical element in Section 4.3.

For cross validation, in the last section of this chapter, a formalism was presented to check the capabilities of a micro-optical element's design using wave propagation simulations. By that the influence of such an element on light can be calculated an compared with the intentions one had when designing the element.

Chapter 3

3 Fabrication of micro-optical elements

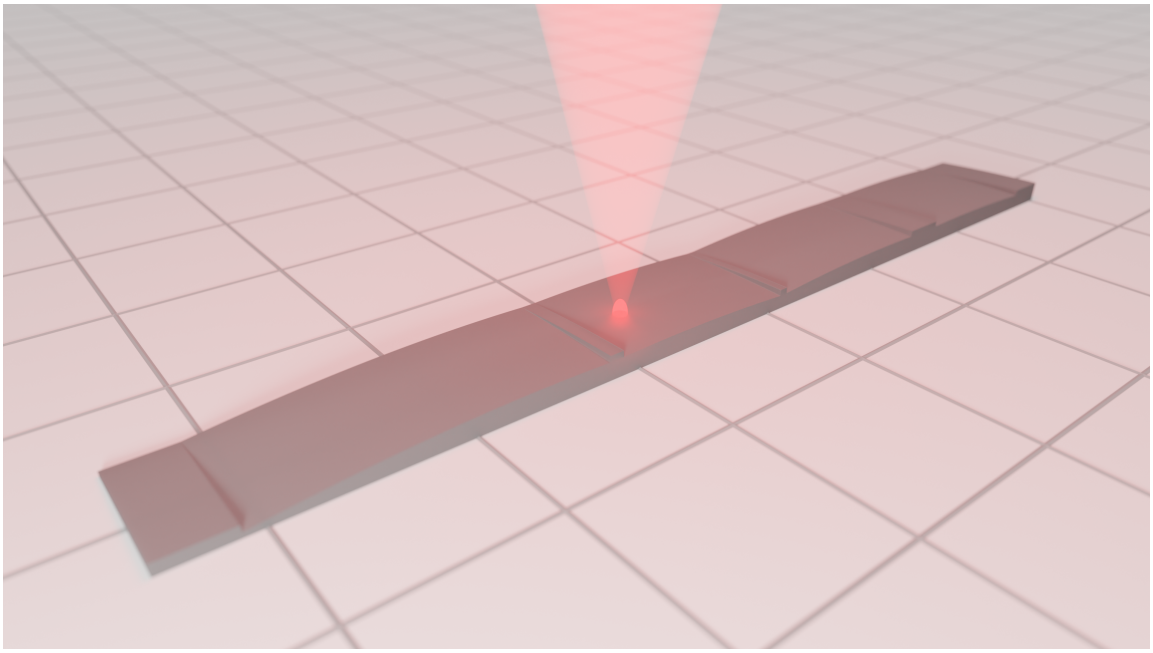

Artistic illustration of the 3D printing process of a refractive optical element. Adapted from [69].

The next logical step after designing an optical element is its fabrication. Depending on the kind of optical elements different techniques are promising. For micro-optical elements, as presented in this thesis, 3D laser micro-printing is very suitable. In this chapter, the working principle of a 3D laser micro-printer and the associated workflow is described. Additionally, the 2-photon grayscale lithography (2GL) technology is introduced. Since the surface accuracy of the micro-optical elements needs to be very high, further optimization is necessary even after the first print is done. Therefore, at the end of this chapter, a complete iterative precompensation routine is described which corrects for systematic errors during the printing process.

3.1 3D LASER MICRO-PRINTING

Since the first description in 1997 [35], 3D laser micro-printing developed to a very popular method of manufacturing micrometer-sized polymer structures [15, 70–77]. The fitting feature size and the availability of optical-grade surface quality make this technology very attractive for the manufacturing of micro-optical elements, such as micro-lenses [57–64], diffractive optical elements [14, 78–81], and optical gratings [82–84]. Thus, 3D laser micro-printing is used for the fabrication of the micro-optical elements presented in this thesis.

3.1.1 Two-photon printing

The core element of 3D laser micro-printing is a polymerization reaction triggered by laser light. The light is focused with a high NA objective lens into a liquid photoresist. The goal is that the reaction only happens in the focus in a small volume, called the voxel - the 3D analogon to a pixel. To ensure this goal, a non-linear behavior in the form of $D \propto I^n$ between the dose D and the light intensity I is necessary [85]. The number n hereby can be identified as the number of photons that need to be absorbed at the same time by one molecule to trigger the polymerization reaction. Thus, a one-photon absorption process means $n = 1$ leading to a linear relation and therefore an insufficient axial resolution. This is due to a high number of polymerization reactions happening in the defocused regions above and below the focal plane. Therefore, it can be said that at least a two-photon absorption ($n \geq 2$) is necessary. For the majority of photoresist systems, however, it is $n = 2$, which is why the technology is also very often called two-photon printing.

To now make a full 3D structure out of single voxels several steps are necessary. First, by scanning the voxel, e.g. by using galvanometric mirrors or mechanical stages, within the photoresist, lines can be printed. If two lines are printed close enough to each other, they will connect together to one object. This can happen even if the corresponding voxels do not touch each other due to the dose accumulation. This effect is called proximity effect. While this first sounds like a disadvantage and a loss in resolution, on the other hand it enables the connection of several parallel lines to a 3D printed plane. The distance between such lines is typically chosen constant and called the hatch distance. The same idea can now be applied for the connection of the parallel planes in the axial direction if they are printed close enough to each other. Due to the elongated shape of the voxel, the distance to merge two planes is larger then the distance to merge two lines in the lateral directions. To print a 3D body, one has to print several lateral planes, called slices, close enough to each other to connect them. This axial distance

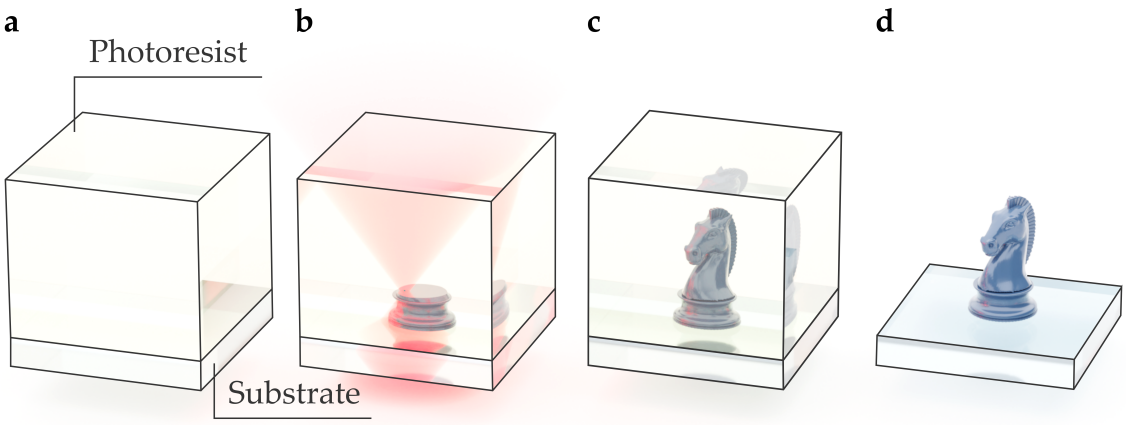

Figure 3.1: Graphical illustration of the general workflow of 3D laser micro-printing. First, a droplet of photoresist is applied onto a (glass) substrate (**a**) which is then put into the 3D printer. Next, the 3D structure is printed by focusing a femtosecond pulsed laser into the resist using a high NA objective lens (**b**). Due to the high intensity in the focus a two-photon absorption process happens, triggering a polymerization reaction, leading to a solid polymer. By scanning the focus through the volume larger structures of polymer can be created, typically in slices. After the scanning process is complete, the full 3D model is finished and lies within the remaining liquid resist (**c**). To get it out of the resist it needs to be developed by washing away the remaining resist with a solvent such as Isopropanol or PGMEA (**d**). The graphic was adapted from [86].

between two slices is called slice distance. In between the printing of two slices, a mechanical stages moves the substrate in the axial direction with respect to the objective lens among this slice distance. By varying the shape of the slices the 3D model can be replicated. This is of course only an approximation to the real shape of the model. The approximation becomes better, the smaller the slice distance is, however, this leads to an increase in the print time. If the slice distance is too high, deviations of the prints occur, for example stair-casing (see Section 3.1.2). The calculation of the shapes of the slices is called slicing and done before the printing by a dedicated slicer software. Within this thesis, GrayScribeX was used as a slicer for structures without overhangs, and NanoPrintX for arbitrary 3D structures including overhangs.

Sometimes it can happen that a desired object is laterally larger than the field of view of the objective lens used for printing. In that case it is not possible to print this object by scanning the voxel slice by slice using only galvanometric mirrors. Therefore, the object is subdivided into different sub-objects which are printed close to each other and thereby connect to the wanted structure. For better stability and surface-quality, it is useful, to let the sub-objects overlap a little bit.

In between the print of each sub-object the stage moves the substrate, so that the center of the next sub-object is beneath the objective lens. This approach is called stitching and the connection lines of the sub-objects are called stitching seams. In the ideal case these lines are invisible after the print, however, in many cases stitching artifacts appear at the stitching seams. This circumstance will be discussed later in Section 3.2 in detail.

The common workflow to perform a 3D laser micro-print is shown in Figure 3.1. In the fist step the photoresist is applied to a (glass) substrate and inserted into the printing device. The objective lens is dipped-in the viscose photoresist and lowered to the point that the focus point produced by the laser in right at the substrate. Now, the printing process is started and the structure is fabricated slice by slice. After the printing process is done, the substrate is removed from the printer but the finished structure is still within the resist. To get it out, the remaining resist needs to be washed away. This process is called development. For the cases presented in this thesis, the sample is first put into a bath of propylene glycol methyl ether acetate (PGMEA) for 20 min. Next, it is rinsed with fresh isopropanol followed by a second bath, this time in isopropanol, for 5 min. Last, it is rinsed a second time with fresh isopropanol and dry blown with nitrogen gas. Now, the structure has to be cleaned from the resist and is ready for usage afterwards.

3.1.2 *Two-photon grayscale lithography*

While the laser power was assumed to be constant during the printing process as described in the previous section, this changes when looking at two-photon grayscale lithography (2GL). In Figure 3.2a the influence of the laser power on the voxel size is illustrated. Assuming a Gaussian shaped squared ($n = 2$) intensity profile, which is proportional to the dose, in space, the voxel is given as the volume where the polymerization dose threshold is exceeded. When the laser power is now increased, the curve is scaled up, leading to a larger voxel size (blue area) in comparison to a lower laser power (green area). This fact can be used to adjust the voxel size during the printing process, see Figure 3.2b. Thus, artifacts from slicing, like stair-casing, are reduced and an optical-grade surface quality is achieved with an area-based mean roughness of 10 nm and an area-based squared roughness of 13 nm [87]. Since the laser power can be adjusted independently of the position of the galvanometric mirrors, the voxel size can be set individually for each spatial point, or, more precisely, the spatial dose distribution can be set freely within the limits of optical resolution.

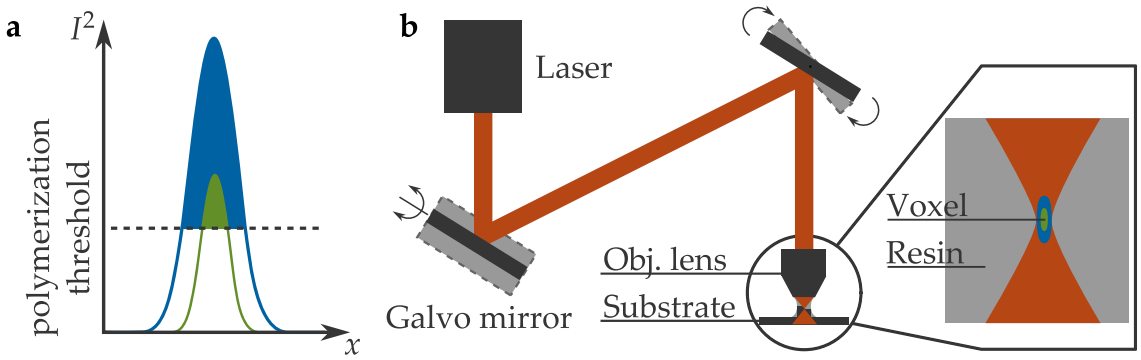

Figure 3.2: Illustration of the power dependency of the voxel size and the general assembly of the Nanoscribe QuantumX. The volume in which the polymerization threshold is exceeded is called voxel. As shown in panel **a** this volume depends on the optical power. When plotting the squared intensity of a Gaussian laser focus against its spatial coordinate and setting a polymerization threshold this circumstance can be understood by considering the volume with a higher squared intensity than the threshold. For a higher total laser power (blue) the voxel is larger then for a smaller total laser power (green). In panel **b**, the spatial scanning of the voxel in two dimensions using two galvanometric mirrors for x and y, is sketched. During the printing process the voxel volume can be adjusted via the laser power, simultaneously, to its x- and y-position using the two galvanometric mirrors. The figure was adapted from [36].

The approach to suppress the slicing artifacts is presented in Figure 3.3. While for the conventional two-photon printing (2PP) in panel a, the laser power and therefore the voxel size is constant, it is adjusted in the 2GL mode in panel b. When the shape of, for example, a lens is aimed to be printed, it first needs to be sliced. In 2PP, all voxels in each slice have the same size which inevitably leads to a stair-casing effect. For optical components requireing smooth surfaces, this is unacceptable. With 2GL, however, the voxel size is adjusted during the printing process enabling the possibility to "fade-in" a new slice and not starting with the full voxel size immediately. Therefore, the stair-casing can be avoided, which is very beneficial for the surface quality and shape accuracy. Both is very critical for the presented micro-optical components, which is the reason, why all presented samples within this thesis were fabricated exploiting the benefits of 2GL.

The only commercially available 3D printing supporting the 2GL technology is the QuantumX by Nanoscribe, which is used for the fabrication of the presented samples. A Zeiss $25\times$ /NA $= 0.8$ objective lens is used as a print head and the commercially available photoresist IP-S. This configuration is suggested by Nanoscribe as the medium-feature set (MF-set).

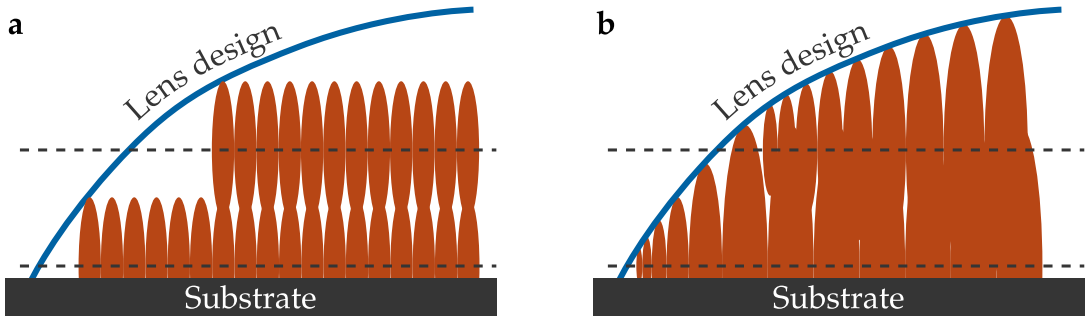

Figure 3.3: Illustration of conventional two-photon printing in contrast to two-photon grayscale lithography (2GL) at the example of printing a curved lens height profile. In conventional two-photon printing (**a**) the laser power is always constant and thus also the voxel size is always the same. Therefore, in each slice the voxel height is identical leading to an unwanted stair-casing effect at the surface. In 2GL, as shown in panel **b**, this effect can be circumvented by adjusting the size of the voxel during printing. By that, the top edges of the voxels can follow the aimed at design leading to a smoother surface without unwanted stair-casing. The figure was adapted from [36].

3.2 Iterative precompensation of 3D printed micro-optical components

Even though 2GL already delivers a good surface quality and shape accuracy in comparison to 2PP (see Section 3.1.2) the shape accuracy is still not sufficient for many applications [87]. To improve the quality even further, an iterative precompensation routine can be performed as described in the following. The presented precompensation routine was already published in [37].

3.2.1 Basic idea of precompensation

The basic idea is to measure the height profile of the printed sample with a spinning-disk confocal-optical microscope (Mahr MarSurf CM explorer, $50\times$ /NA $= 0.95$ objective lens) and thereby gain information about systematic deviations from the designed shape that can be compensated. This approach only works for 2.5D structures, meaning that no overhangs exist. The routine is illustrated in Figure 3.4. First, the design, which is illustrated as a block with one stitching seam included in its center, is printed without any modifications. The resulting print will then suffer from the above mentioned systematic deviations. In this case, especially the field curvature leads to a bending of the top surface and therefore artifacts especially around the stitching seam. The field curvature originates from

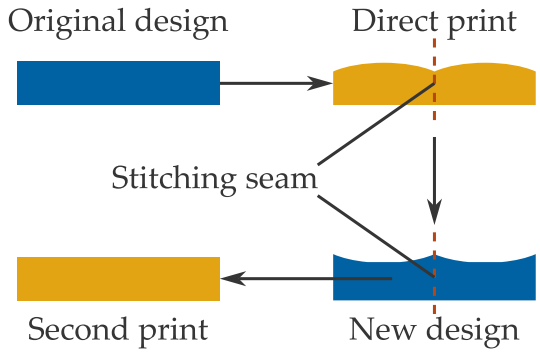

Figure 3.4: Illustration of the concept of an iterative precompensation. The design is naively printed resulting in a structure that deviates from the original design, especially pronouncing the stitching seam in its center. Next, a new design is calculated by adding/subtracting height to the regions where the print was too low/high. After a second print the errors and the height change cancel out each other, leading to a result closer to the original design.

spherical aberrations of the imaging system leading to a lower laser peak intensity at the edges of the writing field and therefore a lower height, see section before. The idea of the precompensation is now that the height profile of the printed structure is measured and compared with the original design. One will then spot regions where the printed structure is too high or low. In these regions the next, precompensated, design will get its height decreased or increased, respectively. Mathematically, this can be performed by calculating the difference between the measured topography and the original design and adding it to the original design again. After printing the new design, the systematic errors should cancel out with the precompensation and, therefore, the result should be closer to the aimed at structure.

On the other hand, it is important to stress the limits of this procedure. As already pointed out, only systematic errors can be compensated. As always, also during printing, statistic errors are relevant and cannot be compensated. Indeed, these statistic errors define the limit of shape accuracy that can be reached with this routine. An estimation of the statistic errors is shown in Section A.1 in the appendix.

3.2.2 *Overview of the necessary steps for a successful precompensation*

While the briefly presented principle of precompensation is quite simple, the details are more complicated then one might initially expect. The flowchart including the main steps for the precompensation routine is shown in Figure 3.5. While it all starts with the import of the design file and the measured topography file, the following main steps are an alignment between the two. This is necessary for making the two topographies comparable and later also subtractable.

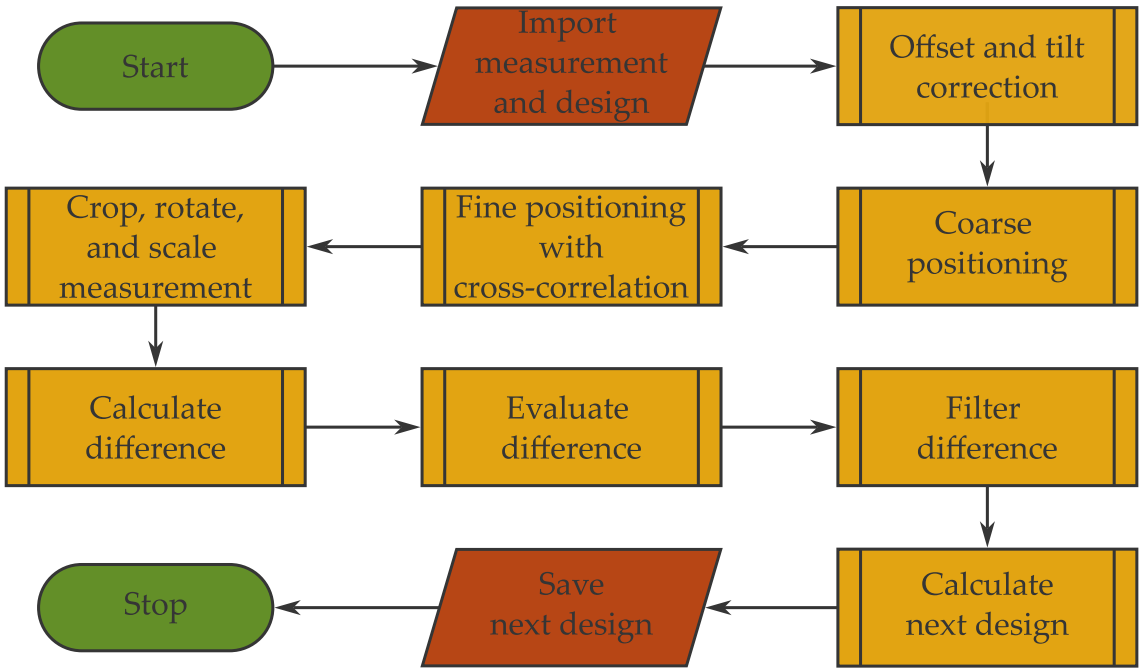

Figure 3.5: Flowchart of the Quandalf program. The measured topography and the design file are imported and spatially aligned in different steps. Next, the difference is first calculated, then evaluated creating some figures of merit, and, last, filtered to get rid of additional error sources like dust particles. Finally, the next design is calculated and save to be printed in the next round. The figure is adapted from [37].

Otherwise, the difference would compare points which do not correspond to the same position in the 3D structure. In this case the precompensation is useless and would probably decrease the print quality instead of improving it. On the other hand, this alignment is not trivial since the lateral image resolutions are not the same and, for obvious reasons, the topographies are similar, but not identical. All degrees of freedom, like a lateral shift, a rotation, and a lateral scaling, are corrected and aligned using image cross-correlation, which will be described deeper in the following section.

After the alignment is done the difference is finally calculated. However, to reduce the impact of statistical errors, it turned out to be useful to apply certain image filters to the difference map before calculating the new design. The new design is then saved in a data file that is ready to be used for the next print. The process can be repeated until the desired print quality is achieved, or the remaining errors are statistically dominated. Within the scope of this thesis, the described routine has been developed and automated in a computer program called **Quandalf** (QUANtum x Data Analysis tool using Light or Fluorescence microscopy), which is open source [88].

3.2.3 *Image cross-correlation for image alignment*

Let $f, g \in \mathrm{L}^2\left(\mathbb{R}^2\right)$ be two-dimensional images, as for example the measured topographies. For these functions the scalar product is defined as

$$\langle f|g\rangle = \int_{\mathbb{R}^2} f(\mathbf{x})g(\mathbf{x})\mathrm{d}\mathbf{x}\,. \tag{3.1}$$

This scalar product induces the norm

$$\|f\|_2 = \sqrt{\langle f|f\rangle}\,. \tag{3.2}$$

Next, the cross-correlation function between the two functions is given by

$$(f \star g)(\mathbf{x}) = \int_{\mathbb{R}^2} f(\boldsymbol{\xi})g(\boldsymbol{\xi}+\mathbf{x})\mathrm{d}\boldsymbol{\xi}\,. \tag{3.3}$$

Let us now assume that $g(\mathbf{x}) = f(\mathbf{x}-\mathbf{u})$, meaning that f is the same function as g but shifted about the vector $\mathbf{u}$. This is the scenario we are facing here, where the measured topography is, despite some small deviations, given by the design, but shifted in space. With a coordinate shift it can be shown that $\|g\|_2 = \|f\|_2$ and thus $g \in \mathrm{L}^2\left(\mathbb{R}^2\right)$ is still fulfilled. Considering now the cross-correlation function again, one can rewrite it as follows

$$F(\mathbf{x}) := (f \star g)(\mathbf{x}) = \int_{\mathbb{R}^2} f(\boldsymbol{\xi})g(\boldsymbol{\xi}+\mathbf{x})\mathrm{d}\boldsymbol{\xi} \tag{3.4}$$

$$= \int_{\mathbb{R}^2} f(\boldsymbol{\xi}) \underbrace{f(\boldsymbol{\xi}+\mathbf{x}-\mathbf{u})}_{:=h_{\mathbf{x}}(\boldsymbol{\xi})}\mathrm{d}\boldsymbol{\xi} = \langle f|h_{\mathbf{x}}\rangle\,. \tag{3.5}$$

Following the argument from before, the new defined set of functions $h_{\mathbf{x}}$ has the same norm as f. Also it becomes clear that $F(\mathbf{u}) = \|f\|_2^2$. Feeding these results in the Cauchy-Schwarz inequality

$$|\langle f|g\rangle|^2 \leq \|f\|_2^2 \cdot \|g\|_2^2 \tag{3.6}$$

we obtain

$$|F(\mathbf{x})|^2 = |\langle f|h_{\mathbf{x}}\rangle|^2 \tag{3.7}$$

$$\overset{(3.6)}{\leq} \|h_{\mathbf{x}}\|_2^2 \cdot \|f\|_2^2 \tag{3.8}$$

$$= \|f\|_2^4 = |F(\mathbf{u})|^2\,. \tag{3.9}$$

Since $F(\mathbf{u}) \geq 0$, it follows that $F(\mathbf{x}) \leq F(\mathbf{u})$ which means that the cross-correlation function between two shifted images has its maximum exactly at the displacement vector. Thus, by finding the maximum of the cross-correlation function, the displacement vector is determined which was the original goal. Once the displacement vector between the two images is known, they can be overlaid. In reality, however, there is not only a lateral displacement, but also a rotation and scaling between the two images. Thus, the more complex procedure presented in the following becomes necessary. However, the main idea of finding the maximum of the cross-correlation function remains the same.

3.2.4 *Alignment of the measured topography with the original design*

Now, the complete alignment process as implemented in Quandalf is described in detail in the order as shown in Figure 3.5. Let

$$D_x \in \mathbb{R}^{n_x},\ D_y \in \mathbb{R}^{n_y},\ D_z \in \mathbb{R}^{n_y \times n_x}\ , \tag{3.10}$$

be the design data, where D_x and D_y contain the x- and y-coordinates of each pixel and D_z the height values. The number n_x and n_y give the numbers of pixels in x- and y-direction, so to say, the image resolution. The pixel size for the design is called px_D. Since statistical errors should be minimized, it is useful to import several measured topographies at once and calculate their average later. Let N be the number of measurements taken and

$$\forall i \in 1, ..., N : M_x^{(i)} \in \mathbb{R}^{N_x},\ M_y^{(i)} \in \mathbb{R}^{N_y},\ M_z^{(i)} \in \mathbb{R}^{N_y \times N_x} \tag{3.11}$$

the measurement data. Again, $M_x^{(i)}$ and $M_y^{(i)}$ define the x- and y-coordinates of each measurement pixel and $M_z^{(i)}$ the corresponding height values. Also, N_x and N_y set the number of pixels for the measurement topography again. The spatial pixels size for the measurement is called px_M and might in general be different from the pixel size of the design.

Next, an offset and tilt from the measurement with respect to the substrate is corrected. Therefore, a region of interest, describing a rectangle with a thickness of 10 pixels and a distance to the edges of the topography image of another 9 pixels, is defined by the two index sets

$$I_x = \{10, \ldots, N_x - 10\} \setminus \{20, \ldots, N_x - 20\}\ , \tag{3.12}$$

$$I_y = \{10, \ldots, N_y - 10\} \setminus \{20, \ldots, N_y - 20\}\ . \tag{3.13}$$

To the topography points lying in this region of interest, a plane is fitted. Therefore, a goal function is defined as

$$\gamma : \mathbb{R}^3 \to \mathbb{R}, (a, b, c) \mapsto \sum_{j \in I_x, k \in I_y} |a \cdot M_{x,j}^{(i)} + b \cdot M_{y,k}^{(i)} + x - M_{z,kj}^{(i)}|^2\ , \tag{3.14}$$

and the optimal parameters are found through its minimum

$$\gamma(A, B, C) := \min_{a,b,c} \gamma(a, b, c) \ . \tag{3.15}$$

Now, the measurement data is corrected by the plane

$$E(x, y) = A \cdot x + B \cdot y + C \ , \tag{3.16}$$

by simple subtraction

$$M^{(i)}_{z,kj} \leftarrow M^{(i)}_{z,kj} - E\left(M^{(i)}_{x,j}, M^{(i)}_{y,k}\right) \ . \tag{3.17}$$

Next, the lateral alignment between the measurement and the design starts. The first step is a coarse positioning which is very fast, but only provides a precision of around 5-10 pixels. However, it is still useful to perform this step first, to be able to coarsely crop the measurement data afterwards without cropping the structure. This increases the performance and stability of the fine positioning later. For the coarse positioning, first, a histogram function $h(z)$ is defined which describes a histogram of the height values from the measurement $M^{(i)}_z$. With that, a height threshold T is defined as

$$h(T) = \min\{h(z) | z \in [0\,\mu\text{m}, 1\,\mu\text{m}]\} \ . \tag{3.18}$$

The idea of this threshold T is that it separates the areas with printed structure and the areas covering only the substrate. In the histogram, typically one sharp peak is visible at heights close to 0, ans another wider peak above zero, corresponding to all pixels associated with printed structure. By finding the minimum in the histogram, the threshold is found that separates both categories of pixels the best. Using this, an index set of all indices corresponding to the printed structure are obtained by

$$I = \{(j, k) \, | M^{(i)}_{z,kj} > T\} \ , \tag{3.19}$$

which enables to calculate the coordinates of the center of gravity (cog) via

$$x_{\text{cog}} = \frac{1}{|I|} \sum_{(j,k)\in I} j \ , \tag{3.20}$$

$$y_{\text{cog}} = \frac{1}{|I|} \sum_{(j,k)\in I} k \ . \tag{3.21}$$

By this step the coarse alignment is considered as being done, since the cog should lie in the center of the printed structure. Since the size of the structure is known,

it is now cropped out of the measurement file. However, as mentioned before, the coarse alignment is not very precise and the measurement might still be rotated. Therefore, a buffer zone of 100 pixels is left over. The region of interest (ROI) that will be cropped out is then calculated by

$$\mathrm{ROI}_{\mathrm{C}}^{(i)} = \{x_{\mathrm{cog}} - \frac{n_x}{2}\frac{\mathrm{px_M}}{\mathrm{px_D}} - 100, \ldots, x_{\mathrm{cog}} + \frac{n_x}{2}\frac{\mathrm{px_M}}{\mathrm{px_D}} + 100\} \times \tag{3.22}$$

$$\{y_{\mathrm{cog}} - \frac{n_y}{2}\frac{\mathrm{px_M}}{\mathrm{px_D}} - 100, \ldots, y_{\mathrm{cog}} + \frac{n_y}{2}\frac{\mathrm{px_M}}{\mathrm{px_D}} + 100\} \; . \tag{3.23}$$

The size of the region of interest is calculated from the size of the design as imported above and then calculated to the pixel size of the measurement. Now, the measurement data set is cropped to the coarse region of interest

$$\bar{M}_{z,kj}^{(i)} := \left(M_{z,kj}^{(i)}\right)_{(j,k)\in \mathrm{ROI}_{\mathrm{C}}^{(i)}} \; . \tag{3.24}$$

Next, the fine positioning using image cross-correlation can start. Therefore, the design file is zero-padded to have the same pixel number in both direction as the cropped measurement, so 100 pixels more in each direction. This zero-padded design is referred as $\bar{D}_z$. At first, the rotation angle between the measured topography and the design is calculated and corrected. Since the maximum value of the cross-correlation gives information about the similarity between the two images, it is used as a goal function to determine the correct rotation angle

$$f : \mathbb{R} \to \mathbb{R}, \alpha \mapsto -\max_{j,k}\left[\bar{D}_z \star \mathrm{imrotate}\left(\bar{M}_z^{(i)}, \alpha\right)\right]_{kj} \; . \tag{3.25}$$

Hereby, the function imrotate is a built-in MATLAB function that rotates an image by the input angle α, and $\star$ denotes the cross-correlation function as explained in the section before. The correct rotation angle $\varphi \in [-\pi, \pi]$ is found by minimizing the goal function

$$f(\varphi) = \min_{\alpha} f(\alpha) \; . \tag{3.26}$$

Next, a lateral scaling is corrected. Such a scaling mismatch can originate from different coordinate calibrations from the 3D printer and the spinning-disk confocal microscope, or lateral shrinkage. The principle is the same as for the rotation. First a goal function is defined exploiting the maximum of the cross-correlation

$$g : \mathbb{R} \times \mathbb{R} \to \mathbb{R}, (\xi, v) \mapsto -\max_{j,k}\left[\bar{D}_z \star \mathrm{scale}\left(\mathrm{imrotate}\left(\bar{M}_z^{(i)}, \varphi\right), \xi, v\right)\right]_{kj} \; . \tag{3.27}$$

Hereby, the function scale scales the already correctly rotated image about the factors ξ and v in x- and y-direction. Values above one mean a shrinkage and

below one an elongation. The correct scaling factors (s_x, s_y) are again found by minimizing the goal function

$$g(s_x, s_y) = \min_{\xi, v} g(\xi, v) \ . \tag{3.28}$$

In the last step, the two topographies need to be aligned laterally. This is done by exploiting the cross-correlation function once again. However, the measurement topography is first rotated and scaled using the previously found factors. Thus, the goal function is

$$h : \mathbb{N} \times \mathbb{N} \to \mathbb{R}, (l, m) \mapsto \left[\bar{D}_z \star \text{scale} \left(\text{imrotate} \left(\bar{M}_z^{(i)}, \varphi \right), s_x, s_y \right) \right]_{ml} \ , \tag{3.29}$$

which is maximized by the correct lateral displacement $(\Delta x, \Delta y)$, so

$$h(\Delta x, \Delta y) = \max_{l,m} h(l, m) \ . \tag{3.30}$$

Now, all the measurement topographies are rotated, scaled, and cropped according to the individually found parameters and to the size of the design. Additionally, they are rescaled, so that their pixel size now is the same as for the design file of 200 nm. This rescaling happens with the built-in MATLAB function imresize.

3.2.5 Calculating and evaluating the difference map

Now, since both, the measurement and the design, have the same pixel size and overlap each other the difference is calculated, for each measurement set individually

$$\text{Diff}^{(i)} = \bar{M}_z^{(i)} - D_z \ . \tag{3.31}$$

Before building the average over all these difference maps, some figures of merit are introduced to evaluate the quality of each measurement data set. This gives the user of the program the chance to kick out single measurement sets that severely suffer from errors, e.g. larger dust particles or remaining misalignment.

For the evaluation, first the height thresholds $T^{(i)}$ are calculated again

$$h(T^{(i)}) = \min_z h^{(i)}(z) \ , \tag{3.32}$$

where $h^{(i)}(z)$ is the histogram function of the measurement data set $i \in \{1, \ldots, N\}$. Next, a mask is defined considering all points with a higher value than the threshold

$$S_{jk}^{(i)} = \begin{cases} 1, & \bar{M}_{z,jk}^{(i)} > T^{(i)} \\ 0, & \bar{M}_{z,jk}^{(i)} \leq T^{(i)} \end{cases} \ . \tag{3.33}$$

This mask ensures that only pixels associated with the printed structure contribute to the calculation of the figures of merit. The first figure of merit is the mean absolute of the difference matrix

$$\mu^{(i)} = \frac{\sum_{jk} |\mathrm{Diff}_{jk}^{(i)} S_{jk}^{(i)}|}{\sum_{jk} S_{jk}^{(i)}} , \tag{3.34}$$

while the second is given by the standard deviation (root-mean-square) of the difference

$$\sigma^{(i)} = \left(\frac{\sum_{jk} \left[\left(\mathrm{Diff}_{jk}^{(i)} - \langle \mathrm{Diff}^{(i)} \rangle \right)^2 S_{jk}^{(i)} \right]}{\sum_{jk} S_{jk}^{(i)}} \right)^{\frac{1}{2}} . \tag{3.35}$$

Both figures of merit have in common that for a perfect print their value would be zero. In practice one can say that a smaller value indicates a better shape accuracy and, thus, also a better sample quality. Therefore, the all $\mu^{(i)}$ and $\sigma^{(i)}$ are shown to the user giving the user the chance to select measurement data sets that should be ignored for the calculation of the next design. This choice is saved in the following variable

$$C^{(i)} = \begin{cases} 1, & \text{user selects measurement set } i \\ 0, & \text{user rejects measurement set } i \end{cases} . \tag{3.36}$$

Now, the selected difference maps are averaged

$$\mathrm{Diff} = \frac{\sum_{i=1}^{N} \mathrm{Diff}^{(i)} C^{(i)}}{\sum_{i=1}^{N} C^{(i)}} , \tag{3.37}$$

and also the masks are merged

$$S_{jk} = \prod_{i \in \{1,\ldots,N\}} S_{jk}^{(i)} . \tag{3.38}$$

3.2.6 *Filtering the difference map and calculating the next design*

Before the averaged difference map is used to calculate the precompensated design, several filters are applied to suppress statistical deviations as much as possible. This is not only noise from the confocal-optical measurement itself but also localized defects or damages of the structure, like dust particles. All the latter deviations have in common that they are localized to a small area and lead to large

gradients in the difference map. Therefore, a filtering mask is defined exploiting a gradient and height threshold

$$m_{jk} = \begin{cases} 1, & |(\nabla \mathrm{Diff})_{jk}| > T_\nabla \text{ or } |\mathrm{Diff}_{jk}| > T \\ 0, & \text{else} \end{cases} . \tag{3.39}$$

Hereby, the two parameters are set to $T_\nabla = 300\,\mathrm{nm}$ and $T = 2\,\mu\mathrm{m}$ within the scope of this thesis. Generally, it might be useful to to adapt these parameters to the specific sample to obtain best filtering results.

The mask defined by m_{jk} finds all regions with large difference values or large gradients in the difference map. While these areas typically correlate with defects that have to be filtered out, the defects usually have a larger area than only the marked region. While a lowering of the thresholds would often include more areas that should not be filtered, it is more suitable to expand the marked regions in m. This widening is performed by the built-in MATLAB function imdilate. For the samples presented in this thesis the marked regions were expanded by 2 µm.

As already mentioned, the marked areas describe defects that should be filtered out from the difference map. The pixel values in these areas do not contain any useful information. Therefore, they are first excluded from the difference matrix

$$\mathrm{Diff}_{jk} = \begin{cases} \mathrm{Diff}_{jk}, & m_{jk} = 0 \\ \mathrm{NaN}, & m_{jk} = 1 \end{cases} , \tag{3.40}$$

where NaN stands for Not a Number. Now, the inserted NaN values need to be interpolated from the pixels around to fill the gaps again. This is performed by the MATLAB file exchange function inpaint_nans [89]. However, this method is problematic at the border regions. Additionally, at the borders typically very high differences arise, e.g., due to lateral shrinkage. Therefore, they are treated separately. In the filter routine, all pixels closer than 5 µm to the border are again set to NaN and then filled up using the MATLAB function fillmissing, which extrudes the pixel values from the inner pixels to the outside. This means that the amount of information at the pixels close to the border is very low. This is one reason for printing micro-optical elements larger than needed to have some buffer.

Last, noise originating from the confocal-optical microscope is filtered using a Gaussian filter via the MATLAB function imgaussfilt. The standard deviation is chosen to be 2 µm. Since the systematic errors, the precompensation tries to compensate for, typically occur at a larger spatial scale, the influence of this filter on them can be neglected. However, the reduced noise level increases the quality of the next design.

With that the filter routine is finished. A comparison between a filtered and unfiltered difference map is shown in Figure 3.6. The presented structure is a diffractive optical element that splits one laser beam into 7×7 beamlets [13]. In the unfiltered difference map some outliers are visible close to the corners. These outliers stem from an imperfect spatial alignment and do not contribute to the precompensation. Therefore, they are recognized by the filter algorithm due to their large gradient and filtered out to the smoother, filtered difference map which will lead to a better precompensated design.

The next design is now calculated as the difference between the previous design and the filtered difference. The previous design is either the original design for the first iteration, or the already precompensated design from the step before. The new design can now be saved and printed for either another step of precompensation, or it final purpose.

The practical performance and the amount of improvement gained by the precompensation routine will be presented in Section 4.2.2 at the example of a micro-lens array. It will be shown that the performance of the micro optical element is not sufficient for the demanded application without the precompensation routine. Additionally, in Section A.1 the borders of the improvement are shown by an evaluation of the statistical errors during the printing process and the measurement of the topography.

Summary

The micro-optical elements presented in this thesis are fabricated using two-photon 3D laser micro-printing. To achieve optical-grade surface quality and improve the shape accuracy, two-photon grayscale lithography (2GL), with the commercially available printer QuantumX, is used. For micro-optical components which do not contain overhangs, the shape accuracy can even be further improved by an iterative precompensation routine which is based on the comparison of the measured topography from the sample after a print and the design topography. The difference of both gives a hint were systematic artifacts occur and how they can be compensated for by changing the design for the next print. This happens by adding height to the structure where the structure appears too low and subtracting height at points, where the structure is printed too high.

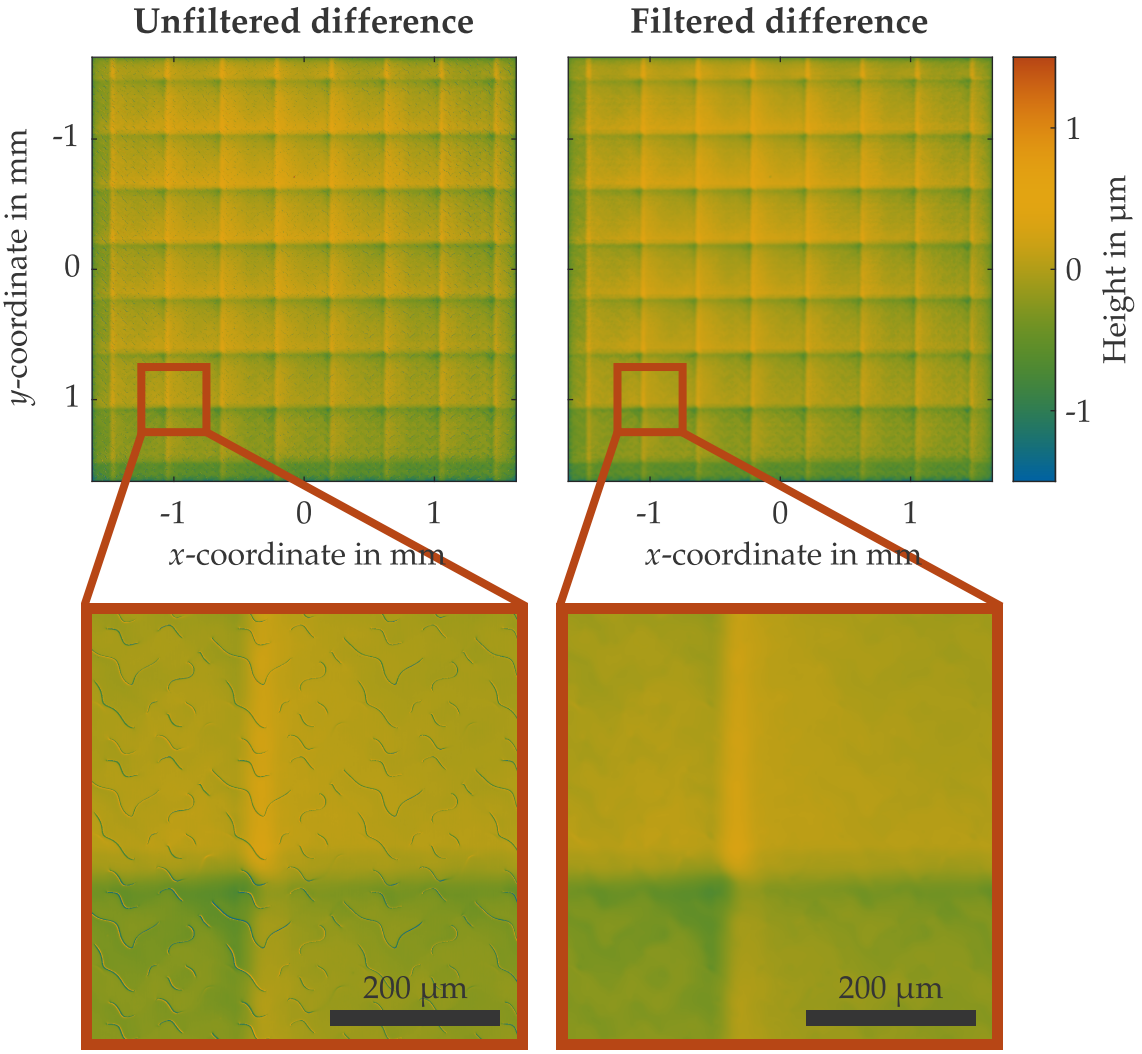

Figure 3.6: Comparison of the filtered and unfiltered difference map originating from a print of a diffractive optical element splitting a single laser beam into a 7×7 focus array [13]. In the unfiltered map several sharp artifacts from an insufficient alignment are visible, especially in the inset of the lower left corner. These outliers are detected, due to their high spatial gradient, and strongly suppressed using the presented algorithm, as visible in the filtered difference map. The figure was adapted from [37].

Chapter 4

4 Micro-optical elements in high-speed protein sequencing using Raman spectroscopy

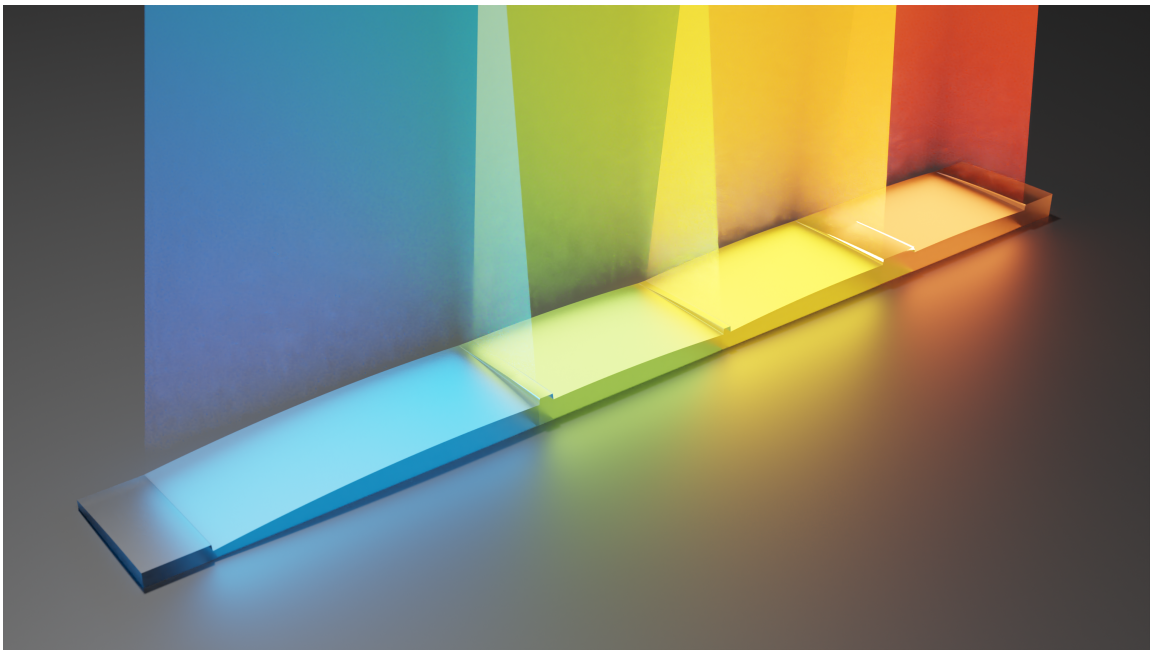

Artistic render of a refractive optical element shaping light from four different spectral regions.

Since it is difficult to hold a single amino acid from a protein inside a small excitation volume for a long time, the Raman spectrum needs to be recorded at a high speed and thus low intensity. Here, micro-optical elements are beneficial. First, a micro-lens array should increase the efficiency of the light detection by focusing the light onto the individual detectors. Second, only optimized spectral regions are focused on corresponding detectors, increasing the amount of information gained by a small number of detectors.

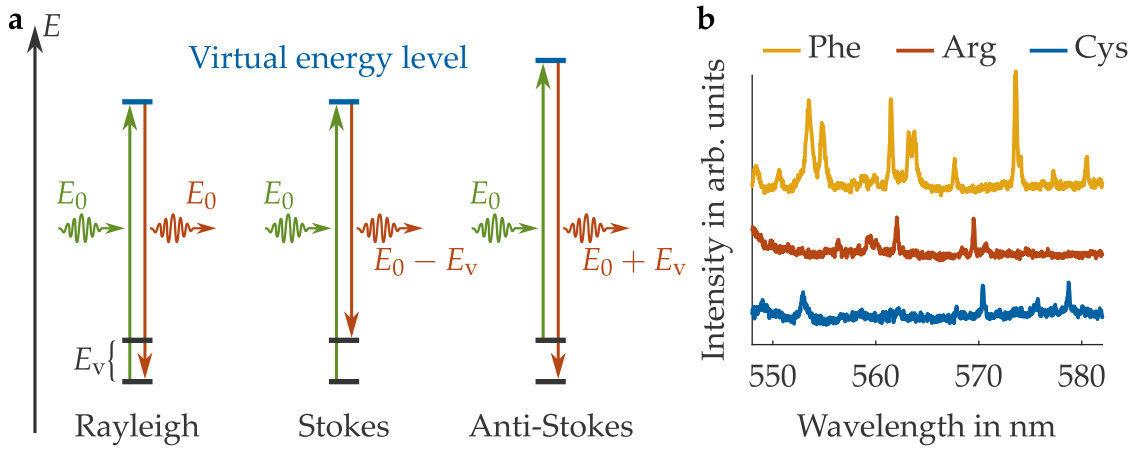

Figure 4.1: Illustration of the Raman scattering process and Raman spectra of three amino acids. In panel **a** two energy levels of a molecule are shown in a Jablonski diagram. When the molecule is hit by a photon, three processes can happen. In all scenarios, the molecule is excited to a virtual state which immediately relaxes back to a real state. Depending on the energy difference between the final real state and the initial state, the three processes are differentiated. Namely, they are Rayleigh scattering (elastic), Stokes scattering (emitted photon has less energy then the incident photon), and anti-Stokes scattering (molecule was excited before and the emitted photon has now more energy then the incident photon). Since the energy difference of the photons is exactly the energy difference of the vibration state E_V, is is characteristic for the molecule. Due to the existence of several vibration states, a Raman spectrum shows several characteristic peaks (**b**) and can thereby serve as a way of identifying the molecule. In this example, the excitation wavelength was 532 nm. Panel **a** was inspired from [90], the spectra of the tree amino acids Phenylalanine, Arginine, and Cysteine (**b**) are taken from the research group of Francesco De Angelis.

4.1 Fundamentals of Raman spectroscopy

Figure 4.1a shows the three main possibilities of a scattering process between a photon and a molecule. In all cases, the molecule is excited to a virtual state under absorption of the photon and immediately relaxes back into a real state under emission of another photon. Depending on the energy difference of the initial and final state of the molecule the scattering process is split into three categories: (1) If both states have the same energy level, the energy of the emitted and absorbed photon is the same. Thus, an elastic scattering process happens which is described by Rayleigh scattering. The intensity of this scattering process is the highest in comparison to the inelastic scattering processes. (2) For the first inelastic case the final state of the molecule has a higher energy as the initial state.

This typically happens under the excitation of a vibration state with the energy E_V. Due to energy conservation, the energy of the emitted photon is reduced by E_V and therefore the photon is red-shifted. This process is called Stokes scattering and is mainly used in Raman spectroscopy and also relevant within this thesis. (3) The Anti-Stokes scattering is a last possible outcome. Hereby, the molecule that interacts with the photon already needs to be in the excited state and loses its energy during the process. Therefore, the emitted photon is blue-shifted in comparison to the incident photon. The intensity of the Anti-Stokes scattering is temperature dependent on the Boltzmann factor since the excited vibration state needs to be populated initially. At room temperature, the intensity of the Anti-Stokes scattering is one to two orders of magnitude weaker than the signal coming from Stokes scattering.

It is important to differentiate between Stokes scattering and conventional fluorescence. For the fluorescence process, the molecule is excited into a real state and then relaxes after a finite life duration time. In contrast, Raman scattering happens immediately and the molecule is excited in a virtual state. Also, fluorescence only occurs if a real excited state exists for the excitation wavelength. In contrast, Raman scattering works with every excitation wavelength and always produces the same shifts.

As mentioned above, the shift in photon energy is dependent on the vibration energy of the molecule. Since there are several vibrational states in a molecule and their energies depend on the molecule structure, the complete Raman spectrum consists of several peaks which are characteristic for the molecule under investigation. In Figure 4.1b three Raman spectra of amino acids are shown. The excitation wavelength for the recorded spectra was 532 nm. For the distinction of different amino acids it seems suitable to compare the different peaks in the Raman spectra.

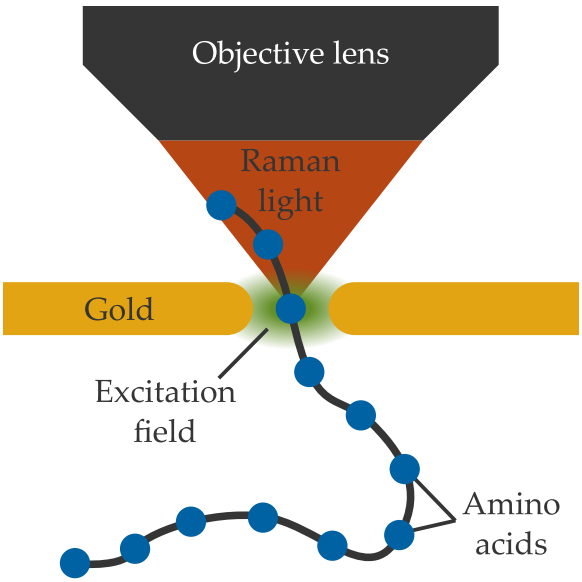

Figure 4.2: Sketch of the nanopore configuration for sequencing proteins. The protein is unfolded to a linear chain of amino acids and then pulled through a nanopore in a metal film (mostly gold). Due to the small diameter of the nanopore, the excitation field is restricted to a very small volume. Thus, only one amino acid is excited at the same time and emits Raman light, which is collected by an objective lens and the guided to the spectrometer for analysis.

4.1.1 Experimental setup for the excitation of single amino acids

For the main goal of sequencing the amino acid sequence in a protein it is necessary to excite only one amino acid at a time. This is possible with nano-optical approaches, for example pulling the protein through a nanopore [28, 29, 31, 33, 34], as sketched in Figure 4.2. The small size of the nanopore restricts the excitation field to such a small volume, that only a single amino acid is excited at the same time. The translocation time of one amino acids is thereby controlled via electro osmosis or surface interactions inside the nanopore by special coatings [31]. During the translocation time the amino acid emits Raman scattered photons which are collected by an objective lens. This light is then split into its spectral components either by a prism for an optical grating so that the spectrum afterwards is recorded by a detector array. Additionally to the ability to only excite one amino acid at the time, such nanopore approaches lead to field enhancements and, therefore, an increased Raman intensity. This is called Surface Enhanced Raman Spectroscopy (SERS) effect which is not only used for sequencing proteins [31–34], but also of DNA [27–30]. The field enhancements are in the order of 10^{10} to 10^{11}, which enables the detection of single molecules in the first place.

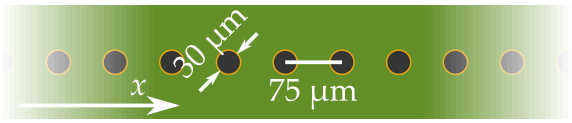

Figure 4.3: Sketch of the geometry of the SPAD array containing 128 detectors. The active areas have a diameter of 30 µm and a pixel pitch of 75 µm.

4.1.2 *Challenges in high-speed protein sequencing*

To sequence a protein via Raman spectroscopy, every single amino acid needs to be identified from its characteristic spectrum. For the nanopore approaches, the excitation time of a single amino acid is in the region of only $1 - 10\,\mu s$ resulting in less than hundred photons to detect. To still gain enough information from this number of photons, it becomes necessary to use sensitive, single-photon detectors, which are typically larger and more expensive than the typically CCD chips used for Raman spectroscopy.

To resolve these problems, custom-made micro-optical elements come into play. First, a micro-lens array is introduced, increasing the efficiency of a linear detector array. The lenses focus the light onto the active detector areas and thereby avoid the illumination of the insensitive areas in between. Thus, the efficiency can be increased by a factor of 5 in comparison to the absence of a micro-lens array. Second, a segmented refractive-optical element (SROE) is presented optimizing the amount of information gained by only a small number of detectors on the detector array. In the later presented example, the light is focused on only four detectors, where each detector should cover a specific, optimized spectral region. This has to be seen in contrast to the hundreds of detectors typically used for Raman spectroscopy within one CCD chip. The light is first split into its spectral components by a grating and then the SROE selects the optimized spectral regions out of the continuous spectrum. The light from each region is coupled into an optical fiber (see Figure 4.9 later), which is then connected to the corresponding detector. Thereby, the probability of correctly identifying the amino acid is be increased by 2.4 % for the presented example (see Section 4.3.1 later).

4.2 Micro-lens arrays for increased detection efficiency

A single-photon avalanche diode (SPAD) array consisting of 128 detectors covers a spectral range of 128 nm in a protein-sequencing Raman spectrometer. The light from emitted the sample is split into its spectral components by a prism and the resulting light rays are parallelized by a lens, so that the spectral components are evenly distributed over the SPAD array. The geometry of the SPAD array is given as a linear array of circular active areas corresponding to one diode each,

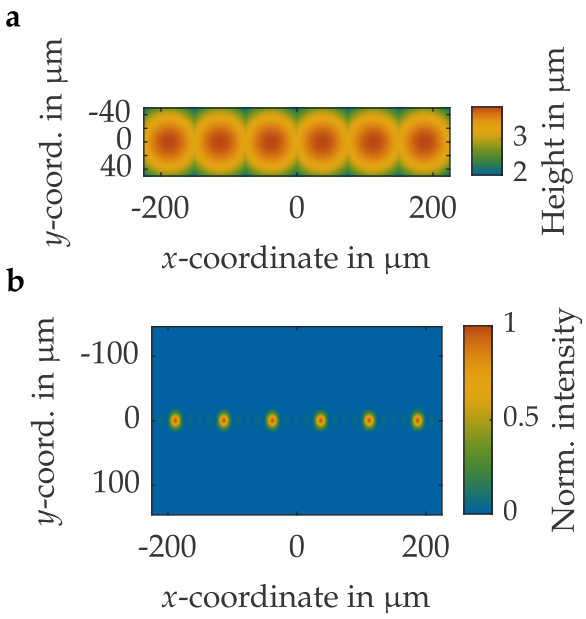

Figure 4.4: Design topography of six central out of 128 lenses of the micro-lens array and their corresponding optical simulation results. The six central lenses designed for the wavelengths 562 – 567 nm of the micro-lens array are shown as a height map in panel **a**. Panel **b** shows six focal points resulting from a wave-propagation simulation of the lenses shown in **a**. The size of them is close to the 30 µm demanded by the application and their distance along x-direction matches the pixel pitch of the detector. The figure was adapted from [37].

see sketch in Figure 4.3. The diameter of one circle (active area) is 30 µm and the distance between two center points of the detectors is given by 75 µm. Judging from these geometries, a micro-lens array (MLA) could increase the efficiency by a factor of 8 assuming an even illumination of the 75 µm × 75 µm square for one pixel and a perfect focusing. In reality, this factor might differ due to a not even, but Gaussian illumination and imperfect focusing due to a finite numerical aperture.

The working distance of the MLA is set to 2 mm measured from the glass substrate. A higher value would decrease the numerical aperture too far and therefore lead to an insufficient resolution. A smaller working distance, however, is not possible due to the electric wiring from the SPAD array which stand out over the detector plane. The following description of the MLA sample is already published in [37].

4.2.1 Adapting the ideal lens model to the given geometries

The MLA consists out of 128 lenses next to each other with a width of 75 µm in x-direction and a height of 100 µm in y-direction, matching the detectors geometry sketched in Figure 4.3. Therefore, the size of the lenses in this direction is given by the pixel pitch. For y-direction the lenses are a little bit larger than the Gaussian beam diameter of 48 µm to have some buffer in size. This is useful since, due to the described precompensation routine from Section 3.2, artifacts are not corrected at the outlines of the structure.

The lens form is calculated by the lens equation 2.3 presented in Section 2.1. The parameters are obtained from the geometrical boundaries described above. The refractive index of the material IP-S is published by Nanoscribe [91]. The values of the 2-photon-polymerized solid material are interpolated using a Sellmeier fit for wavelengths in between. Therefore, the refractive index is calculated for each lens with respect to the expected wavelength hitting the lens in the spectrometer. The MLA is designed for a wavelength range of $500 - 628\,\mathrm{nm}$, covering a difference of 1 nm per lens and a central wavelength of 564 nm. Putting all these information together, the height profile of the MLA is calculated and the center six lenses are shown in Figure 4.4a. For all lenses, a 2 µm height offset is added to optimize the print quality. Low values here might lead to deviations, e.g., by printing parts of the lenses into the glass substrate, whereas high values make stitching artifacts more severe and increase the print time.

In Figure 4.4b an optical simulation of the calculated height profile is shown as described in Section 2.3. This incident electric field was assumed to be constant in x-direction and Gaussian shaped in y-direction with a $1/e^2$ beam diameter of 48 µm. The result shows the desired focal spots at the desired positions. Due to the finite resolution of the imaging system, the spots have a finite size larger than the 30 µm detector active area, causing some light being lost at the edges of the active areas. Following the simulations, in sum 85.9 % of the light intensity would be collected by the photo detectors later in the experiment. The elliptical shape of the foci can be explained by looking at the numerical aperture in x- and y-direction. In x-direction, the lens is illuminated at its full width of 75 µm with a constant intensity, whereas the illumination along y-direction is restricted to a Gaussian intensity profile with a smaller height of the already mentioned 48 µm. Thus, the numerical aperture along y-direction is smaller than along x-direction, resulting in an elliptical shaped focus, elongated along y-direction.

4.2.2 *Experimental realization and characterization of the fabricated micro-lens array*

The MLA was printed using 2GL as described in Section 3.1 with a scan-speed of $200\,\mathrm{mm/s}$, a slice distance of 1 µm and a hatch distance of 200 nm. The remaining parameters were chosen as in the standard profiles from Nanoscribe. The stitching period was set to 375 µm, such that the stitching seams are always in between two lenses. A field overlap in between two stitching fields of 60 µm was used and 2GL stitching was activated to get best results at the stitching seams.

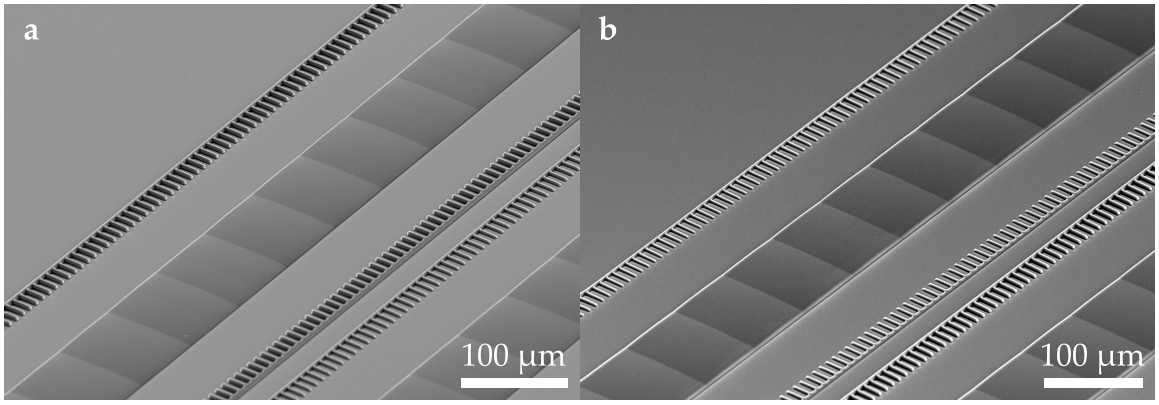

Figure 4.5: SEM images of a section of the micro-lens array. Both images contain stitching seams which are barely visible on the SEM images. One image is taken from the initial print (**a**) and the other from a print after two steps of precompensation (**b**). It is clear that an SEM image is not a suitable mean to characterize the surface quality of the micro-lens array without a deeper analysis of several images. The pictures are taken from [37].

In Figure 4.5, two scanning-electron microscopy (SEM) images of two MLAs are shown. One of the samples is directly printed without further modifications and the other one underwent the precompensation routine, as described in Section 3.2, for two iterations. While the individual lenses are recognizable and look smooth, no immediate differences can be observed, even though both images contain stitching seams. This illustrates that the SEM is no suitable technique for characterizing such micro-optical elements printed with 2GL, despite geting a quick overview over the 3D shape of the structure. Therefore, other characterization methods, such as spinning-disk confocal-optical microscopy and characterization in an optical test setup are shown in the following section.

Characterization of the topography

The first characterization method is the measurement of the surface topography using a spinning-disk confocal-optical microscope (Mahr MarSurf CM explorer, $50 \times /\mathrm{NA} = 0.95$ objective lens). This measured topography are then compared to the original design assuming, that if the difference becomes smaller, the quality of the MLA increases. Additionally, an iterative precompensation as described in Section 3.2 will be performed using these topography data.

In Figure 4.6 in the first row, the measured topographies of the first print, the first precompensation, and the second precompensation are shown. While there is a difference visible between the first print and the compensated versions, between the first and second precompensation, no difference is visible by bare eye.

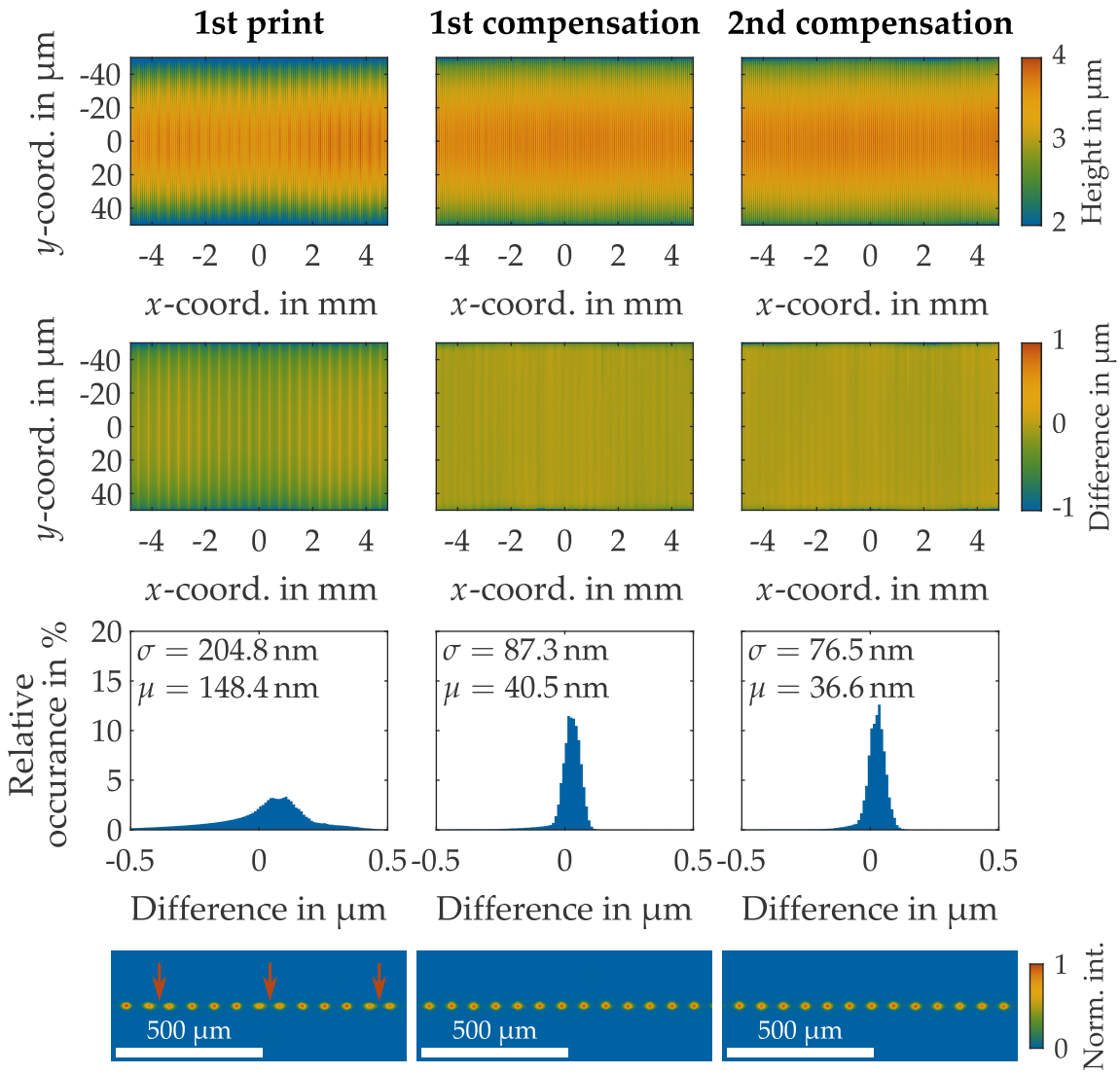

Figure 4.6: Presentation and evaluation of the measured topographies of the micro-lens array after different iterations of precompensation. In the first row, the measured topography is shown. For the sake of visualization, the x- and y-axis are scaled differently. In the second row the difference between the measured topography and the design is shown. The 1st and 2nd precompensation show significant improvements visualized by an overall more constant difference map. In the third row histograms of the difference pixel values are shown. In the ideal case, all pixels would have a value of zero. In reality, a narrower peak is a sign for a better quality. Additionally, the figures of merit as introduce in section 3.2 are presented. They also indicate that the quality improved with increasing number of precompensation. In the last row, an optical characterization is shown. While for the first print, every 5th (stitching period) focus point is deformed to its neighbor (red arrows), this effect visibly vanishes with increasing number of precompensation. The figure was adapted from [37].

Additionally, it is not obvious to tell weather the quality between the 1st print and the precompensations improved or not. Therefore, the difference between the measured topography and the design is shown in the second row in the same figure. Now, it becomes clear, that the initial print has way larger deviations in comparison to the precompensated versions. When having a closer look, one can see several vertical lines in the difference map of the initial print. These lines originate from stitching seams and disappear with the precompensation routine. Note that the x- and y axis are scaled differently and, therefore, the stitching field look elongated in y-direction.

In the third row of the figure, the histograms of the difference maps are shown. The peak visible in the histograms becomes narrower with increasing number of precompensations, indicating that the number of pixels with low differences increases. This is also visible at the two figures of merit σ and μ, see Section 3.2. Their value decreases, which also indicates that the quality of the MLA improves. Overall, the characterization via surface topography already gives a good impression that an improvement of the optical performance can be expected with increasing number of precompensations.

Optical characterization

The second and most relevant characterization of the MLA is an optical test in an experiment. Therefore, a test setup was assembled as sketched in Figure 4.7. In this setup, a laser with a wavelength of 561 nm, which is close to the center wavelength the MLA is designed for, is used as illumination. The beam quality is improved using a 75 µm pinhole and a iris diaphragm. After that the beam is collimated with a $f = 150\,\text{mm}$ focusing lens resulting in a $1/e^2$ beam diameter of 1.7 mm. Since all lenses of the MLA should be illuminated at the same time, a galvanometric mirror is used to rapidly scan the beam along x-direction. A second lens ($f = 100\,\text{mm}$) is parallelizing the deflected rays and focusing the beam to a line with a $1/e^2$ thickness of 42 µm along y-direction. In the focal plane of this second lens the MLA is placed. Here, the wavefronts of the light waves are flat and the shape of the scanned beam fits the requirements of the design. The resulting foci, generated by the micro-lenses, are imaged using a camera. Since the scanning frequency of the galvanometric mirror is much faster than the camera frame rate, all focus points are visible on the camera image. In other words, from the perspective of the camera, the illumination along x-direction is simultaneous.

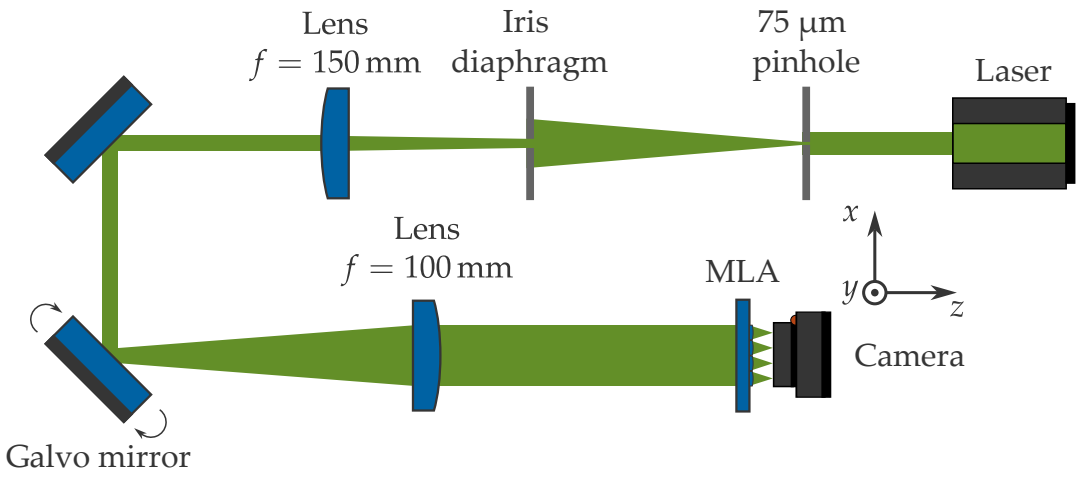

Figure 4.7: Beam path of the optical test setup to characterize the micro-lens array. A laser with 561 nm is guided on a pinhole for beam cleanup. The rings in the airy diffraction pattern are removed with an iris diaphragm and the beam is collimated using a lens. Next, a galvanometric mirror scans the beam along x-direction to illuminate all lenses of the micro-lens array along x-direction. Another lens relays the scanned beam again and focuses it onto the micro-lens arrays. The resulting foci are captured by a camera. Since the frame rate of the camera is much slower than the scanning speed of the galvo mirror, all focus spots appear at the same time on the images. This Figure was created using "ComponentLibrary" [92] by Alexander Franzen (CC BY NC 3.0).

The acquired images from this setup are shown in the last row in Figure 4.6. For the sake of clarity, only the central 13 spots of the total 128 foci are shown. While the spot size and distance along x-direction match the requirements of a 75 µm spacing, the shape of the spots deviates in case of the first print. It is visible, that every 5th spot is elongated towards its neighbor (red arrows). The distance of these elongated foci matches the stitching period of the printed sample. However, already with the first step of precompensation, this artifact disappears, indicating that the quality after one step of precompensation is sufficient.

4.3 SEGMENTED REFRACTIVE OPTICAL ELEMENTS FOR DISCRIMINATION OF AMINO ACIDS WITH LIMITED NUMBERS OF DETECTORS

As described in Section 4.1.2, sensitive single-photon detectors are typically very expensive, especially for small sizes. Therefore, one might rise the question if a SPAD array with 128 pixels as discussed in the previous section is really necessary. The spectra of the three amino acids shown in Figure 4.1b show that it might be enough to only measure spectral regions with characteristic spectral lines to identify the amino acid. In that case, a smaller number of detectors might be enough as well. In reality, one does not have to distinguish 3 possible amino acids, as shown in Figure 4.1b, but with 20 in total. Thus, the number of possible outcomes for the amino acid identification is limited to 20. While the number of detectors is not directly linked to the number of possible outcomes, it is clear that more detectors deliver more information about the details of the spectrum.

In this thesis, a protocol is demonstrated with an example of 4 detectors. Each detector will collect light from an optimized spectral region. The optimization, performed by Bikash Kumar Bhandari under the supervision of Nick Goldman, happens in a way that the amount of information gained by the system is maximized, which will be described in the following. The light deflection is performed by a segmented refractive optical element (SROE), which focuses the light from each spectral region onto an optical fiber tip. The optical fibers are then connected to the detectors. Light in between these optimized spectral regions is refracted out of the detection area. This protocol is presented in [68].

4.3.1 Derivation of the optimized spectral regions

Let D_i be the detectors which detect photons in the spectral intervals I_i ($i = 1,\ldots,4$). Let $f^X(\nu)$ be the intensity distribution of the Raman scattered light originating from amino acid X with respect to the Raman shift in wavenumbers ν. It turns out that the integral over the whole spectrum is the largest for the amino acid Serine. Therefore, all spectra are normalized with respect to Serine, meaning that the total intensity of all other amino acids are below 1. Let further T be the average number of photons emitted by Serine in the experiment. This value will be chosen to be 100 and 50 for two different optimizations and therefore two samples for demonstration. For the given interval I_i, the relative photon detection rate r_i^X is given by

$$r_i^X = \int_{I_i} f^X(\nu)\mathrm{d}\nu \,. \tag{4.1}$$

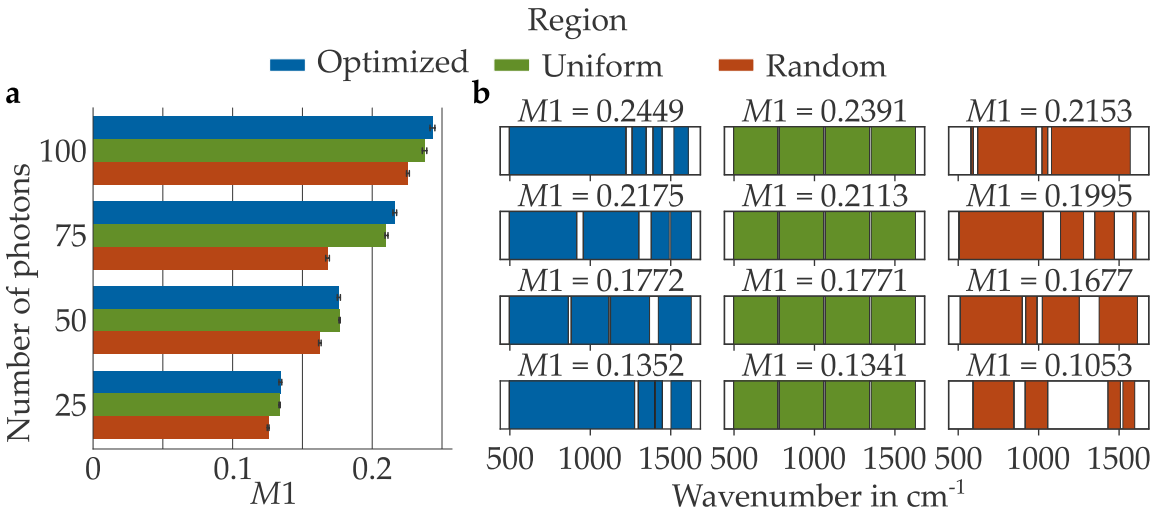

Figure 4.8: Different spectral regions and the corresponding $M1$ value. For each value of $T \in \{25, 50, 75, 100\}$, three scenarios are compared: Four spectral regions were (1) optimized, (2) uniformly with gaps of $\Delta\nu = 10\,1/\text{cm}$, and (3) randomly distributed over the whole spectrum and associated with one detector each. The value of the gaps matches the resolution limit of the later shown demonstrator test spectroscope, see Section 4.3.4. The corresponding average $M1$ values of 10 approaches each are shown in **a**. The errorbars denote the 100 % percentile. In panel **b** the specific spectral regions are shown for the case with the maximum $M1$ value. For the case of $T = 100$, the performance of the optimized regions is 2.4 % better than a uniform distribution. The figure was adapted from [68].

The goal is to optimize the spectral regions I_i $(i = 1, \ldots, 4)$, such that the probability for a correct identification of the amino acids is maximized. By Bayes law, the probability for the recognition of amino acid Y, when X is the true amino acid is proportional to

$$P(Y|X) \propto \text{prior}(Y) \cdot l_Y^X \,, \tag{4.2}$$

where $\text{prior}(Y)$ is the belief to find amino acid Y without further information, so typically $\text{prior}(Y) = \frac{1}{20}$, and l_Y^X is the likelihood to measure a spectrum corresponding to amino acid X, when Y is the emitting amino acid. Assuming a Poisson distribution for counts c with average μ

$$P_\mu(c) = \frac{\mu^c}{c!} \mathrm{e}^{-\mu} \,, \tag{4.3}$$

and using the expected values for the number of photons received by amino acid X in interval I_i

$$\mu_i^X = T \cdot r_i^X \,, \tag{4.4}$$

the likelihood is calculated as

$$l_Y^X = \prod_{i=1}^{4} P_{\mu_i^Y}(c_i^X) = \prod_{i=1}^{4} \frac{(\mu_i^Y)^{c_i^X}}{c_i^X!} \mathrm{e}^{-\mu_i^Y} \ . \tag{4.5}$$

Hereby, the photons counts from amino acid X at detector D_i, c_i^X, are simulated during the optimization process. In a last step, the probabilities $P(Y|X)$ are obtained via Equation 4.2 and the demand that they add up to 1 under summation over Y.

The mean of the diagonal elements of the matrix $P(X|Y)$ is called $M1$ and describes the expected probability of correctly inferring the true amino acid. Therefore, $M1$ serves as a good goal function during the optimization process and needs to be maximized while varying the intervals I_i. Note that due to the random generated values for c_i^X, the optimization might deliver different results each time. Therefore, the optimization is performed 10 times and the $M1$ values are averaged. The result are shown in Figure 4.8a. As a comparison, the optimized values are shown together with random spectral regions and uniformly spaced spectral regions. The cases $T = 50$ and $T = 100$ are later chosen for the fabrication of the SROE as demonstrator. It becomes clear that the optimization process increases the $M1$ value. This can be quantified in relative numbers for the case of $T = 100$ as $\frac{0.2449-0.2391}{0.2391} = 2.4\,\%$ with respect to the uniform distribution with $10\,1/\mathrm{cm}$ gaps in between the spectral regions. Only a small improvement like this leads to a better accuracy for the identification of the protein under investigation when comparing the measured amino acids sequence with a database [93]. The improvement of the identification accuracy is more drastically when one focused on only a subset of amino acids as shown in Section A.2 in the appendix. Even when only detecting two different amino acids in the protein this is very helpful for the identification of the protein. Additionally, the number of expected photons matter a lot. Indeed, the best results for only 50 photos on average ($T = 50$) is still worse than the worst spectral configuration for 100 photons. In Figure 4.8b, the spectral intervals for the scenarios leading to the highest value of $M1$ are shown. The optimized intervals for $T = 50$ and $T = 100$ shown in this figure are used for the SROE design presented within this thesis.

4.3.2 *Deriving the SROE topography as a refractive free-form surface*

To calculate the height profile of the SROE as a free-form surface, see Section 2.2, first, the boundary conditions need to be formulated and the necessary parameters need to be defined. The excitation wavelength in the experiment is chosen to be $\lambda_0 = 785\,\mathrm{nm}$. This wavelength is then red shifted by the Raman scattering process. The refractive index of the SROEs material is assumed to be constant over the whole Raman spectrum. The wavelength for which the refractive index is calculated for is 841.5 nm, which lies central in the spectrum. The refractive index is then calculated with the data from [91], as already described in Section 4.2.1 to $n = 1.5054$. Next, the working distance is set to $d = 15\,\mathrm{mm}$, which is a compromise between small angles of deflection and thus low structure height to print, and a sufficient numerical aperture of the SROE focusing elements.

Last and above all, the displacement function $\mathbf{\Delta}(x, y)$ needs to be calculated as introduced in Section 2.2 and illustrated in Figure 2.2. The SROE will be designed for a spectrometer, in which the light is split into its spectral components along x-direction, whereas the wavelength is constant along y-direction. The x-dependency of the Raman shift ν is calculated from the grating constant $g = 150\,\mathrm{grooves/mm}$ of the splitting grating, and the focal length $f = 300\,\mathrm{mm}$ of the curved mirror paralellizing the beam-lets and focusing them onto the SROEs back plane. First, the angle of diffraction for the first order is derived as $\sin(\varphi) = \lambda \cdot g$. Next, the position x at which the beamlet with wavelength λ hits the SROE is calculated from the focal length of the curved mirror $x = f \cdot \tan(\varphi)$. Putting both together, we get

$$x = \frac{f \cdot \lambda}{\sqrt{\frac{1}{g^2} - \lambda^2}} \,. \tag{4.6}$$

Replacing the wavelength $\lambda = \lambda_0 + \Delta\lambda$ with the excitation wavelength and the Raman shift $\Delta\lambda \approx \lambda_0^2 \nu$, which is expressed in a linearized form by the Raman shift in wavenumber ν, an approximation for the position x is found in dependency of the Raman shift

$$x = \frac{f \cdot (\lambda_0 + \Delta\lambda)}{\sqrt{\frac{1}{g^2} - (\lambda_0 + \Delta\lambda)^2}} \approx x_0 + \frac{f \cdot \Delta\lambda}{\sqrt{\frac{1}{g^2} - \lambda_0^2}} \approx x_0 + \frac{f \cdot \lambda_0^2}{\sqrt{\frac{1}{g^2} - \lambda_0^2}} \nu \,. \tag{4.7}$$

Hereby, the constant offset x_0 is of no interest and can be neglected by shifting the SROE to the left and right during the alignment process. Now, a linear relationship between the spatial position x on the SROEs back plane, and the Raman shift ν is given in a proportional way $x \propto \nu$.

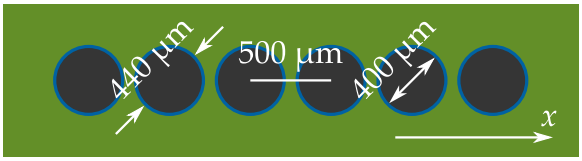

Figure 4.9: Sketch of the geometry of the fiber stack containing all relevant geometrical values. Only 6 fibers are drawn to gain a better overview. In the experiment only four out of 16 fibers were used.

Using Equation 4.7, the positions at which the light should be deflected by the SROE can be calculated. To detect light, it has to be coupled into an optical fiber which is connected to the detector. There are 16 optical fibers on a fiber stack (MPN:VGA-16-500-0-X-12-10-2.53-QM-IRVIS-400/440-3-0.75-1-0-PYREX) with a core diameter of 400 µm, a fiber diameter of 440 µm, and a center to center distance of 500 µm. From these 16 fibers, only four are used while the remaining are just ignored. The decision on which fibers are used is arbitrary and is done such that the maximum deflection angle of the light is minimized. Let the four selected fibers be at the canvas positions $\mathbf{x'}_i$ $(i = 1, \ldots, 4)$ according to the sketch in Figure 4.9. The light in between the spectral regions should not be detected. This is ensured by deflecting it along y-direction about $y_\mathrm{b} = 300\,\mu\mathrm{m}$. This value is a compromise between a better signal to noise ratio and a small structure to print. To summarize, the target position for each beam arriving at position $\mathbf{x} = (x, y)^\mathrm{T}$ is calculated as

$$\mathbf{x'}(\mathbf{x}) = \begin{cases} \mathbf{x'}_i, & x = x(\nu), \text{ with } \nu \in I_i \\ (x, y_\mathrm{b})^\mathrm{T}, & \text{else} \end{cases} . \tag{4.8}$$

Using Equation 4.8, the displacement function $\mathbf{\Delta}(x, y)$ is calculated by

$$\mathbf{\Delta}(x, y) = \mathbf{x'}(\mathbf{x}) - \mathbf{x} . \tag{4.9}$$

Putting all these constrains and parameters to the PDE for free-form surfaces from Equation 2.20, and solving it using the strategy presented in Section 2.2.3, the height profiles presented in Figure 4.10a ($T = 100$) and b ($T = 50$) are obtained.

Fabrication of the SROE

The SROE was fabricated using a hatch distance of 200 nm, a slice distance of 1 µm, a scan-speed of 200 mm/s, and the 2GL parameters as in the standard recipe for IP-S from Nanoscribe. Additionally, the stitching period was set to 420 µm, while the field overlap was left at 60 µm as for the MLA. Also, the 2GL stitching was used again to improve the quality of he structure close to the stitching seams.

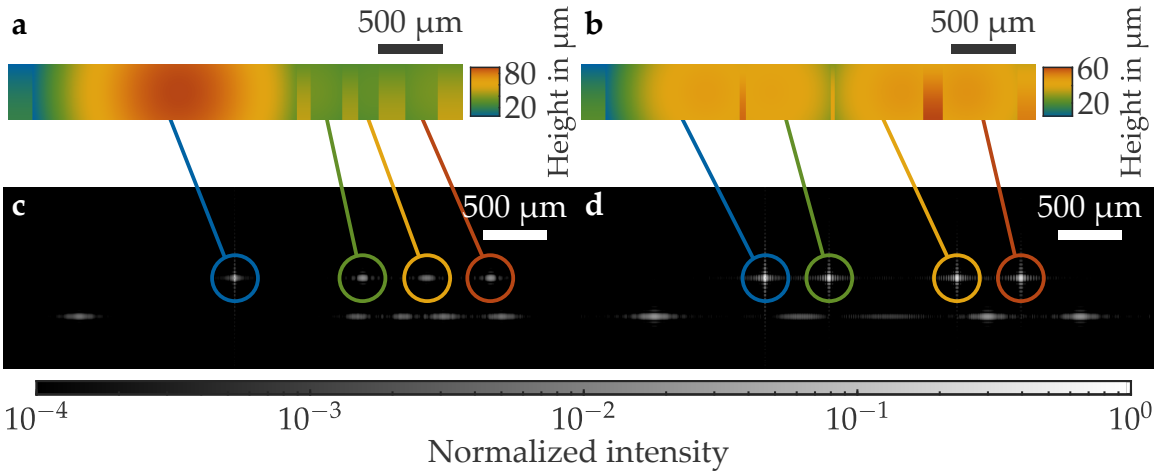

Figure 4.10: Graphical illustration of the solution of the SROE's height map and verification with optical simulations. The solution of the coupled PDEs is shown in panel **a** for $T = 100$ and in panel **b** for $T = 50$. As already shown for the micro-lens array, a wave-propagation simulation is performed to double check the capabilities of the solution. The results are shown in panel **c** and **d**. In both cases four focus spots are visible at the expected positions. By applying the illumination in the simulation only to parts of the SROE, it is proven that the spots indeed result from the light from the corresponding spectral region. This is illustrated by the colored circles and lines. The graphics were adapted from [68].

4.3.3 *Testing the SROE designs with simulations*

As already performed for the MLA, also the SROE design is first tested with simulations, before it is fabricated. The same wave-propagation method is used as shown in Section 2.3. Again, the incident light intensity is assumed to be constant along the x-direction and Gaussian shaped along y-direction with a $1/e^2$ beam radius of 300 µm. The results are shown in Figure 4.10c and d. It is clearly visible that there are four focal spots for each design which also appear at the correct positions. Note that since not all 16 fibers are used, there might be fibers skipped which leads to a not equidistant positioning of the focal spots. Additionally, there are horizontal lines below the focal spots which correspond to the light which is deflected along y-direction to avoid detection. By restricting the illumination to only the spectral regions that should be detected, it is shown that the focal spots indeed correspond to the light coming from the desired spectral regions. Therefore, the simulations show the capabilities of the SROE to fulfill its desired task.

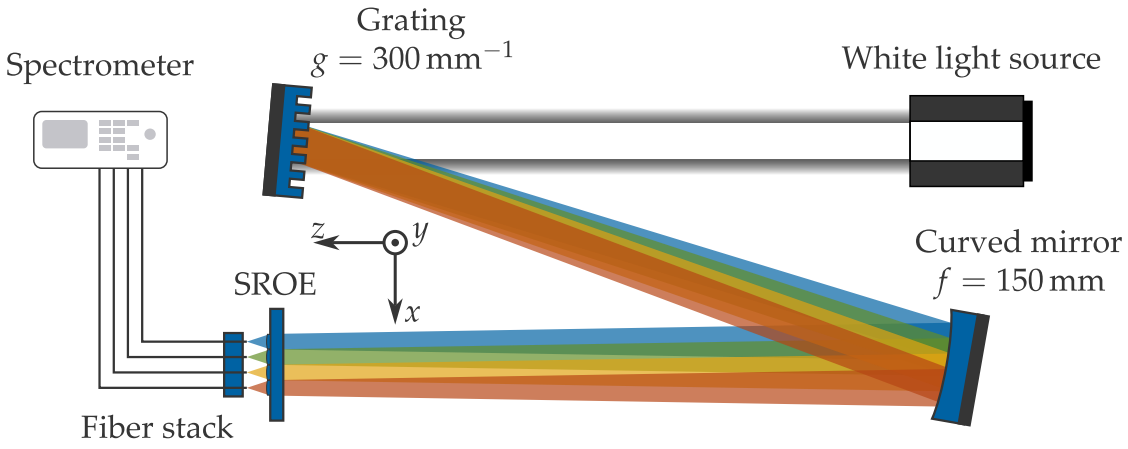

Figure 4.11: Beam path ot the optical test setup for testing the SROE. A white light laser source is split into its spectral components by a grating. The individual spectral beamlets are then parallelized by a concave mirror and focused onto the back plane of the SROE. The SROE then focuses the spectral regions it is designed for onto the end faces of four optical fibers in a fiber stack. Last, the fibers are connected to a spectrometer to prove that indeed the correct spectral regions are picked out of the continuous spectrum by the SROE. This Figure was created using "ComponentLibrary" [92] by Alexander Franzen (CC BY NC 3.0).

4.3.4 *Experimental characterization of the fabricated SROE*

As already performed for the MLA in Section 4.2.2, also the SROE should be experimentally characterized. Therefore, again, two different approaches for characterization were applied, the measurement of the topography using a spinning-disk confocal-optical microscope, and an optical characterization close to the real spectroscopy setup. In contrast to the MLA, the measurement of the topography and the resulting precompensation did not influence the optical performances notably. Therefore, it is not relevant for the optimization process and shown in the appendix in Section A.3.

The test setup for the optical characterization is sketched in Figure 4.11. This setup mimics the setup for the identification of an amino acid. Experiments with real amino acids are not included within this thesis. However, the used wavelength ranges are the same as in the final experiment for the sequencing of proteins. A white light laser (see spectrum in Figure 4.12) source is used for illumination and split into its spectral components by an optical grating (Thorlabs GR13-0310, $g = 300\,\mathrm{grooves/mm}$). The light from the first diffraction order is then parallelized and focused on the back plane of the SROE by a curved concave mirror (Thorlabs CM254-150-P01, $f = 150\,\mathrm{mm}$). This combination of grating constant and focal

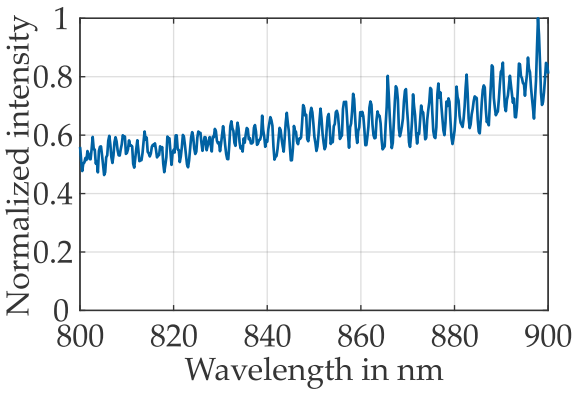

Figure 4.12: Light spectrum of the white light source used for the characterization of the SROE. The light is generated by focusing puled light from a fundamental mode in the near infra-red wavelength range onto an optically non-linear crystal. As a result, many optical transitions happen within the crystal leading to a quasi-continuous white light emission. The graphics were taken from [68].

length differs from the one, the SROE was designed for. However, as long as $\frac{1}{g^2} \gg \lambda_0^2$, both configurations are equivalent. The SROE then focuses the light from the designed spectral regions down to four spots, which are either imaged by a camera (IDS U3-3882LE-C), or the light is coupled into optical fibers in the fiber stack and then characterized by a spectrometer (Ocean Insight FLAME-T-XR1-ES).

The results of these characterizations is presented in Figure 4.13. In panel a and b the recorded camera images are shown which look very similar to the images obtained by the optical simulations in Figure 4.10. By aligning four fibers from the fiber stack to the produced four focus spots, the spectra of the light propagating though the fibers is measured using a spectrometer. There was no realignment of the fiber-stack or the SROE necessary between the measurement of the individual spectra. In Figure 4.13c and d, the measured spectra are shown, which match the desired intervals from the optimization process illustrated by the boxes in the background of the curves. Only for very small spectral regions, as for example the third region (yellow) for the 100 photons SROE (Figure 4.13c), the measured spectrum is too wide with respect to the design. This can be explained by the resolution limit of the imaging system. For a 500 µm diameter incoming beam, focused by the curved mirror, the spot size is around 300 µm. Within this length along x-direction, however, the wavelength already changes by 6.5 nm. This means that there is an overlap between beamlets of a spectral range of these 6.5 nm, hence $\Delta\nu = 10.5\,1/\mathrm{cm}$, at each point. Since the spectral width of the third spectral region in the 100 photons scenario is only 3.5 nm wide, it cannot be focused without also focusing light from neighboring spectral regions into it. For a future improvement, this effect should be included before the optimization of the spectral regions. However, it is also possible, to include the information about the filtering capabilities of the SROE in combination with the optics before into the algorithm, which will select the corresponding amino acid from the database and thereby improve the precision.

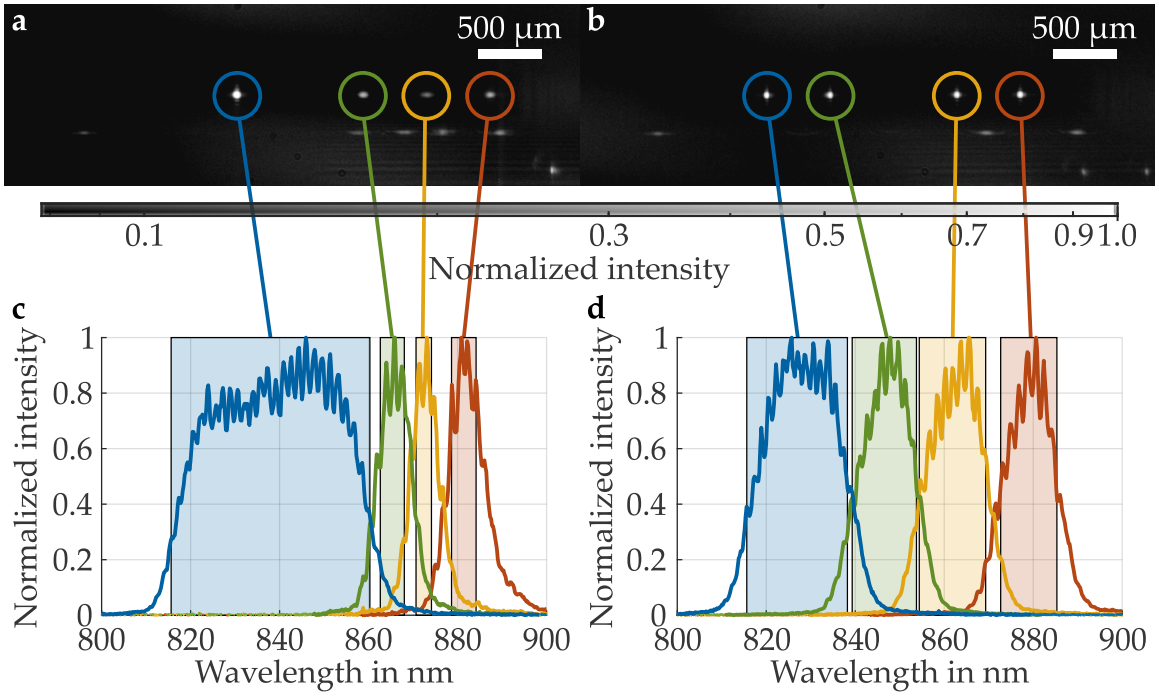

Figure 4.13: Test results of the characterized SROE versions. In panel **a** and **b**, camera images from the four focus spots are shown. Therefore, in the test setup from Figure 4.11, the fiber stack was replaced with a camera chip. The shown images match the requirements and show a lot of similarity with the simulations shown in Figure 4.10. Next, in panel **c** and **d** the measured spectra of the light from the individual optical fibers are shown. The rectangles in the background thereby illustrate the designed optical regions. The curves match the designed regions with the exception of very narrow regions as for example the yellow colored in panel **c** which appears to be wider. This comes from the limited spatial resolution of the imaging system. The high-frequency fluctuation, however, is not an artifact from the SROE but comes from the white light laser source. The figure was adapted from [68].

Summary

When performing high-speed molecule identification by Raman spectroscopy, the number of detected photons becomes crucial. Here, micro-optical elements are a way to improve the light efficiency by focusing the light better onto the detectors, as done with the MLA. The presented steps for design and fabrication in this chapter show how to fabricate custom MLAs, fitting to the boundary conditions of the remaining optical elements, using commercial 3D micro-printers. Additionally, the presented SROE delivers an improvement to a much cheaper few-channel Raman spectrometer. The steps for the determination of the optimized spectral regions as well as the design of the SROE surface profile itself are kept general, making them adaptable to many different cases in optical spectroscopy.

Chapter 5

5 Micro-optical elements as scintillators

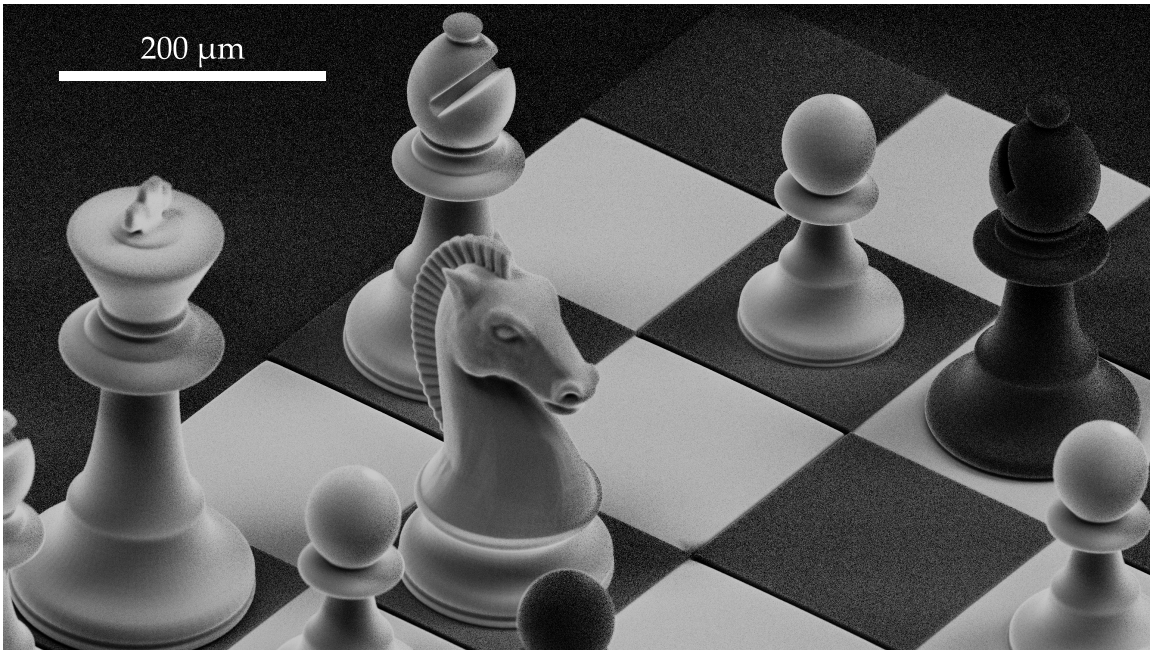

Overlay of two scanning electron microscopy images, detecting electrons and photons, of chess figures printed from scintillating (white) and not scinitllating (black) material (Adapted from [94]).

While the optical elements presented before only interacted with light, in the following chapter an example for the generation of light by the micro-optical element itself is demonstrated. In the discussed case, photons are generated under the radiation of electrons. This behavior is commonly known by scintillators, however, so far, plastic scintillators were not printable at the micro-scale. To achieve this goal, first, a custom photoresist is developed that has scintillating properties after printing. Next, suitable printing parameters, including parameters for two-photon grayscale lithography (2GL), are found to print the scintillator at a high quality including optical-grade surfaces. Last, the light efficiency of the scintillator is measured by comparing it to a commercially available product.

For over 50 years, plastic scintillators have been widely used in particle physics [38], and are still used in collider experiments as calorimeters [39–42], in the field of neutrino physics [43–45], or medical applications [46–49]. Many modern detector systems relying on plastic scintillators require a connection between the scintillator [95, 96] and the detectors, or a precise control over the scintillators shape [50, 51]. 3D printing of plastic scintillators [52–54] is a growing technique making both requirements feasible. On the other hand, state-of-the-art 3D printed scintillators do not match the requirements on spatial resolution given for some application concepts [55]. This is where 3D laser micro-printing comes into play. The content of this chapter is already presented in [94]. A resist is developed that is printable with commercially available micro-printers, delivering a higher resolution in contrast to the one-photon based printing approaches, and a good surface quality for optical applications. The motivation for the new material lies in the application of an active-Transverse-Energy Filter (aTEF) [55] that should be used in the Karlsruhe Tritium Neutrino (KATRIN) experiment to increase its sensitivity.

5.1 A RESIN FOR PRINTING SCINTILLATING MATERIALS

Simplified, in general a photoresist consists of one or more monomers and a photoinitiator. During the printing process, the photoinitiator absorbs ≥ 2 photons simultaneously and decomposes into radicals. These radicals then react with the surrounding monomers creating a cross-linked network of monomers, which is then called a polymer. Thus, also the scintillator resist needs to contain at least these two components to be printable at all.

For the scintillation effect, aromatic systems are necessary, due to their large number of delocalized electrons. The incoming high-energy electron first creates secondary electrons which then interact with those delocalized electrons and create UV-light. Thus, it is beneficial to chose a monomer, that already contains a significant number of aromatic systems [54].

Additionally, wavelength shifters are necessary in plastic scintillators. These molecules red-shift the generated light by a fluorescence process. By that, the reabsorption, and thus potential loss, of the just generated light by the scintillating material is suppressed and, therefore, the light efficiency is increased.

The exacts choices and justifications on the specific molecules are presented in the following.

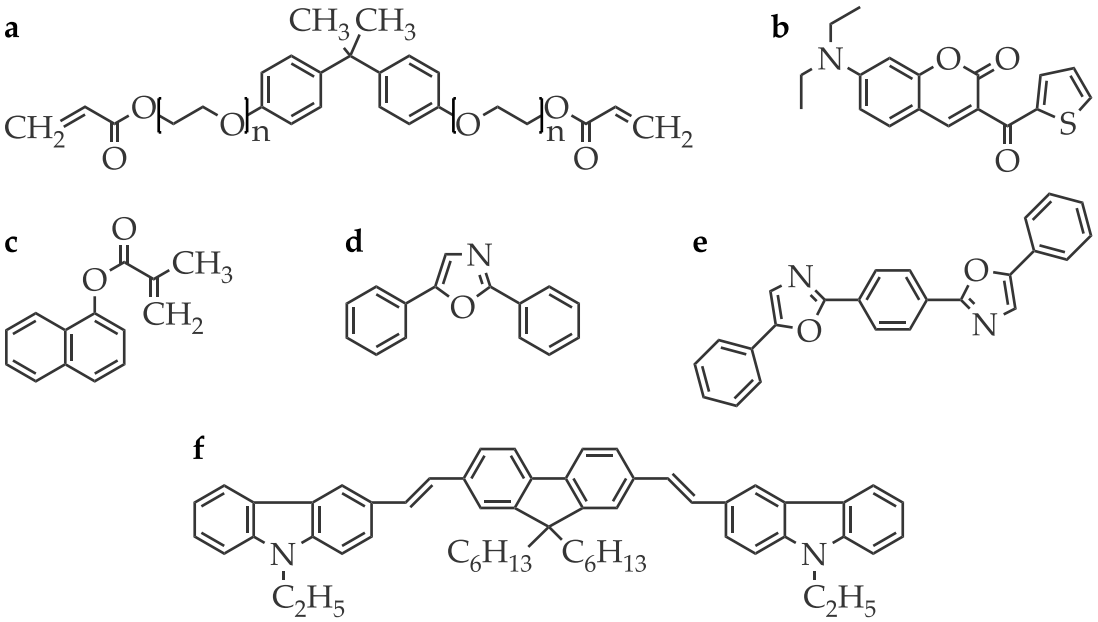

Figure 5.1: Structural formulars of the chemicals relevant for the presented scintillator resist. The molecules are Bisphenol A ethoxylate diacrylate (**a**), DETC or 7-diethylamino-3-thenoylcoumari (**b**), 1-Naphthyl methacrylate (**c**), PPO or 2,5-Diphenyloxazole (**d**), POPOP or 1,4-bis(5-phenyloxazol-2-yl) benzene (not used in the recipe) (**e**), and ADS086BE or 1,4-Bis(9-ethyl-3-carbazo-vinylene)-9,9-dihexyl-fluorene (**f**). Figure adapted from [94].

5.1.1 Chemical resin composition

A monomer that contains many aromatic systems is Bisphenol A ethoxylate diacrylate (Figure 5.1a) with an average molar mass of 468 g/mol. It is used as the main component of the scintillator resist. In comparison to the commercially available monomer mixture IP-S NPI from Nanoscribe (NPI stands for "no photoinitiator"), the light output from the first monomer turned out to be higher. As a photoinitiator, the molecule DETC (Figure 5.1b) was used with a concentration of 0.34 w.%. To increase the scintillation efficiency even further, 1-naphthyl methacrylate (Figure 5.1c) was added with 20 w.% as suggested in [53]. Hereby, an even higher concentration would increase the effect, on the other hand, the printability of the resist suffers a lot. A too high concentration leads to incomplete polymerization of the materials, even at very high laser power values. At the extreme, micro-explosions occur even before the material is polymerized completely. Thus, the chosen concentration can be seen as a trade-off. A deeper analysis of the effect of different concentrations of 1-naphthyl methacrylate is shown in the appendix in Section A.5.1.

For the wavelength shifter, there are several options. A widely spread molecule to perform a first shift of the freshly generated light is PPO (Figure 5.1d) [52–54], which is also used in the presented case with a concentration of 1.5 w.%. To increase the efficiency further, it is beneficial to perform a second shift to even more red shifted frequency ranges. This can be performed by adding POPOP (Figure 5.1e), or ADS086BE (Figure 5.1f). Since no difference in the performance was notable, but the solubility of the latter molecule in the monomers was better, ADS086BE was chosen as a second wavelength shifter with a concentration of 0.08 w.%.

5.1.2 *Mixing procedure*

For the mixing procedure, first, the two wavelength shifter PPO and ADS086BE both are solved in the 1-Naphthyl methacrylate at 60 °C under constant stirring for 1 h. Next, the DETC is added and the composition is filled up with the Bisphenol A ethoxylate diacrylate until everything adds up to 100 w.%. Afterwards, the resist is stirred again at 60 °C until the photoinitiator dissolved completely. Last, the resist is filtered with a 200 nm filter to remove dirt or remaining unsolved particles.

5.2 Determination of printing parameters

After the mixing of the resist is done, it is ready to be printed. However, for a successful print, the parameters as slice distance, hatch distance, laser power, scan speed, etc. (Chapter 3) need to be fine tuned to the resist. Therefore, several pre-experiments need to be done to systematically determine the correct combination of parameters. The general workflow for finding printing parameters, including those for 2GL, is shown in Figure 5.2. It starts by finding suitable parameters for conventional 2PP and continues with the parameters for the grayscale mode.

5.2.1 *Conventional Two-photon printing parameters*

In the first step, the scan-speed, hatch distance, and slice distance need to be set. These values can be chosen by experience values and are also recommended by Nanoscribe in the Nanoguide [97]. The scan-speed is set to the maximum value of 250 $^{mm}/_{s}$, which is adviceable, as long as no artifacts resulting from an imprecise scanning are visible or the resist show problematic behaviors connected to high scan-speeds. Additionally, the scan-speed might be reduced, if the maximum available laser power of the system is not sufficient anymore, to lead to a solid

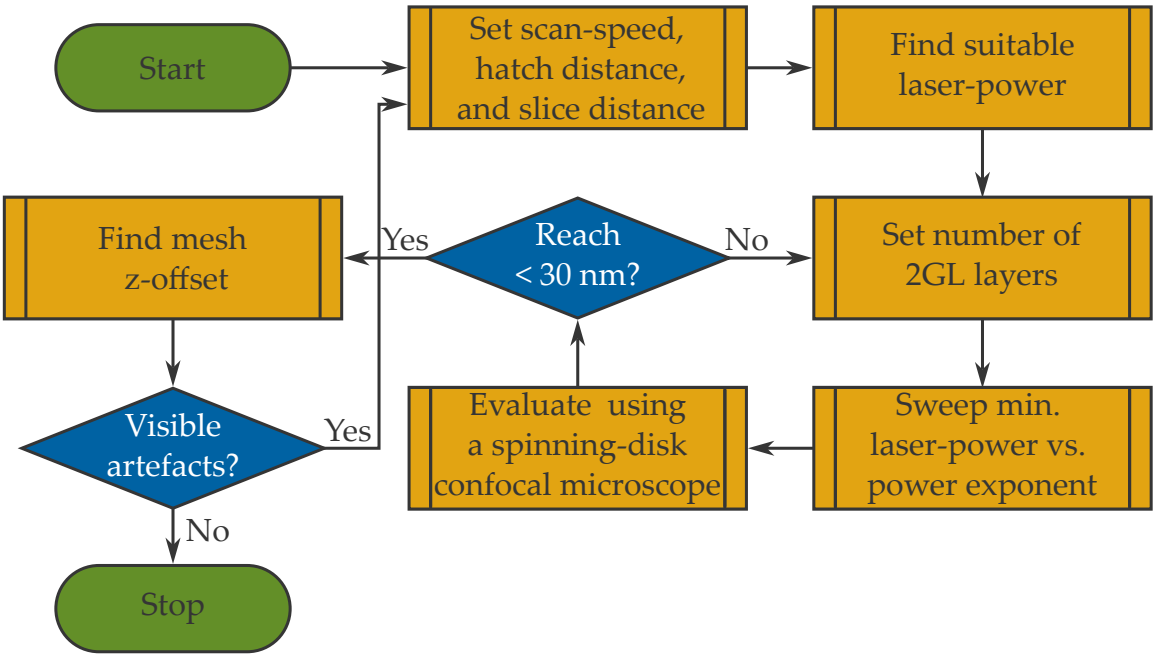

Figure 5.2: Flowchart for finding suitable 2GL parameters for custom resists. First, scan-speed, hatch distance, and slice distance are set followed by the estimation of a suitable laser power by in between the polymerization threshold and the micro-explosion threshold. Next, the number of 2GL layers is set (default 5) and the minimum laser power is swept versus the power exponent. Under confocal investigation the surface roughness for each parameter set is evaluated. If a threshold of 30 nm, as suggested by Nanoscribe, is surpassed for one parameter set, the mesh-z-offset can be estimated. Otherwise, the number of 2GL layer should be increased. After the whole process the structures are evaluated once again for further artifacts. If some are found, it might be necessary to go back and adjust the slice distance, hatch distance or even the scan-speed. If no severe artifacts are found, the parameter set is complete.

polymerization. For the presented scintillator resist this was not the case. The slice distance is chosen to 0.5 µm and the hatch distance to 0.1 µm. These values can be considered as quite conservative. If printing time is critical, both can be increased up to a factor of 2, to still be within the range of typical values for the medium feature set (25× objective lens). However, this might result in slightly worse printing quality. For too large hatch distances, the hatching lines might not be connected smoothly, as hatching is not affected by 2GL, and for too large slice distances, there might be some delamination or stair-casing, despite the use of 2GL. Overall, for the presented structures, such compromises were not necessary.

Having these basic parameters set, the laser power needs to be adjusted to achieve a sufficient cross-linking rate in the polymer, but not lead to explosions due to

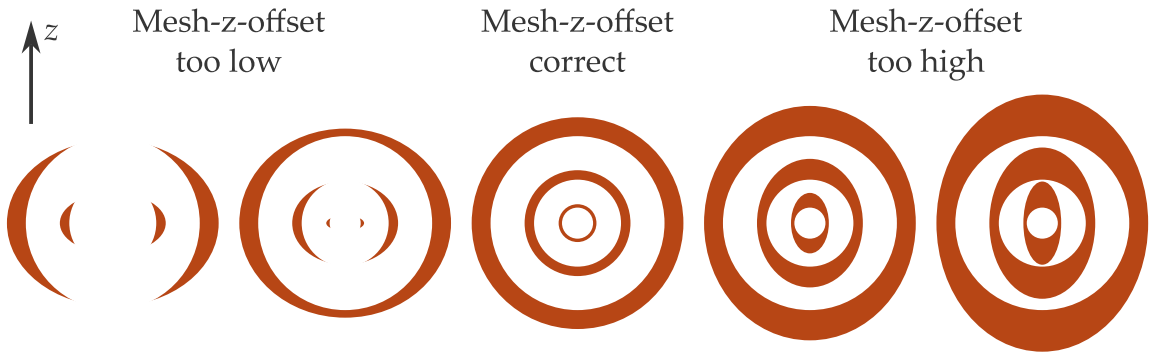

Figure 5.3: Sketch illustrating the printed structure for determine the mesh-z-offset. Several concentric rings facing to the lateral direction are printed. For the correct mesh-z-offset, these rings appear as round rings. If the mesh-z-offset is chosen too high, the top and bottom parts of the rings are too thick, whereas a too low mesh-z-offset leads to too thin ring elements at the top and bottom.

overheat. In general, lower hatch distance and slice distance values lead to a higher dose accumulation by proximity and, thus, a lower necessary laser power. A similar statements holds true for the scan-speed, where a higher scan speed also requires higher laser power. To find the correct laser power, small blocks are printed and investigated through the camera of the QuantumX printer itself. Once the edges and corners were sharply visible on the camera, the laser power can be considered as sufficient. Additionally, explosions become visible in the camera image and indicate a too high laser power. The optimal laser power for the presented system lies at 38 mW. With these parameters, conventional 2PP prints can be performed. However, if the advantages of 2GL should be used, more parameters need to be found as described in the following.

5.2.2 2GL-parameters

The 2GL profile is described by three parameters in the nanoPrintX software. The first parameter is the number of 2GL layers, which is set to 5. A higher value results is smoother surfaces, however, larger values here lead to more computational effort, and also a higher inward shift of surfaces along z-direction. This inward shift is an artifact of the 2GL algorithm and will be treated separately later.

After the number of layers is set, the next two parameters need to be determined, namely the minimum laser power and the power exponent. Therefore, a two dimensional sweep of small lens structures (with a radius of 130 µm, a height of 60 µm, and a curvature of 0.01 $^1/_{\mu m}$) are printed with varying one parameter along one axis. Thus, each of the printed lenses corresponds to another combination of

2GL parameters. After the printing and developing, as described in Section 3.1, is done, the lenses are evaluated under a spinning-disk confocal-optical microscope (Mahr MarSurf CM explorer, $50 \times /\mathrm{NA} = 0.95$ objective lens) to measure the surface quality and investigate possible slicing artifacts. Therefore, an evaluation script published by Nanoscribe in the Nanoguide [97] is used. A rule of thumb is to find a combination with a value for the parameter S_z, describing the maximum height of the structure after applying a bandpass filter from 2.5 µm to 8 µm, below 30 nm. This value can also be interpreted as a measure for roughness. For a minimum laser power of 8 mW and a power exponent of 1.5, an S_z value of 23.3 nm is found which can be considered as sufficient. If the best found surface quality is not sufficient for the demanded application, it might be necessary to go back and increase the number of 2GL layers. Then, the sweep with the lenses can be printed again with most likely smoother results.

Last, the inward shift of the models surfaces along z-direction needs to be treated. Therefore, the parameter mesh-z-offset needs to be determined, which simply counter-shifts all surfaces outwards along z-direction. A suitable 3D model to print, published by Nanoscribe, consists of rings facing in one lateral direction, see sketch in Figure 5.3. When looking from the side, the thickness of such rings varies if the mesh-z-offset is not chosen properly. For example, a too low mesh-z-offset results in thinner ring elements at the top and the bottom of the ring due to the inwards shift along z-direction, whereas a too high value results in thicker ring elements at the same position. Only if the thickness of the ring is constant all around, the mesh-z-offset is chosen properly. For the presented setup, the mesh-z-offset was found to be 1.9 µm.

Now, all printing parameters including those for 2GL are found. It is adviceable to perform a last check of the quality, in the best case by printing and characterizing the aimed at structure for the application. If there are severe artifacts remaining, for example visible hatching artifacts, it might be necessary to go back to the beginning and adjust the corresponding parameters (see Figure 5.2). If everything is sufficient for the application in mind, the process is complete and the printing of the original structures can start.

5.3 Measurement of the scintillators light yield

For large 3D printed samples, the scintillation capabilities typically are tested using an electron source and a photomultiplier, to which the scintillator is fixed to [52–54]. For the small samples presented in this thesis, this approach is not suitable since the covered area by the scintillator is too small and, therefore, the generated signal is not sufficiently strong. Thus, the printed scintillator samples are characterized in a scanning-electron microscope (SEM), where it could be hit by a focused electron beam in a controlled way. Additionally to the conventional secondary electron detector in the used SEM (Zeiss Supra 55VP), a photodetector (variable pressure secondary electrons, VPSE detector) is available to take luminescence images.

5.3.1 Qualitative demonstration of the scintillation effect

In Figure 5.4, a qualitative demonstration of the scintillation effect of the custom made resist is shown. In panel a and b, conventional SEM images of a chess board and figures are shown. For both images secondary electrons were detected and the acceleration voltage was set to 15 kV. The chess board and the figures were printed from two materials: IP-S for the black figures and fields and the custom made scintillator resist for the white figures and fields. On the conventional SEM images, no obvious difference between the two materials is visible. However, it can already be told that the print quality of both materials is comparable to each other in this scenario. In panel c and d, the same scenery is imaged, but this time photons are detected using the VPSE detector. The acceleration voltage was kept at 15 kV. Now a clear difference between the two materials becomes visible as the scintillator emits photons and therefore appears white. In contrast, IP-S remains black on the images. This clearly demonstrates that the scintillator resist fulfills its job and emits photons when hit by electrons. On the other hand, the black figures now appear as silhouettes, meaning that all their structural information, visible in the images before, cannot be obtained from the luminescence images. Therefore, in panel e and f, both images from before are combined into one image, conserving all the information from each measurement. Thereby, the luminescence image was used as a mask and overlaid with the conventional SEM image. For the mask, white pixels were set to transparent and with reducing white value, the transparency was also reduced. This procedure is also commonly known as luma keying. Therefore, the white figures appear bright as in the conventional SEM images, whereas the IP-S figures remain their structural information, but become darker. The horizontal stripes, especially visible in Figure 5.4e are artifacts from the scanning direction of the electron beam.

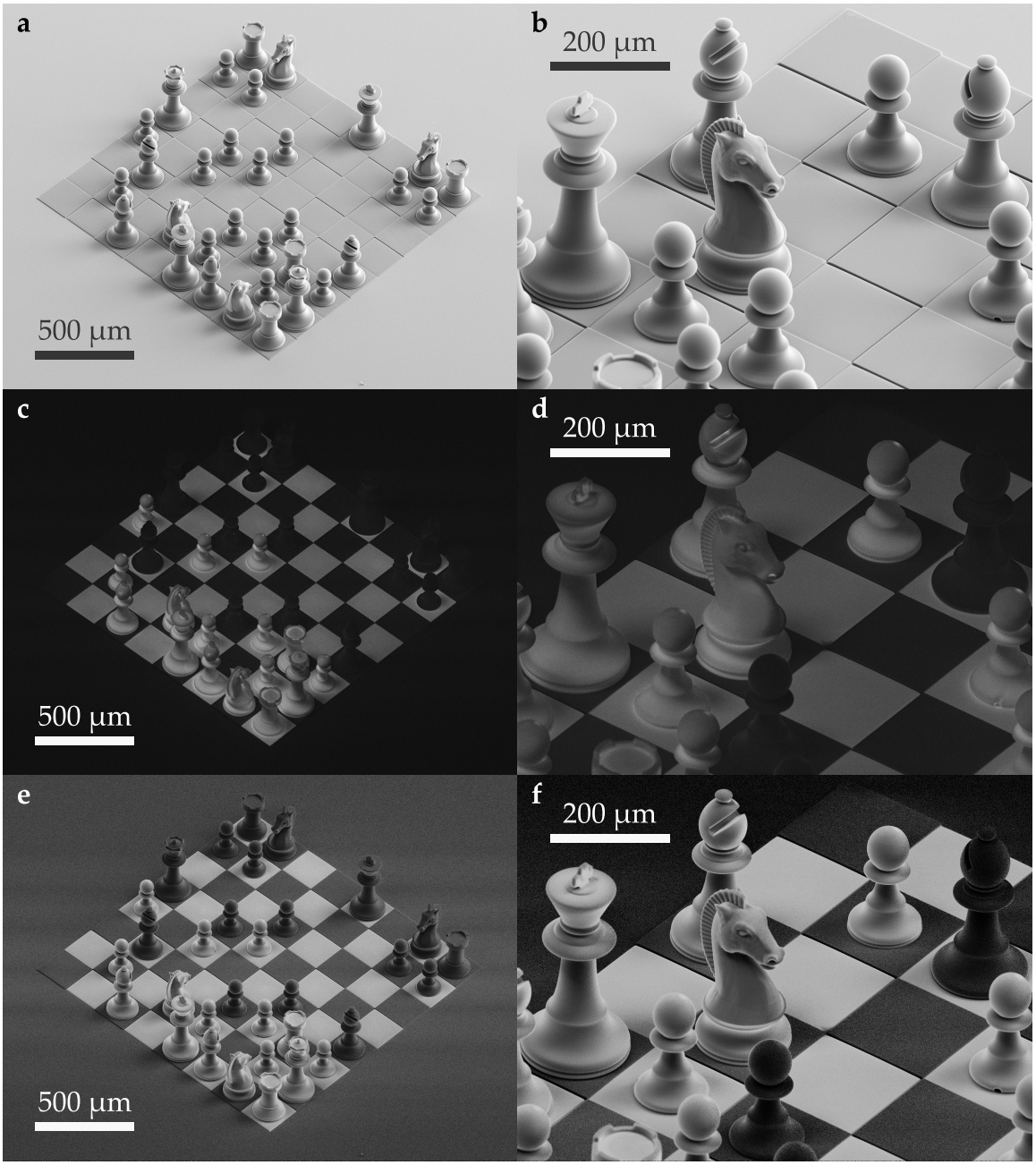

Figure 5.4: Demonstration of the scintillation capabilities. The sample is a 3D printed chess board where the figures and fields are either printed from the scintillator resist (white) and IP-S (black). In panel **a** and **b** conventional SEM images are shown with no visible difference between the two materials. In panel **c** and **d**, however, photons were detected instead of secondary electrons leading to signal from the scintillator, in contrast to the IP-S. In panel **e** and **f** an overlay of both images is shown where the image with detected photons serves as a white-to-alpha mask. In these last images, both, the structural information (especially of the IP-S) and the material contrast become visible. The figure is adapted from [94].

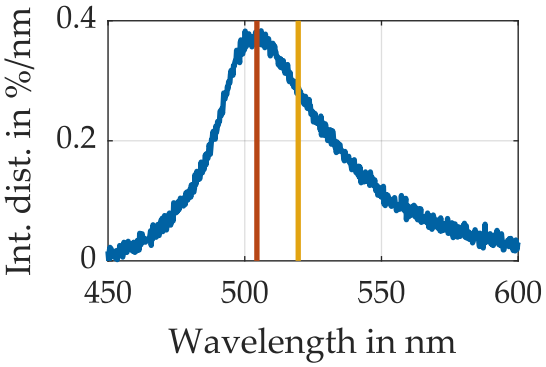

Figure 5.5: Fluorescence spectrum of the custom scintillator excited with a 360 nm UV lamp leading to a peak in the green regime. The position of the peak (red line) is at 504.4 nm whereas the mean wavelength from this intensity distribution is 519.5 nm (yellow line). The figure was adapted from [94].

5.3.2 *Quantitative analysis of the scintillation effect*

In a next step, the light output of the printed scintillator is characterized quantitatively. Therefore, a 500 µm × 500 µm × 500 µm large block was printed on a substrate and a second block of the same size was cut out of a commercially available plastic scintillator (Epic-Crystal, EPS100) with a known efficiency of 50 – 60 % anthracene or 9750 photons/MeV (using 17400 photons/MeV for anthracene [98]). After sputtering a thin layer of gold on the two samples, they were imaged with the SEM using 8 kV acceleration voltage and the VPSE detector. The resulting images are shwon in Figure 5.6. The 8-bit gray values of the images are averaged over the marked areas. The results are 93.1 for the EPS100 and 5.8 for the printed scintillator. These values need to be corrected for the wavelength dependency of the photodetector and its nonlinearity. The characterization of the detector itself is shown in the appendix in Section A.4. The emission wavelength of the

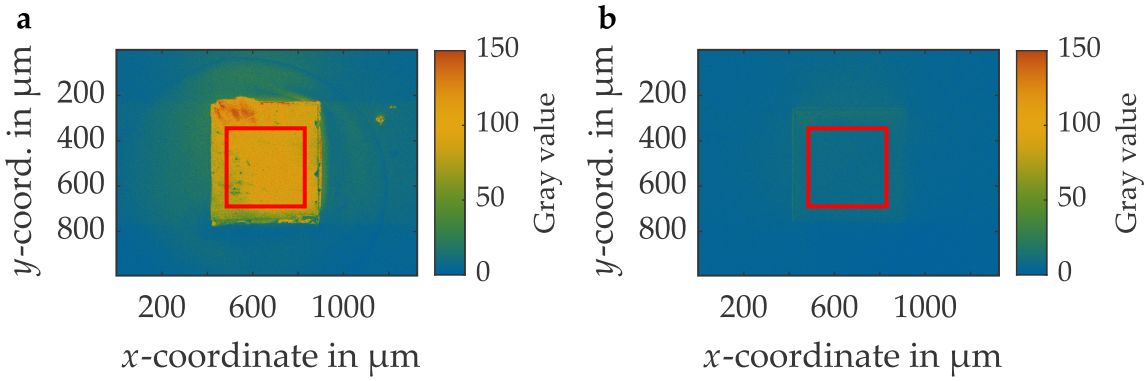

Figure 5.6: SEM luminescence images of blocks with a size of 500 µm × 500 µm × 500 µm. The block shown in panel **a** consists of the commercially available plastic scintillator EPS100, whereas the second block in panel **b** is 3D printed from the presented resist. The average gray values in the red marked squares are 93.1 for the EPS100 and 5.8 for the printed scintillator. The figure was adapted from [94].

EPS100 is given in the data sheet as 415 nm, whereas the emission wavelength of the printed scintillator is estimated from its fluorescence spectrum. Since the emission light is produced by a fluorescence process from the wavelength shifter as explained above, it can be estimated by exciting the scintillator with UV light (360 nm) and measuring the emission. The fluorescence spectrum under these conditions is shown in Figure 5.5. The spectrum is not symmetric leading to a difference between the peak wavelength (504.4 nm), and the average emission wavelength (519.5 nm). Taking all these information into account and subtracting a background measurement (see appendix Section A.4), the performance of the printed scintillator is given by 8.3 % for the peak wavelength or 11.2 % for the average wavelength. Overall, it can be summarized, that the light output of the 3D micro-printed scintillator is around 930 $^{\text{photons}}/_{\text{MeV}}$.

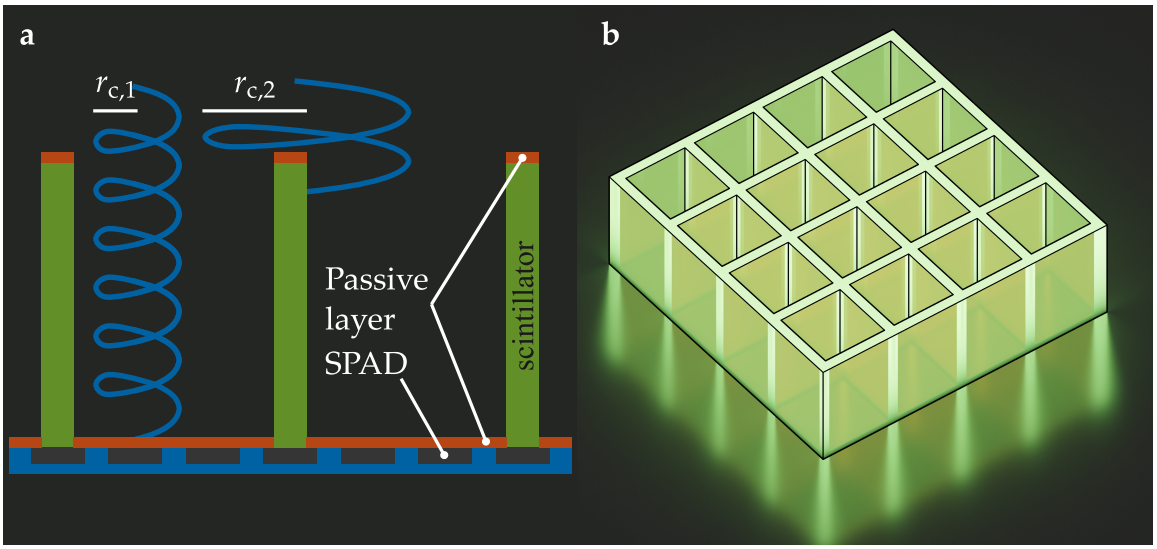

Figure 5.7: Schematic explanation of the principle of an active Transverse Energy Filter (aTEF). In panel **a** the scintillator pillars are shown. Two electrons approach with different transverse energy and thus, due to a not shown magnetic field, different cyclotron radii. The first cyclotron radius $r_{c,1}$ is smaller than the distance of the pillars to each other allowing the electron to hit the ground without touching the scintillator. Due to a passive layer, this electron does not create any signal. The second electron has a cyclotron radius $r_{c,2}$ which is larger than the distance between the pillars forcing the electron to hit scintillating material. The produced photons are then wave-guided inside the scintillator until they reach the SPAD and generate a detectable signal. In panel **b**, a 3D generalization of this concept is shown. The pillars are replaced by walls filling up the whole area in a square pattern. The figure was adapted from [94].

5.4 An active transverse energy filter as a possible application

One application for the presented custom scintillator is an active Transverse Energy Filter (aTEF) [55]. The goal is to detect only electrons with a large transverse energy and suppress the detection of electrons with a low transverse energy. This filtering detector system is beneficial in the KATRIN experiment since in that case background electrons show a small transverse energy, whereas the signal electrons come at larger transverse energies. The aTEF consists of scintillator walls connected to a detector array. The working principle is illustrated in Figure 5.7a. Two incoming electrons from the top propagating though a magnetic field which is perpendicular to the detector array surface. Therefore, the electrons fly on a spiral curve with certain cyclotron radii $r_{c,1}$ and $r_{c,2}$ which are both proportional to the corresponding transverse electron momentum. In this examples, let us assume that $r_{c,1} < r_{c,2}$. The scintillator walls have a constant distance to each other, which is significantly larger then $r_{c,1}$. Thus, the probability is high that the first electron with the smaller cyclotron radius is traveling in between two walls to the ground of the detector system. However, at this point a passive layer is deposited resulting in a suppressed detection of this electron. For the second electron, the cyclotron radius $r_{c,2}$ is larger then the wall distance leading to a high probability for the electron to hit the scintillator walls from the side. Thus, photons are generated which then travel down the scintillator wall, guided by total internal reflection, until they reach the SPAD detectors. Therefore, the second electron with the larger cyclotron radius, meaning a larger transverse momentum or energy, is detected, whereas the first electron with a small transverse energy is filtered out. For a generalizes scintillator geometry covering the whole detector area, the scintillator walls need to be arranged in a grid as shown in Figure 5.7b exemplary for a quadratic grid. Other grids, like hexagonal grids, are also possible.

For feasibility demonstration, such an aTEF structure was printed on a SPAD array, see Figure 5.8. In panel a, a light microscopy image of the detector array is shown where a grid is aligned to the detector's active areas (blue areas). The thickness of the walls is chosen to be 30 µm and the squares in between the walls have a side length of 185 µm. In panel b and c the printed structure is shown, again under observation with a light microscope. The alignment fulfills the requirement and the structure looks clear from the side. Only the stitching seams are visible and show the shear angle of 15° set in the printing program. The connection of the printed scintillator and the diodes as substrate works well without any delamination or micro explosions at the interface. Under the SEM (panel d), the square grid structure is clearly visible and again the surfaces are smooth, despite the stitching seams. This means that the total internal reflection is expected to

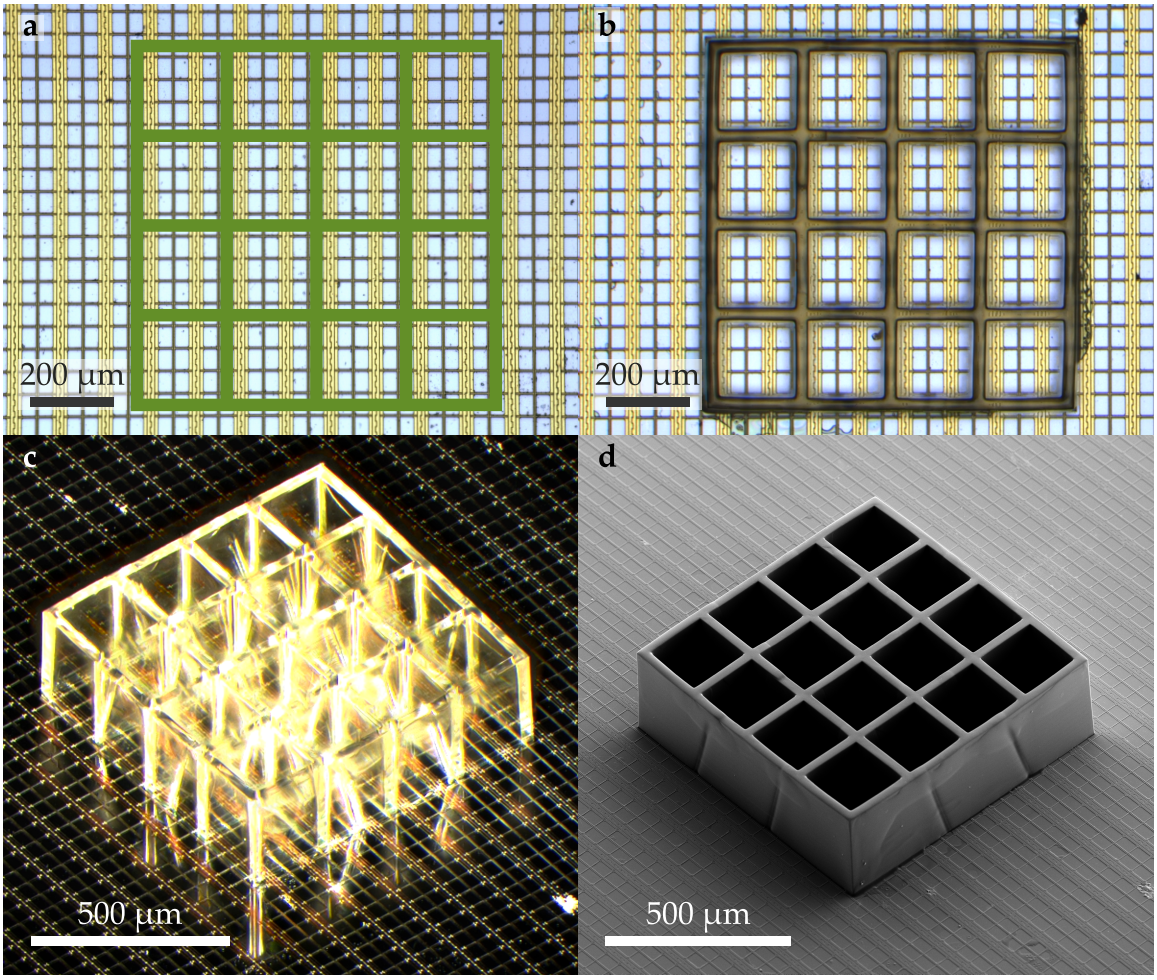

Figure 5.8: Demonstration of the capabilities to 3D print an aTEF structure on a SPAD-array. In panel **a** the target alignment of the aTEF grid with the SPAD array is shown. The walls should lay on the centers of the active areas (light blue). In panel **b** an optical microscope image of the printed structure is shown, following this alignment. The structure is also investigated under an angle with the same microscope (**c**). Additionally, the printed structure is investigated with an SEM showing the surface quality. Despite some clearly visible stitching artifacts at the sides, the surfaces are very smooth which is crucial for the wave-guiding application. The figure was adapted from [94].

work at high efficiency, but the stitching seams will lead to losses. For a further optimization aiming towards the application, improvements of the stitching seams should be considered. All in all, the detector system, providing an aTEF, is feasible with the presented printable plastic scintillator.

Summary

Motivated by an application from the KATRIN experiment, a two-photon printable scintillator resin was developed and presented within this chapter. The resin is composed out of two monomers providing a large density of aromatic systems. the monomers are combined with two wavelength shifters and a photoinitiator to be polymerizable via two-photon absorption. Additionally, print parameters, concerning the conventional two-photon printing, as well as two-photon grayscale lithography were determined.

Building up on that, the scintillation capabilities of the polymer were investigated. First, a qualitative demonstration of the scintillation effect was performed by hitting the scintillator with electrons in an scanning-electron microscope. The emitted photons were detected by a photodetector. The results were compared with the conventional photoresist IP-S in form of a chessboard with black (IP-S) and white (scintillator) figures. Additionally, the printed scintillator was compared with a commercial scintillator (Epic-Crystal, EPS100) to find its light yield to be around 930 $\mathrm{photons}/\mathrm{MeV}$.

Chapter 6

6 Conclusions and Outlook

Within this thesis, I described the full workflow of designing, fabricating, and testing of micro-optical elements for specific applications. The main focus was set to the improvement of single amino acid identification using Raman spectroscopy. Here, the main problem lied in the low signal intensity due to the low measurement time and only one molecule under investigation simultaneously. Therefore, the micro-optical elements were designed in a way that the benefits from the available photons were maximized. I achieved this goal with two examples. For a large detector array with 128 detectors, covering the entire spectrum, the signal yield was improved by a custom-made micro-lens array (MLA) focusing the signal light onto the active areas of the individual detectors. Thereby, losses were minimized.

While this approach is not new, the second approach brought more novelty. Here, the number of detectors was reduced drastically to only four detectors, which therefore delivered the same sensitivity at a lower total price. To cover up the disadvantage of their low number, each detector was fed with light from a specific optimized spectral region. The optimization, performed by collaboration partners from Cambridge, was done in such a way that the information about the amino acid under investigation was maximized. Hereby, it was extremely beneficial that the number of possible outcomes for amino acids is limited to 20. Based on that, a segmented-refractive optical element (SROE) was designed that selected the light from the optimized regions and coupled it into one optical fiber for each region. Then the fibers guided the light to the detectors.

Following to their design, I also presented the fabrication and optimization routine of the MLA and the SROE. The optimization of the elements was performed with a home-developed iterative precompensation routine, described in detail within my thesis. Additionally, I showed the optical characterization in experimental setups as close as possible to the final spectroscopy setup. The optical characterization for the MLA was performed by me alone, whereas the optical characterization of the SROE were performed in collaboration with Alba Viejo Rodriguez in the research group of Nicolò Maccaferri at Umeå. The results of both characterizations

were fitting with the expectations and the simulations, indicating that the two micro-optical elements will fulfill their task in the final spectroscopy setup within the EU project ProID.

Last, I presented 3D micro-printed plastic scintillators as a different class of micro-optical elements, generating light under incidence of electrons. The initial goal of this project was the fabrication of an improved detector for the Karlsruhe Tritium Neutrino (KATRIN) experiment. Therefore, a scintillator needs to be structured as an active Transverse Energy Filter (aTEF) [55], a structure consisting of walls with a thickness around 20 µm arranged in a grid with a wall distance around 200 µm, depending on the aimed at transverse energy filter level. The fabrication of such a structure is challenging due to the required feature size in combination with an target wall height above 300 µm. Many other techniques like etching do not allow for a reliable fabrication of walls with such a high aspect ratio. The problems can be overcome with 3D printing of plastic scintillators, however, state of the art (one-photon based) 3D printing approaches [52–54] of plastic scintillators do not provide the necessary resolution and surface quality. Therefore, together with Sebastian Kalt, Maximilian Bojanowski, Anton Huber, and other group members of the group of Guido Drexlin, I developed a novel two-photon printable photoresist with scintillator capabilities. I demonstrated the scintillation effect qualitatively and also quantitatively by comparing it to a well-established commercially available plastic scintillator. The measurement of the scintillation effect was performed in a scanning-electron microscope (SEM), where the emitted light from the sample, under incidence of electrons from the e-gun, was measured with a photo-detector in the microscopy chamber. Last, I demonstrated the feasibility of the fabrication of the aTEF structure by printing a dummy sample directly on a single-photon avalanche diode chip. The success of this experiment encourages for further experiments towards a fully integrated working detector system.

In the following, I give a brief summary over the individual chapters of my thesis, followed by an outlook of a possible future developments of the individual topics.

In Chapter 2, I showed the theoretical foundation for the description of the demonstrated refractive optical elements for the application within a Raman spectrometer. Based on the concept of a constant optical path length for the incoming light to a focus point, the shape of an ideal lens, or more precise a focusing element, is derived and mapped onto the equation for an aspheric lens. Thus, the two parameters describing an aspheric lens surface, the conic constant and the inverse radius of curvature at the center, are derivable from the given material's refractive index and the geometrical boundaries. This analytic relation

is later used for the derivation of the MLA. Additionally, the broader concept of refractive freeform surfaces is discussed. For rays inciding in parallel direction, based on Snell's law, a set of partial differential equations (PDEs) is derived. For each ray, the position at which it should hit the canvas is given as a boundary function and the set of PDEs is solved accordingly. This formalism is later used to obtain the surface topography of the SROE. To directly test the derived designs, wave-propagation simulations are introduced at the end of the chapter, which are performed for every design presented in the thesis.

I described the fabrication routine for the micro-optical elements in Chapter 3. At first, I explained the concept of 3D laser micro-printing and the related workflow in the lab. I introduced all the necessary technical terms to be able to understand and reproduce the relevant steps for the fabrication of the presented samples. Furthermore, as a mean to improve the surface quality and shape accuracy of the printed topographies, I explained the concept of two-photon grayscale lithography, which is exclusively available for the Nanoscribe QuantumX printer. Thus, this printer was used for the fabrication of the samples presented in this thesis. As a last step of the fabrication, I presented an iterative precompensation routine, developed by me together with Sebastian Kalt, Pascal Kiefer, and Pascal Rietz. While this routine basically already covers a characterization and optimization aspect, we all consider it as very basic and easy to implement. Thus, we see it as a part of the fabrication routine for most optical elements.

As mentioned above, the aimed at application for the presented refractive optical elements is in a Raman spectrometer. Therefore, in Chapter 4, I described first the main concept of Raman spectroscopy and how it can be used to identify single amino acids in a protein. Based on that, I introduced the MLA as a first example of how the signal can be improved for a large detector array covering the whole spectrum. For this application, the analytic description of an ideal aspheric lens form from the second chapter was used. The MLA design was first verified by simulations and then the fabrication and experimental characterization was explained. I described two different approaches to characterize the MLA, first the measurement of the topography, which was then compared to the design topography. This had to be done anyways in order to perform the iterative precompensation. Within this characterization, the improvement of the surface accuracy with increasing number of precompensation became visible. Second, I showed an optical characterization made in an optical test setup. With the optical characterization the improvement due to the precompensation was visible again. As a result, the optimized optical element produced a row of equidistant spots, as desired from the application.
The second example is the SROE, focusing light from four optimized spectral regions onto the end of one optical fiber each. I presented the optimization routine

of the spectral regions, performed by Bikash Kumar Bhandari under the supervision of Nick Goldman. I applied the result to the formalism for the freeform surface described in the second chapter and derive the surface topography. Again, optical simulations proved that the SROE fulfilled the requirements. Similar to the the MLA, an optical characterization was performed, where the signal Raman light was mimicked by continuous white light, which was split into its spectral components - the same way as it would in a Raman spectrometer. Thus, not only the images of the produced spots were analyzed, but also the spectra of the light emitted from the end of each fiber was measured. These spectra matched the designed spectral regions, indicating that the fabrication of the SROE was successful. An iterative precompensation of the SROE did not improve its optical capabilities significantly, which is why this aspect is shown in the appendix.

In Chapter 5, I switched to a different class of optical elements and described the 3D micro-fabrication of plastic scintillators. Motivated by an application of the KATRIN experiment, a two-photon printable scintillator photoresist was developed. I named the used chemical components and discussed the advantages and disadvantages of each of them. Additionally, the mixing procedure of the resist was described. For the application, it was necessary that the generated light was guided by the structure through total internal reflection. Thus, optical grade surface qualities were necessary. This was achieved using the benefits of two-photon grayscale lithography (2GL) as described in Chapter 3. To be able to use this technology, a 2GL profiles needed to be generated to print the scintillator with suitable parameters. I described the procedure of estimating the correct parameters and achieved surface roughness of below 30 nm.
To demonstrate the scintillator's capabilities, it was analyzed in an SEM measuring the emitted light with a photodetector in the SEM chamber. Thus, I first showed a qualitative demonstration of the scintillation effect from a chess board sample. Here, one could clearly see, that the scintillator generates light under incidence of electrons, whereas conventional IP-S did not. However, I also quantified the scintillators capabilities by comparing it to a commercially available scintillator (Epic-Crystal EPS100). For that, a calibration of the photodetector was necessary, which I showed in the appendix. As a result, the light yield of the custom made scintillator was found to be around 930 $\mathrm{photons/MeV}$. Finally, I also showed the printability of the required aTEF structure for the KATRIN experiment directly on a single photon avalanche diode array chip. This successful, even if not perfect, print example demonstrated the possibilities of applying this scintillator in future (particle physics) experiments.

Outlook

In the future, the improvement of the efficiency of single amino acid identification inside proteins will be topic of further research. Looking at the common problems discussed within this thesis coming along with those experiments, the main issue is always the small number of photons emitted by the amino acid under investigation. Therefore, I expect most future research targeting this issue. There are several approaches thinkable:
First, improvements can be made at the specimen side. Here, especially the translocation time of a single amino acid through the nanopore is a critical factor that can increase the number of photons gained by one amino acid by increasing this translocation time. The slowing down of the amino acids inside the nanopore has already been investigated intensely [99–101] and will most likely be the topic of many research projects in the future, too. However, this approach cannot be exploited unlimited due to potential destruction of the amino acid by bleaching.
Second, it is important to guide the emitted photons with a high efficiency toward the detector. Since every interface in the beam path leads to losses due to reflection, it is beneficial to use as few optical elements as possible. For the inevitable optical elements, a high transmission rate is crucial. While commercially available optical elements often come with very high transmission rates, due to anti-reflection coatings (AR coating) and high quality materials, this is not necessarily the case for the custom-made micro-optical elements presented within this theses. However, AR coatings can be applied to the 3D printed structure and the back side of the glass substrate, too. Two possibilities are physical vapor deposition [13, 102–104] or atomic layer deposition [105, 106]. Both possibilities reduce the reflection from about 4 % per interface below 1 % per interface.
Another way to increase the transmission is the material of the micro-optical element itself. While the glass substrate already provides a high transmission rate for visible light, the same is not necessarily given for the 3D printed material. For IP-S, used within this thesis, the extinction coefficient in the visible region is around 10^{-4} [91] which leads for a wavelength of 600 nm and a material thickness of 20 µm already to a loss of 2 % of the photons. Thus, especially for even thicker samples, it is useful to invest in more transparent materials. Two possibilities are the resist IP-Visio [107] or IP-n162 [108] sold by Nanoscribe, which already deliver a lower absorption [109]. Recently, even the possibility of glass printing using a minimal invasive post baking process arised, which gives hope for an even higher transmission rate [110] and better shape accuracy in comparison to previous glass printing approaches using a high temperature sintering process [111–113].
Additionally to the increasing of the number of signal photons reaching the detector, the reduction of noise photons, confusing the evaluation algorithm, is also of high interest. Here, especially a shielding of the detectors against other light

sources is relevant. One possibility is the vaporization of a metal film onto the substrate of the micro-optical element, in which a rectangle is etched out in the center to print the MLA or SROE in. Thus, light hitting the substrate at positions where no optical element is printed would be blocked by the metal film, whereas the transmission though the micro-optical component itself would remain high. First experiments concerning this approach were already performed within this thesis, however, due to a lack of time, this feature was not included in the final samples and therefore not described. For future samples with a higher demand in noise reduction, this approach could be included again.
Last, in case of the SROE selecting optimized spectral regions, the optimization of the spectral regions can be improved in the future, too. As already shown at the end of Section 4.3.4 some of the aimed at spectral regions were too small for the resolution of the imaging system. This boundary could be included in the optimization process for an improved version. Additionally, one could think of removing some other unnecessary boundaries set to the spectral regions. First, it is not necessary, that one spectral region associated with one detector is continuous. In fact, light from several intervals, distributed over the whole spectrum, can be focused onto one optical fiber or one detector. By that, the optimization routine gets more degrees of freedom enabling a possibly higher performance. Another restriction that could be removed is the fact, that the spectral regions may not overlap. By fabricating diffractive optical elements instead of refracting optical elements, it is possible to distribute photons from one spectral regions over several detectors with controllable probabilities. Here again, the increased degrees of freedom for the optimization could potentially lead to a solution with a better performance. However, it needs to be analyzed if this possible improvement is large enough to justify the additional experimental effort of integrating diffractive optical elements into the SROE.
If the goal is only the identification of the protein without measuring the complete sequence of amino acids, is is also sufficient to concentrate on two or three amino acids and measure their positions in the amino acid sequence with a high precision [114]. An optimization of the spectral regions for this approach leads to higher identification probabilities as shown in the appendix in Section A.2.

Concerning the 3D micro-printed plastic scintillator, I see two main topics for improvement in the future. First, the light yield of only 930 $\mathrm{photons/MeV}$, as described in Section 5.3.2, is poor in comparison to other plastic scintillators like the Epic-Crystal EPS 100 used for comparison (9750 $\mathrm{photons/MeV}$). To work on this issue, it is probably inevitable to try different monomers or monomer combinations and compare the resulting performances. As suggested by the literature [54], it is very promising to use monomers with a higher density of aromatic systems. For the case presented in this thesis, it might already improve the performance to lower the molar mass of the bisphenol A ethoxylate diacrylate and thus effectively

increase the density of the aromatic systems in the polymer. Additionally, it is important to ensure that the generated light is not reabsorbed in the material. Therefore, also the choice of the used photoinitiator can play a role since its absorbance is often in the spectral region of the first generated photons. While in this thesis only two different photoinitiators were tested, see Section A.5.2 in the appendix, there are many more available which might have a larger effect on the scintillation capabilities.
The second major improvement that can be aimed at for the further research of 3D micro-printed scintillators is the increase of printing resolution. The presented scintillator suffered from a large proximity effect avoiding the printing of very fine structures below micrometer resolution. On the other hand, some applications in photonics require such resolutions [56]. In the cited example, structures smaller than the wavelength of the emitted light can be used to increase the scintillators light yield by manipulating the local density of optical states. However, even with a resist supporting a lower proximity effect and even an objective lens with a larger numerical aperture, it will be hard to print structures smaller than the emission wavelength of 500 nm or, even worse, half of this wavelength. Here, the reduction of the writing laser's wavelength, as for example with novel two-step lithography approaches might help [115–117]. Another possibility is the use of STED inspired laser-lithography systems [118, 119]. It will be an interesting development if and how such nano-structured scintillators are used in the future. In any case, I see a lot of potential in the 3D laser micro-printing of plastic scintillators for many applications.

Appendix A

A Appendix

A.1 Quantification of uncompensatable errors in printing micro-optical elements

As already described in Section 3.2 an iterative precompensation improves the shape accuracy of printed micro-structures. However, this only works for deviations that originate from systematic errors. The remaining, statistical, errors cannot be compensated and remain in every print leading to a limit of the reachable quality. Therefore, it is of interest to evaluate the statistical errors and compare them to the reached accuracy after performing the precompensation. If the deviations of the precompensated and printed structure with respect to the design is comparable to the deviations originating to the statistical errors of the system, no further improvement can be expected from more steps of precompensation.

To quantify the statistical errors, 10 MLA samples after two steps of precompensation were printed on the same substrate and measured 10 times each with the confocal-optical microscope resulting in 100 measured topographies. Each topography was analyzed in the Quandalf program and the histogram of the difference maps, with respect to the design, were generated. The histograms are shown in Figure A.1. Even though the fabrication and measurement conditions for each histogram were similar, the histograms differ in their width and shape to each other, indicating, that various statistical errors are significant.

To be able to distinguish different statistical errors sources in the next step, the topography of the 6th MLA sample, measured for the 6th time, was used as a fake design in Quandalf and all other topographies were compared with this fake design in a second round. The new histograms are shown in Figure A.2. Obviously, the histograms in column and row 6 is only one bar at zero difference, since the topography was compared with itself. The remaining deviations, indicated by the figures of merit of $\sigma = 12.5\,\text{nm}$ and $\mu = 2.5\,\text{nm}$, result from the fact,

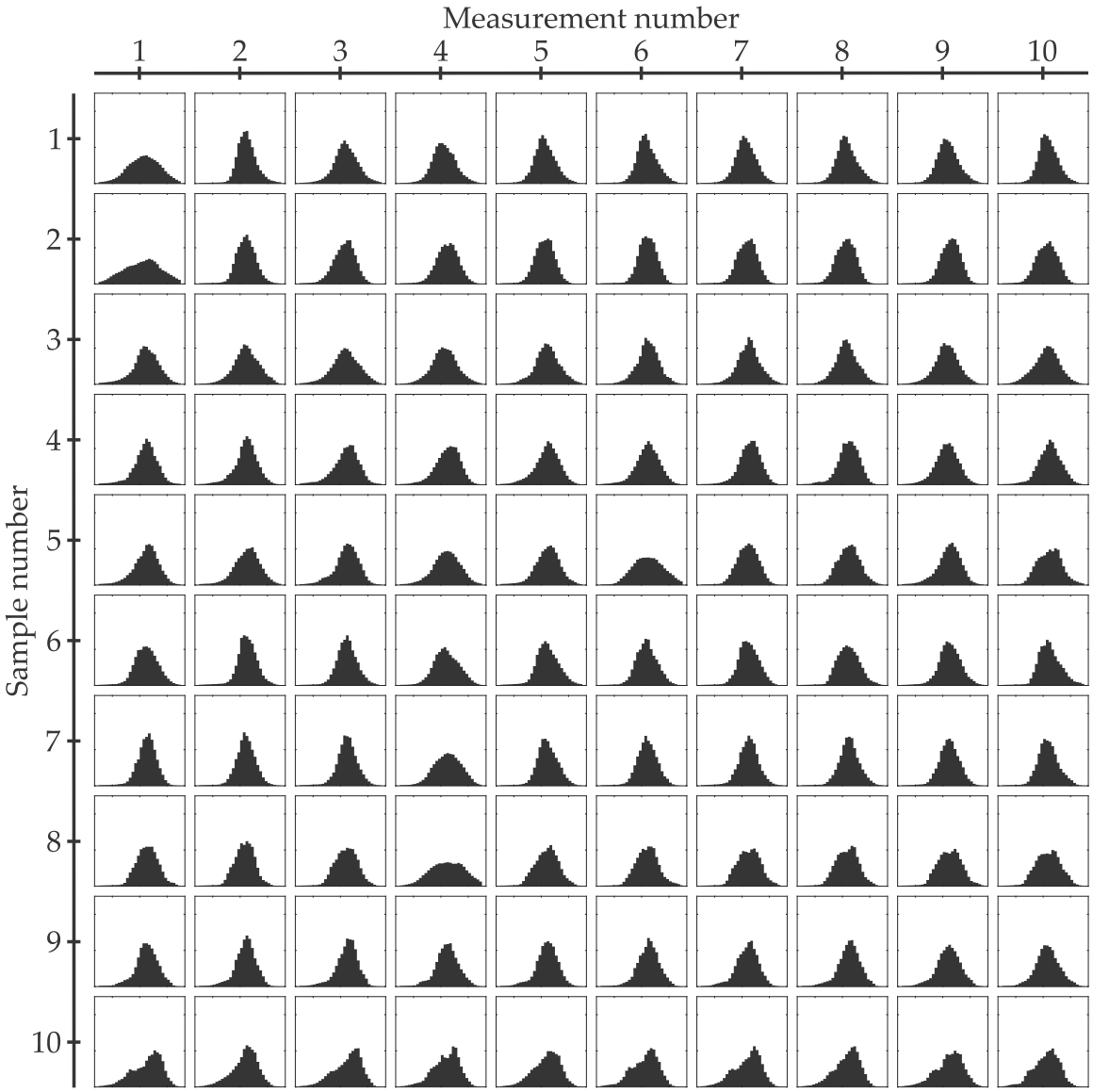

Figure A.1: Estimation of the statistical, uncompensateable errors when 3D printing micro-optics. Ten micro-lens arrays after two-steps of precompensation were printed and each micro lens array was measured ten times. All resulting 100 histograms of the difference to the design are shown in this figure. The differences between the histograms result from different statistical errors during the printing or measurement process. The figure was taken from [37].

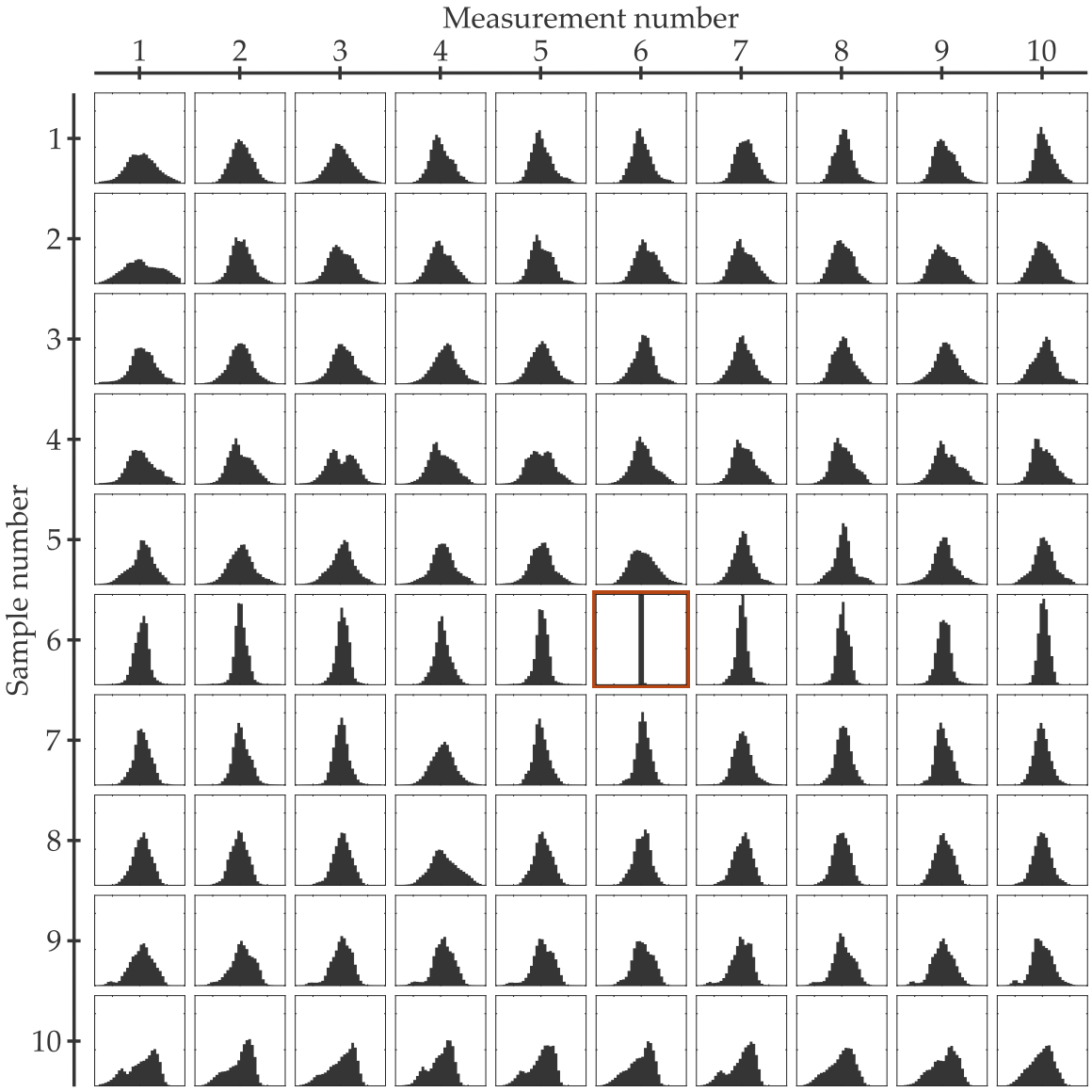

Figure A.2: Distinction of the statistical, uncompensateable errors when 3D printing micro-optics from different sources. The same 10×10 topographies as in Figure A.1 are now not compared to the design, but to the 6th sample measured for the 6th time. Therefore, the histogram marked with the red square is a perfect peak since the height topography is compared with itself. Additionally, one can now say, that the remaining histograms for the 6th sample only show the statistical deviation from the confocal-optical measurement, since the sample always stayed the same. The figure was taken from [37].

that the different resolution of the exported cropped fake design differs from the topographies. Therefore, the rotation, shrinkage, and lateral positioning is not optimal. Looking at the remaining 9 measured topographies of the same sample number 6, the histograms appear narrower in comparison to the histograms from the remaining samples. This comes from the fact, that from sample number 6 only the statistical errors from the confocal-optical microscope are relevant. The average values over the figures of merit over these remaining 9 topographies associated with sample 6 is $\sigma = 107.3\,\text{nm}$ and $\mu = 27.1\,\text{nm}$. These values give a quantification of the statistical error of only the confocal-optical microscope. Last, the combination of the two devices, printer and microscope, are quantified by looking at all histograms despite in row and column 6. The averaged figures of merit over these 81 topographies are $\sigma = 109.1\,\text{nm}$ and $\mu = 40.1\,\text{nm}$. Especially the increase in μ is significant and indicates relevant statistical errors during the printing process. One example of such error sources is the interface finder of the printer which only has a limited accuracy for each writing field. To gain further improvement, thus, these error sources during printing and measuring the topography need to be minimized.

Last, the latter figures of merit including all statistical deviations can be compared with the figures of merit for the second precompensation in Section 4.2.2 ($\sigma = 76.5\,\text{nm}$ and $\mu = 36.6\,\text{nm}$). These values are smaller, since they result from averaged measured topographies canceling out some of the statistical deviations. Still, they are in the same order of magnitude, indicating, that the achieved surface accuracy is close to the achievable limit.

A.2 Optimization of the spectral region for a subset of amino acids

As mentioned in Section 4.3.1, the optimization process for the spectral regions can be restricted to only a subset of amino acids. The knowledge of the positions of only two or three amino acids in a protein is already enough to identify the complete protein when comparing it to a database with a decent accuracy [114]. As an example, the optimization is performed to identify the amino acids Luecine and Serine with the highest possible probability on average without taking into account the remaining 18 amino acids. The results are shown in Figure A.3 for different numbers of detected photons emitted by Serine. In this example, the $M1'$ improves by 8.9 % when comparing the optimized spectral regions with the uniformly separated regions for the case of $T = 100$. Due to the flexibility of the protocol exploiting the SROE presented in this thesis, the following steps for the design and fabrication of the SROE would be the same.

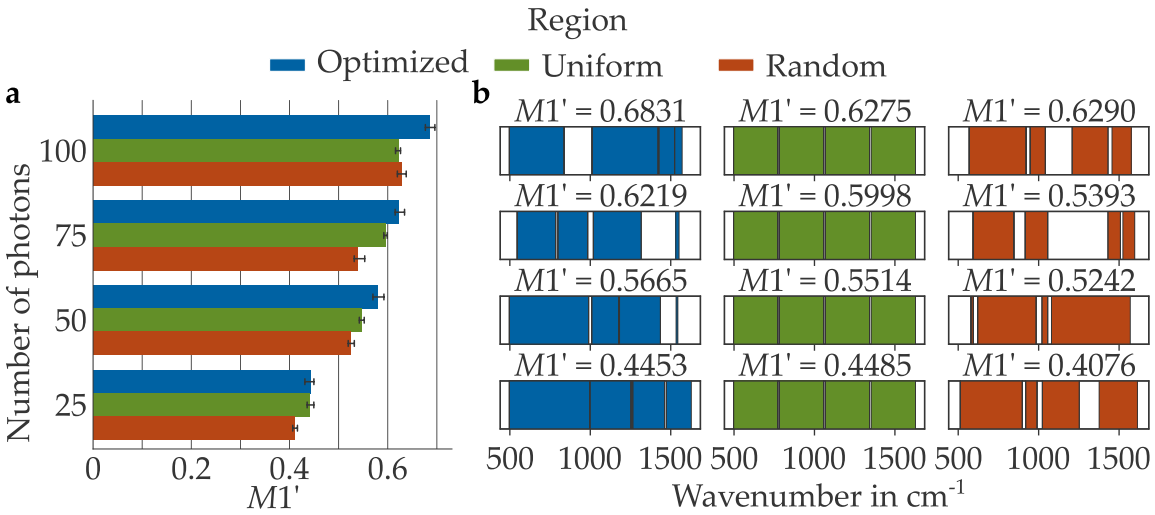

Figure A.3: Different spectral regions and the corresponding $M1'$ value for the correct identification of the two amino acids Leucine and Serine. Here, $M1'$ is the mean of the diagonal of the 2×2 confusion matrix. For the case of 100 detected photons emitted by Serine, the probability for a correct identification is 39 % for Leucine and 97 % for Serine ($M1' = 0.683$). The figure was taken from [68].

A.3 Influence of iterative precompensation for the NIR-SROE

As announced in Section 4.3.4, also for the SROE a precompensation optimization was performed. Again the topography for 4 printed samples is measured using a spinning-disk confocal-optical microscope. All measurement data were analyzed with Quandalf and averaged over the 4 samples. The difference for each status of precompensation is is shown in Figure A.4. It is visible for the difference maps, that the surface accuracy improves with increasing steps of precompensation, since the differences become more even. Additionally, this fact can be seen at the histograms connected with the difference values. The peaks become narrower with increasing number of precompensation. Note that a shift of the peak to the left or right does not matter, since a constant offset of the optical element has no influence. Only the width of the peak matters. Therefore, it can be concluded, that the precompensation improves the shape accuracy of the SROE.

Additionally to the pure topography characterization, also the optical performances of the SROE should be analyzed with respect to the iterations of precompensation. As already explained in Section 4.3.4, the SROE samples were

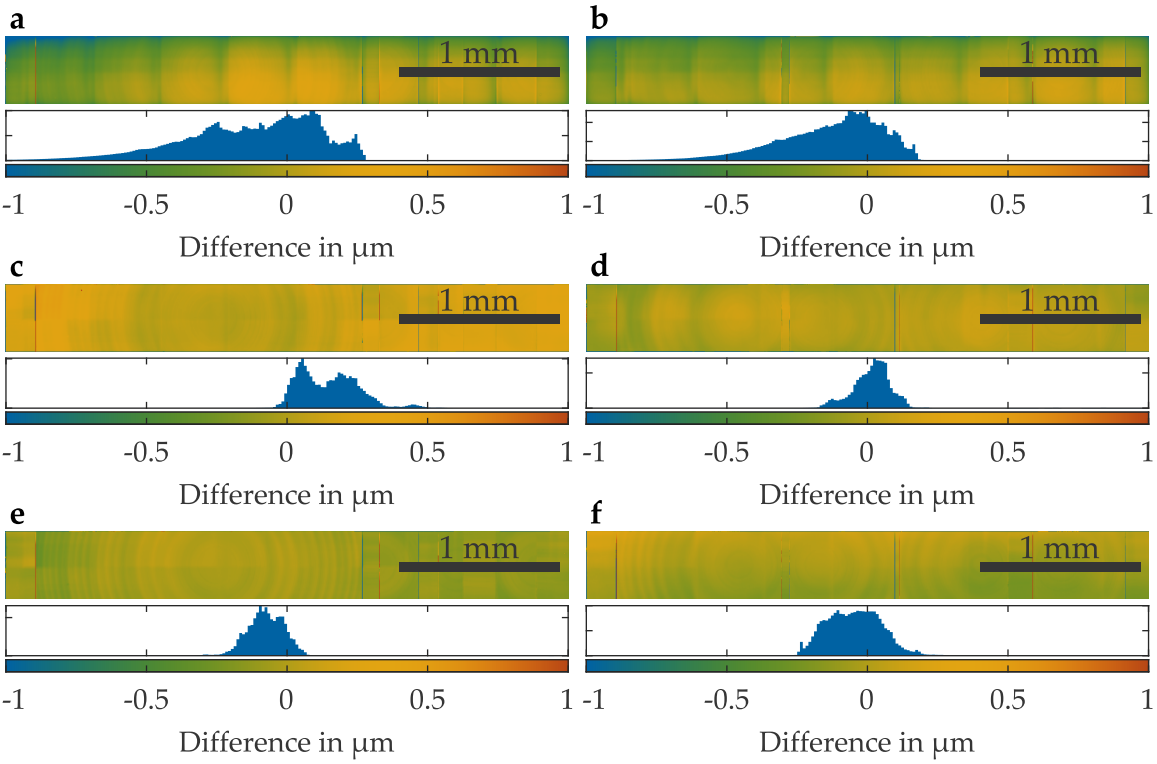

Figure A.4: Difference maps of the SROE after different iterations of precompensation. In panel **a** (100 photons) and **b** (50 photons) the difference maps with respect to the design and the corresponding difference histograms of the first, uncompensated print is shown. In panel **c** and **d** one step of precompensation was applied and in panel **e** and **f** two steps of precompensation were applied. The histogram peaks become narrower after one step of precompensation and remain at their width for the second step, indicating a quick saturation. The figure was taken from [68].

illuminated in a test setup and the foci produced by the SROE were captured with a camera first. The taken camera images of different status of precompensation are shown in Figure A.5. While the images without any precompensation performed are the same as already shown in Section 4.3.4, the images concerning the samples with one or two steps of precompensation look similar to a point, were one could not tell them apart. This indicates that even though the surface accuracy improves with the iterative precompensation, this is not necessarily the case for the optical performance. Indeed, on can conclude that the shape of the foci is robust within the SROE shape tolerances that are already achieved after the first print.

For the sake of completeness, also the spectra of the light from the four foci are measured as described before in Section 4.3.4. The results are shown in Figure A.6. Again, the two spectra without the precompensation are the exact same as in the main text. However, as already noted from the camera images, also the

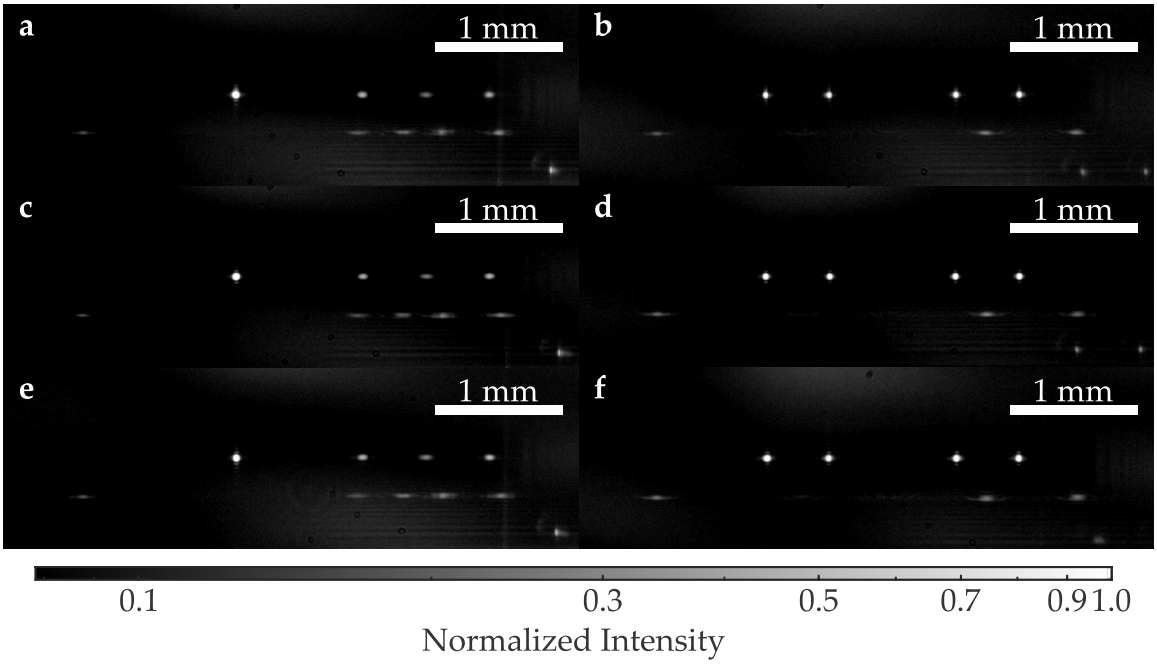

Figure A.5: Camera images of the four focal spots produced by SROE samples in the optical test setup. In panel **a** (100 photons) and **b** (50 photons) the images are shown for a sample without any precompensation. These images are the same as the ones shown in Figure 4.13. Panel **c** and **d** show the images for samples after one step of precompensation and panel **e** and **f** after two steps of precompensation. The absence of a notable differences between the images from different precompensation steps indicate that the precompensation routine might not be so crucial for these kind of samples as in contrast for the micro-lens array from Section 4.2. The figure was taken from [68].

spectra did not change let alone improve after applying the precompensation. This again indicated, that even the first print has a sufficient quality for the task that is demanded from the SROE.

One reason for the robustness of the SROE in comparison to the MLA is, that the working distance of the SROE (15 mm) is a lot higher then the one from the MLA (2 mm). This results in a lower numeric aperture and therefore also a higher Rayleigh range of the focused light. Thus, small deviations in the focal length do not lead to strong deviations. Additionally, the target size is larger in the case for the SROE. While the active area the MLA was focusing the light on only had a size of 30 µm, which was close to the diffraction limit, the core diameter of the fibers the SROE should couple the light in is at 400 µm.

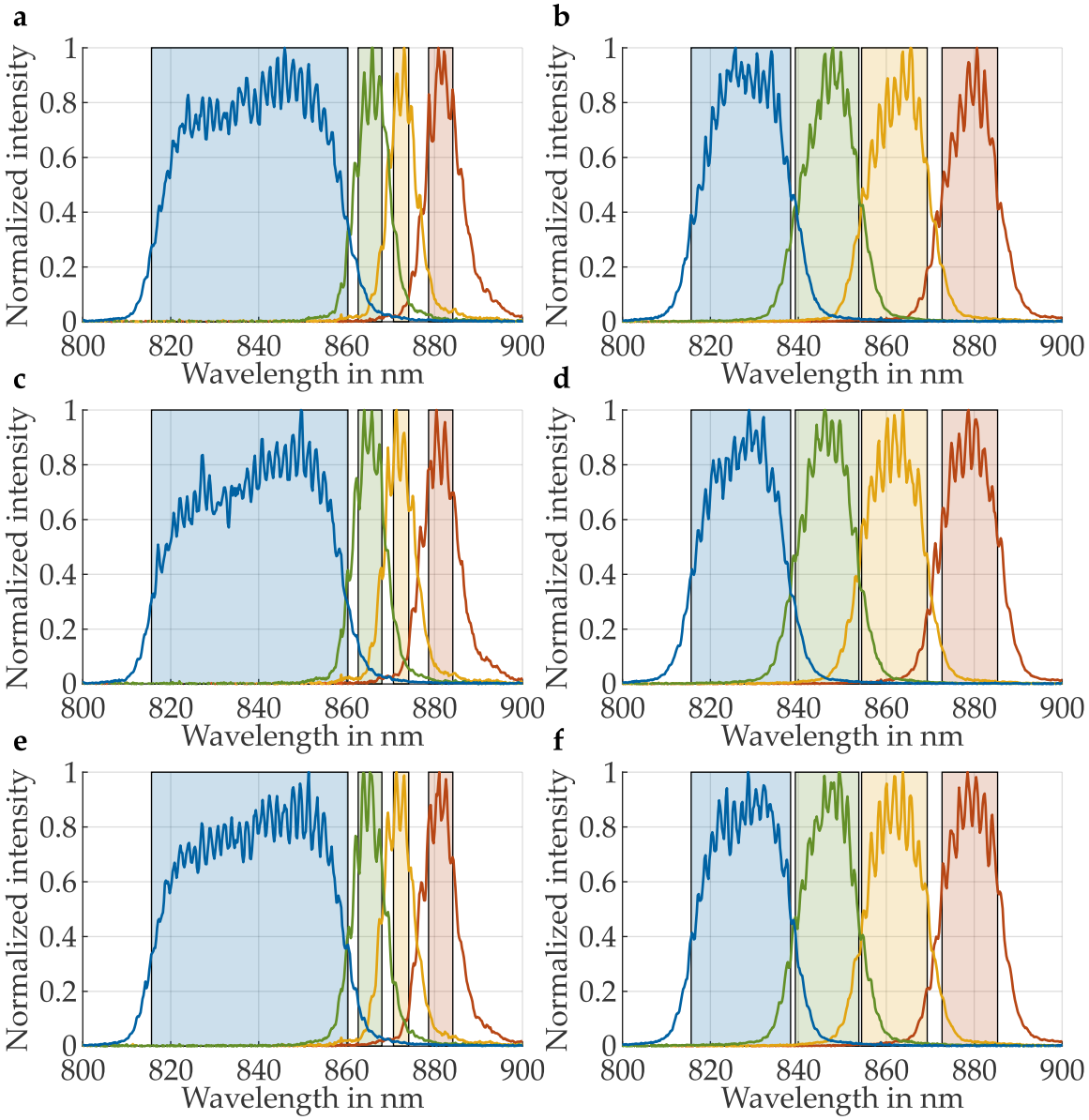

Figure A.6: Recorded spectra from the light emitted by the four optical fibers in the test setup for samples with different number of precompensation. The first two panels **a** (100 photons) and **b** (50 photons) show the spectra obtained while using the sample without any precompensation. These spectra are identical with the ones presented in Figure 4.13. Panel **c** and **d** show the spectra recorded when testing samples treated with one step of precompensation while panel **e** and **f** show the spectra from samples after two steps of precompensation. As for the camera images in Figure A.5, there is no major difference between the number of precompensations, indicating that this structure does not depend so strongly on the precompensation routine as other micro-optical elements. The figure was taken from [68].

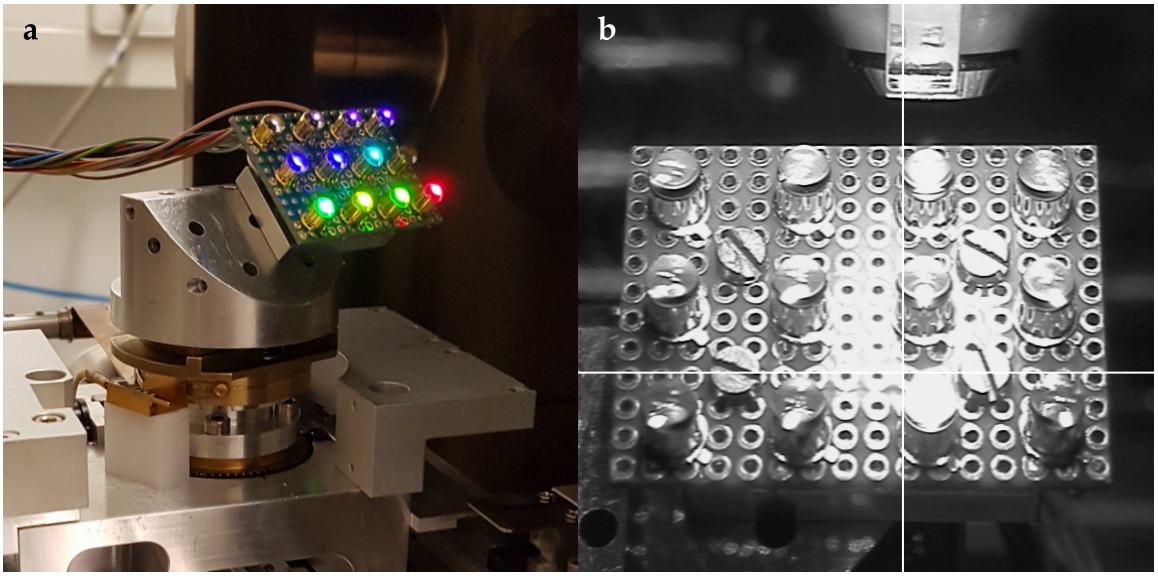

Figure A.7: Electric board with 12 LEDs inside the SEM chamber for the VPSE detector calibration. The board can be seen as a color image in panel **a** and contains 12 LEDs at different wavelengths (375 nm, 385 nm, 395 nm, 405 nm, 430 nm, 450 nm, 490 nm, 505 nm (not working), 525 nm, 545 nm, 570 nm, 645 nm). The board is mounted in the movable stage of the SEM and aligned before each measurement, so that the relevant LED is always at the same position (see panel **b** for the 570 nm LED), using the optical camera in the SEM chamber. The camber illumination was deactivated for the measurement itself.

A.4 Wavelength calibration of the VPSE detector used in the SEM

Since no model number of data sheet was available for the VPSE photon detector built in the used Zeiss VP55 SEM, a measurement of the wavelength dependency needed to be done. The reason for this is, that the emission wavelength of the custom made scintillator differs from the one of the commercially available scintillator. Thus, the gray values of the obtained images in Section 5.3 cannot be compared directly. Additionally, the dependency of the image gray value with the light intensity of the light source has to be analyzed.

Therefore, 12 LEDs (11 of them working) with different wavelengths were soldered onto an electric board and put into the SEM chamber (see Figure A.7). Each LED can be turned on and off, controlled from outside of the SEM. Additionally, the voltage applied to all turned on LEDs can be controlled using a lab power supply unit (Tenma 72-13350). Using the chamber camera of the SEM in combination

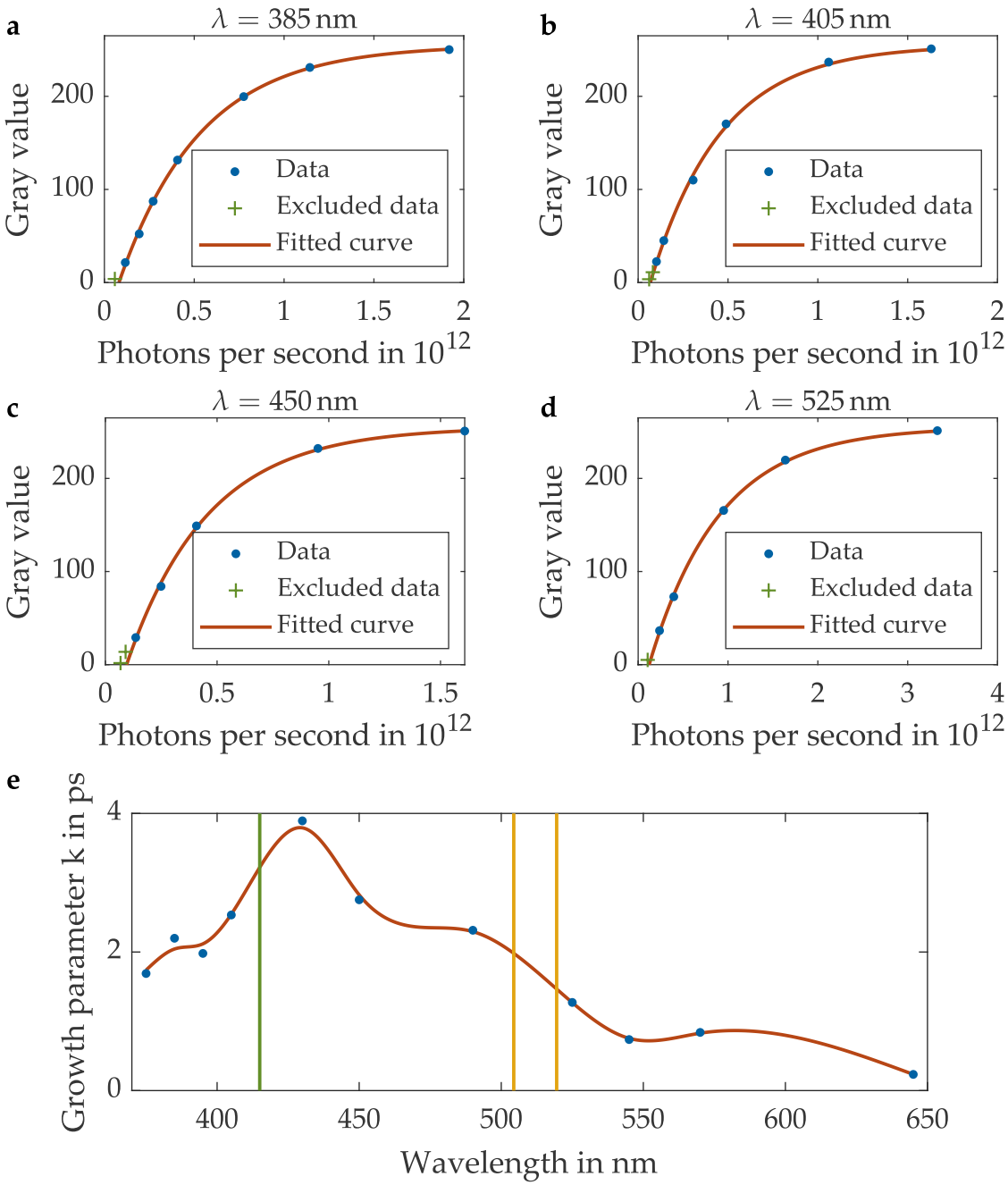

Figure A.8: Power dependency of the gray value and sensitivity curve of the VPSE detector. Panels **a** - **d** show the gray value in dependency of the number of photons emitted by an LED for different wavelengths. For each, a saturation model was fitted. In panel **e**, the growth parameters resulting from these fits are plotted against the wavelength showing the spectral sensitivity of the VPSE detector. The figure was taken from [94].

with the movable sample stage, it is possible to bring the LED under investigation always to the same position. The electron beam was shut down for the whole measurement. Now, VPSE images were taken for different values of the voltage at the LED for each wavelength. Afterwards, the average gray value of each image was calculated. In a second measurement, the optical output power from each LED was measured using a calibrated optical power meter. Thus, the gray value becomes available in dependency of the optical power and, since the wavelengths are known, also in dependency of the emitted number of photons per second. 4 out of these 11 data curves are shown in Figure A.8 a - d. Note, that the number of emitted photons is not equal to the number of photons reaching the photodetector, since most photons emitted by the LEDs in the SEM chamber will be emitted in other directions then toward the detector. At the gray value curves, it becomes clear that the gray value does not scale linearly with the number of emitted photons per second, but follows a saturation curve. Therefore, the gray value G is modeled by a growth model in dependency of the number of emitted photons N as

$$G(N) = 255 \cdot \left(1 - e^{-k \cdot (N - N_0)}\right) , \tag{A.1}$$

where k is the growth parameter and N_0 describes an offset in the optical power stemming from an insufficient zeroing of the optical power meter. Since this error is thereby eliminated, the number of photons will be denoted by $\tilde{N}$ in the following which corresponds to $N - N_0$. Both model parameters are evaluated by a least square fit. Thus, the parameter k becomes available in dependency of the wavelength and describes the detectors sensitivity. The sensitivity curve is shown in Figure A.8e. The individual points are interpolated by a smoothing spline with a smoothing parameter of 0.01 using the Matlab fit function, to obtain the function $k(\lambda)$. For the sake of overview, the emission wavelength of the commercially available scintillator (Epic-Crystal, EPS100) is marked with a green line, and the emission peak and average wavelengths of the custom scintillator are marked with a yellow line.

For a quantitative comparison between the two scintillators, the measured gray values need to be back transformed to the emitted photons. Therefore, first, the background signal, introduced by the activation of the electron beam in the SEM, needs to be subtracted. Since the electron beam was turned off during the LED measurement, these data do not contain this background. Thus, an VPSE image was taken under the same conditions as for the scintillator measurements, but the sample was only a metal plate. The average background gray value was found to be $G_b = 2.4$. Using that and the inverted growth model from Equation A.1, the

number of emitted photons is obtained as

$$\tilde{N}_i = \frac{-1}{k(\lambda_i)} \cdot \log\left(1 - \frac{G_i - G_b}{255}\right) . \tag{A.2}$$

Note again that these numbers do not describe the exact number of emitted photons per second for the two scintillators, but are proportional to them. Therefore, the ratio between $\tilde{N}$ for the custom made scintillator and $\tilde{N}$ for the EPS100 is equal to the ratio of their efficiencies. For the peak fluorescence wavelength of the custom made scintillator (see Figure 5.5 in Section 5.3), this ratio is 8.3 %, and for the average fluorescence wavelength 11.2 %. These are the numbers, which lead approximately to the light yield of 930 photons/MeV, presented in Section 5.3.

A.5 Variation of the ingredients of the scintillator resist

In this section, the influence of two major components of the scintillator resist on the scintillation effect should be analyzed. To be precise, the concentration of 1-naphthyl methacrylate is varied with a simultaneous analysis of the light output to justify the decision to used a concentration of 20 % for the main recipe. Second, the influence of the photoinitiator DETC should be investigated by replacing it with the photoinitiator Irgacure-819 and comparing the light output of both mixtures.

A.5.1 Variation of the concentration of 1-naphthyl methacrylate

To identify the effect of the concentration of 1-naphthyl methacrylate on the scintillation capabilities of the resist, a study was performed with 3 recipes with different concentrations of 1-naphthyl methacrylate. With each recipe, a set of block with different printing parameters was printed and analyzed in the SEM under observation of emitted photons. The electron energy was set to 12 keV. The results are shown in Figure A.9. It becomes clear that for a concentration of 20 % the light output increases in contrast to the recipe without any 1-naphthyl methacrylate. However, also the polymerization threshold increases making more laser power necessary to print a fully polymerized block. This is also the reason why a further increment of the concentration of 1-naphthyl methacrylate does not improve the situation further. Indeed, with a concentration of 40 % no well defined blocks can be printed anymore making the resist useless for most applications. The decrease of light output in this case can also be explained by the insufficient polymerization since main components of the scintillator, as for example the wavelength shifters, are likely to be solved out of the unstable

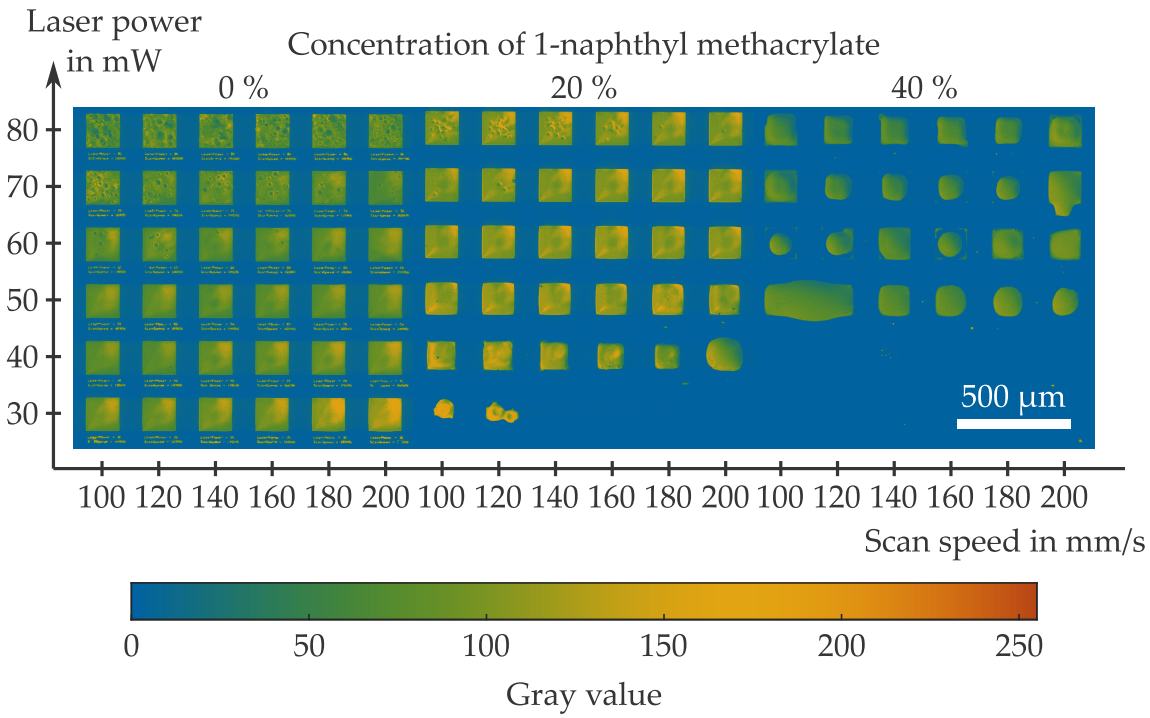

Figure A.9: Determination of the scintillation effect with the different concentrations of 1-naphthly methacrylate. Nominally identical block were printed with different laser power an scan speed. For each set of block the concentration of 1-naphthyl methacrylate was changed. The slice distance was generally set to 0.5 µm and the hatch distance to 0.3 µm. The figure was taken from [94].

polymer matrix during the development process. Therefore, a concentration of 1-naphthyl methacrylate of 20 % seems to be a good compromise and is thus used for the scintillator recipe presented in Section 5.1.

A.5.2 Replacement of the photoinitiator DETC with Irgacure-819

For an analysis of the influence of the photoinitiator on the scintillation effect, two different photoinitators were used to print a block on the same substrate. The sample is then investigated in the SEM under observation of emitted photons, see Figure A.10a. On the first look, the average 8-bit gray value from the block using Irgacure-819 as photoinitiator is 12.7 % higher than the one from the block with DETC as photoinitiator. However, for a full comparison also the emission wavelength needs to be taken into account. Therefore, Figure A.10b shows the fluorescence spectrum of the photoresist with Irgacure-819. Both, the peak emission wavelength as well as the average emission wavelength are blue shifted with respect to the emission wavelengths of the scintillator using DETC

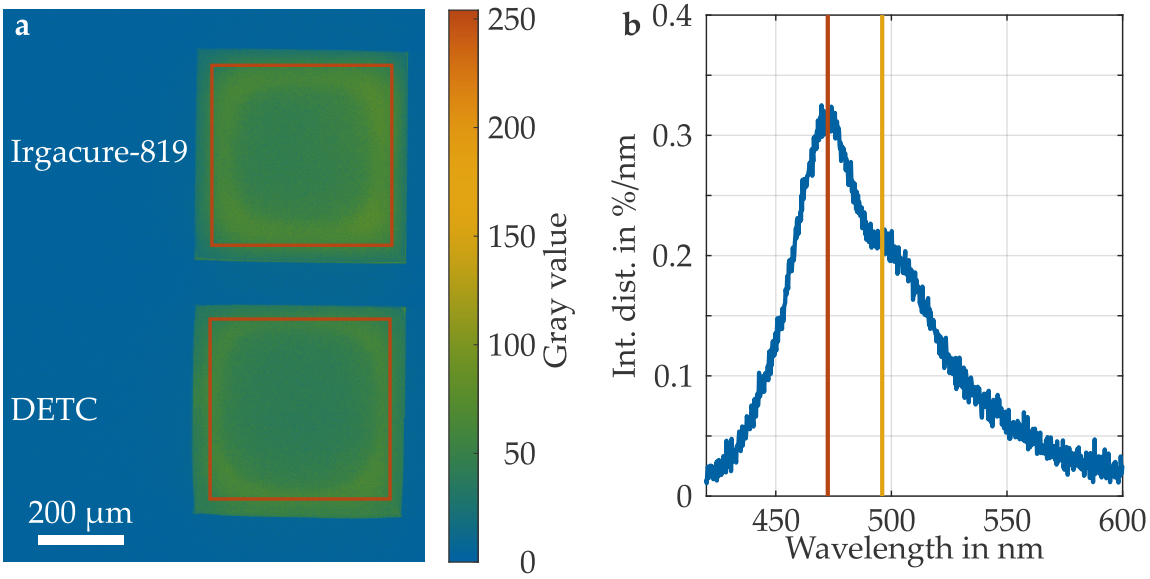

Figure A.10: Comparison of the scintillation performance between the two photoinitiators DETC and Irgacure-819. Panel **a** shows an SEM image obtained with an acceleration voltage of 8 kV from two printed scintillator blocks with DETC and Irgacure-819 as photoinitiator under the observation of emitted photons. The average 8-bit gray values of the pixels inside the marked squares are 55.3 for Irgacure-819 and 49.0 for DETC. The fluorescence emission spectrum of the photoresist with Irgacure-819 under illumination with 360 nm is shown in panel **b**. The peak wavelength (red line) is as 472.5 nm and the average emission wavelength (yellow line) at 496.0 nm. The figure was adapted from [94].

(see Figure 5.5 in Section 5.3.2). Comparing the spectral sensitivity of the VPSE detector as characterized in Section A.4, the sensitivity of peak wavelength of Irgacure-819 is 18.9 % higher than for the peak wavelength of DETC and 49.9 % for the average wavelengths respectively. Thus, the increase of the gray value can be fully explained by the wavelength dependency of the VPSE detector's sensitivity.

Interestingly, the photoinitiator does have an influence on the emission wavelength of the scintillator. Obviously it acts as an additional wavelength shifter shifting the light even more to the red. Thus, it is very important to use photoinitiators that do not introduce losses at this point and have a high quantum efficiency.

Bibliography

[1] H. J. Kimble, M. Dagenais, and L. Mandel, "Photon antibunching in resonance fluorescence", Physical Review Letters **39**, 691 (1977) (cited on page 3).

[2] I. Aharonovich, D. Englund, and M. Toth, "Solid-state single-photon emitters", Nature photonics **10**, 631–641 (2016) (cited on page 3).

[3] S. Castelletto, B. Johnson, V. Ivády, N. Stavrias, T. Umeda, A. Gali, and T. Ohshima, "A silicon carbide room-temperature single-photon source", Nature materials **13**, 151–156 (2014) (cited on page 3).

[4] T. T. Tran, K. Bray, M. J. Ford, M. Toth, and I. Aharonovich, "Quantum emission from hexagonal boron nitride monolayers", Nature nanotechnology **11**, 37–41 (2016) (cited on page 3).

[5] E. Synge, "XXXVIII. A suggested method for extending microscopic resolution into the ultra-microscopic region", The London, Edinburgh, and Dublin Philosophical Magazine and Journal of Science **6**, 356–362 (1928) (cited on page 3).

[6] X. Ma, Q. Liu, N. Yu, D. Xu, S. Kim, Z. Liu, K. Jiang, B. M. Wong, R. Yan, and M. Liu, "6 nm super-resolution optical transmission and scattering spectroscopic imaging of carbon nanotubes using a nanometer-scale white light source", Nature Communications **12**, 6868 (2021) (cited on page 3).

[7] Y. Oshikane, T. Kataoka, M. Okuda, S. Hara, H. Inoue, and M. Nakano, "Observation of nanostructure by scanning near-field optical microscope with small sphere probe", Science and Technology of Advanced Materials **8**, 181 (2007) (cited on page 3).

[8] S. W. Hell and J. Wichmann, "Breaking the diffraction resolution limit by stimulated emission: stimulated-emission-depletion fluorescence microscopy", Optics letters **19**, 780–782 (1994) (cited on page 3).

[9] T. A. Klar and S. W. Hell, "Subdiffraction resolution in far-field fluorescence microscopy", Optics letters **24**, 954–956 (1999) (cited on page 3).

[10] V. Petrik, V. Apok, J. A. Britton, B. A. Bell, and M. C. Papadopoulos, "Godfrey Hounsfield and the dawn of computed tomography", Neurosurgery **58**, 780–787 (2006) (cited on page 3).

[11] S.-R. Zhao and H. Halling, "A new Fourier method for fan beam reconstruction", in 1995 IEEE Nuclear Science Symposium and Medical Imaging Conference Record, Vol. 2 (IEEE, 1995), pp. 1287–1291 (cited on page 3).

[12] A. Burvall, U. Lundström, P. A. Takman, D. H. Larsson, and H. M. Hertz, "Phase retrieval in X-ray phase-contrast imaging suitable for tomography", Optics express **19**, 10359–10376 (2011) (cited on page 3).

[13] P. Kiefer, V. Hahn, S. Kalt, Q. Sun, Y. M. Eggeler, and M. Wegener, "A multi-photon (7×7)-focus 3D laser printer based on a 3D-printed diffractive optical element and a 3D-printed multi-lens array (submitted)", Light: Advanced Manufacturing (2023) (cited on pages 3, 32, 33, 73).

[14] V. Hahn, P. Kiefer, T. Frenzel, J. Qu, E. Blasco, C. Barner-Kowollik, and M. Wegener, "Rapid assembly of small materials building blocks (voxels) into large functional 3D metamaterials", Advanced Functional Materials **30**, 1907795 (2020) (cited on pages 3, 18).

[15] M. F. Groß, J. L. G. Schneider, Y. Wei, Y. Chen, S. Kalt, M. Kadic, X. Liu, G. Hu, and M. Wegener, "Tetramode metamaterials as phonon polarizers", Advanced Materials **35**, 2211801 (2023) (cited on pages 3, 18).

[16] F. Fan, Z. Feng, and C. Li, "UV Raman spectroscopic study on the synthesis mechanism and assembly of molecular sieves", Chemical Society Reviews **39**, 4794–4801 (2010) (cited on page 3).

[17] R. F. Kranenburg, F. A. van Geenen, G. Berden, J. Oomens, J. Martens, and A. C. van Asten, "Mass-spectrometry-based identification of synthetic drug isomers using infrared ion spectroscopy", Analytical Chemistry **92**, 7282–7288 (2020) (cited on page 3).

[18] N. Akkilic, S. Geschwindner, and F. Höök, "Single-molecule biosensors: Recent advances and applications", Biosensors and Bioelectronics **151**, 111944 (2020) (cited on page 3).

[19] P. Schanda and G. Haran, "NMR and Single-Molecule FRET Insights into Fast Protein Motions and Their Relation to Function", Annual Review of Biophysics **53** (2024) (cited on page 3).

[20] J. Martens, G. Berden, R. E. Van Outersterp, L. A. Kluijtmans, U. F. Engelke, C. D. Van Karnebeek, R. A. Wevers, and J. Oomens, "Molecular identification in metabolomics using infrared ion spectroscopy", Scientific reports **7**, 3363 (2017) (cited on page 3).

[21] D. Musumeci, C. Platella, C. Riccardi, F. Moccia, and D. Montesarchio, "Fluorescence sensing using DNA aptamers in cancer research and clinical diagnostics", Cancers **9**, 174 (2017) (cited on page 3).

[22] C. Kretschmer, A. Sterner-Kock, F. Siedentopf, W. Schoenegg, P. M. Schlag, and W. Kemmner, "Identification of early molecular markers for breast cancer", Molecular cancer **10**, 1–11 (2011) (cited on page 3).

[23] E. C. Le Ru and P. G. Etchegoin, "Single-molecule surface-enhanced Raman spectroscopy", Annual review of physical chemistry **63**, 65–87 (2012) (cited on page 3).

[24] G. Haran, "Single-molecule Raman spectroscopy: a probe of surface dynamics and plasmonic fields", Accounts of chemical research **43**, 1135–1143 (2010) (cited on page 3).

[25] Y. He, S. Su, T. Xu, Y. Zhong, J. A. Zapien, J. Li, C. Fan, and S.-T. Lee, "Silicon nanowires-based highly-efficient SERS-active platform for ultrasensitive DNA detection", Nano Today **6**, 122–130 (2011) (cited on page 3).

[26] Q. Ding, J. Wang, X. Chen, H. Liu, Q. Li, Y. Wang, and S. Yang, "Quantitative and sensitive SERS platform with analyte enrichment and filtration function", Nano letters **20**, 7304–7312 (2020) (cited on page 3).

[27] J.-A. Huang, M. Z. Mousavi, Y. Zhao, A. Hubarevich, F. Omeis, G. Giovannini, M. Schütte, D. Garoli, and F. De Angelis, "SERS discrimination of single DNA bases in single oligonucleotides by electro-plasmonic trapping", Nature Communications **10**, 5321 (2019) (cited on pages 3, 38).

[28] M. Iarossi, D. Darvill, A. Hubarevich, J.-A. Huang, Y. Zhao, A. F. De Fazio, D. B. O'Neill, F. Tantussi, and F. De Angelis, "High-Density Plasmonic Nanopores for DNA Sensing at Ultra-Low Concentrations by Plasmon-Enhanced Raman Spectroscopy", Advanced Functional Materials **33**, 2301934 (2023) (cited on pages 3, 38).

[29] Y. Zhao, A. Hubarevich, A. F. De Fazio, M. Iarossi, J.-A. Huang, and F. De Angelis, "Plasmonic Bowl-Shaped Nanopore for Raman Detection of Single DNA Molecules in Flow-Through", Nano Letters **23**, 4830–4836 (2023) (cited on pages 3, 38).

[30] Z. He, W. Qiu, M. E. Kizer, J. Wang, W. Chen, A. V. Sokolov, X. Wang, J. Hu, and M. O. Scully, "Resolving the sequence of RNA strands by tip-enhanced Raman spectroscopy", ACS Photonics **8**, 424–430 (2020) (cited on pages 3, 38).

[31] Y. Zhao, M. Iarossi, A. F. De Fazio, J.-A. Huang, and F. De Angelis, "Label-free optical analysis of biomolecules in solid-state nanopores: toward single-molecule protein sequencing", ACS photonics **9**, 730–742 (2022) (cited on pages 3, 38).

[32] N. Maccaferri, G. Barbillon, A. N. Koya, G. Lu, G. P. Acuna, and D. Garoli, "Recent advances in plasmonic nanocavities for single-molecule spectroscopy", Nanoscale Advances **3**, 633–642 (2021) (cited on pages 3, 38).

[33] W. Li, J. Zhou, N. Maccaferri, R. Krahne, K. Wang, and D. Garoli, "Enhanced optical spectroscopy for multiplexed DNA and protein-sequencing with plasmonic nanopores: Challenges and prospects", Analytical Chemistry **94**, 503–514 (2022) (cited on pages 3, 38).

[34] D. Garoli, H. Yamazaki, N. Maccaferri, and M. Wanunu, "Plasmonic nanopores for single-molecule detection and manipulation: toward sequencing applications", Nano letters **19**, 7553–7562 (2019) (cited on pages 3, 38).

[35] S. Maruo, O. Nakamura, and S. Kawata, "Three-dimensional microfabrication with two-photon-absorbed photopolymerization", Optics Letters **22**, 132–134 (1997) (cited on pages 4, 18).

[36] "Introducing Two-Photon Grayscale Lithography (White paper)", Nanoscribe GmbH & Co. KG (2021) (cited on pages 4, 21, 22).

[37] J. Weinacker, S. Kalt, P. Kiefer, P. Rietz, and M. Wegener, "On Iterative Pre-Compensation of 3D Laser-Printed Micro-Optical Components Using Confocal-Optical Microscopy", Advanced Functional Materials **34**, 2309356 (2024) (cited on pages 4, 9, 22, 24, 33, 40, 42, 43, 78, 79).

[38] P. B. Cushman and D.-M. Poehlmann, "Plastic Scintillator Detectors for Particle Physics", Plastic Scintillators: Chemistry and Applications, 541–588 (2021) (cited on pages 4, 56).

[39] K. Cankoçak, P. de Barbaro, D. Vishnevskiy, Y. Onel, O. behalf ofCMS-HCAL Collaboration, et al., "CMS HCAL installation and commissioning", in Journal of Physics: Conference Series, Vol. 160, 1 (IOP Publishing, 2009), p. 012055 (cited on pages 4, 56).

[40] F. Cavallari, "Performance of calorimeters at the LHC", in Journal of Physics: Conference Series, Vol. 293, 1 (IOP Publishing, 2011), p. 012001 (cited on pages 4, 56).

[41] P. Cortese, G. Dellacasa, R. Gemme, L. Ramello, M. Sitta, A. Ahmad, N. Ahmad, A. Danish, M. Irfan, A. Kamal, et al., "ALICE electromagnetic calorimeter technical design report", PhD thesis (-, 2008) (cited on pages 4, 56).

[42] A. A. Alves Jr, L. Andrade Filho, A. Barbosa, I. Bediaga, G. Cernicchiaro, G. Guerrer, H. Lima Jr, A. Machado, J. Magnin, F. Marujo, et al., "The LHCb detector at the LHC", Journal of instrumentation **3**, S08005 (2008) (cited on pages 4, 56).

[43] D. Michael, P. Adamson, T. Alexopoulos, W. Allison, G. Alner, K. Anderson, C. Andreopoulos, M. Andrews, R. Andrews, C. Arroyo, et al., "The magnetized steel and scintillator calorimeters of the MINOS experiment", Nuclear Instruments and Methods in Physics Research Section A: Accelerators, Spectrometers, Detectors and Associated Equipment **596**, 190–228 (2008) (cited on pages 4, 56).

[44] D. Ayres, G. Drake, M. Goodman, J. Grudzinski, V. Guarino, R. Talaga, A. Zhao, P. Stamoulis, E. Stiliaris, G. Tzanakos, et al., "The NOvA technical design report", (2007) (cited on pages 4, 56).

[45] L. Aliaga, O. Altinok, C. A. Del Castillo, L. Bagby, L. Bellantoni, W. Bergan, A. Bodek, R. Bradford, A. Bravar, H. Budd, et al., "MINERvA neutrino detector response measured with test beam data", Nuclear Instruments and Methods in Physics Research Section A: Accelerators, Spectrometers, Detectors and Associated Equipment **789**, 28–42 (2015) (cited on pages 4, 56).

[46] Y. Poirier, J. Xu, S. Mossahebi, F. Therriault-Proulx, and A. Sawant, "Characterization and practical applications of a novel plastic scintillator for online dosimetry for an ultrahigh dose rate (FLASH)", Medical Physics **49**, 4682–4692 (2022) (cited on pages 4, 56).

[47] P. Moskal and E. Stępień, "Prospects and clinical perspectives of total-body PET imaging using plastic scintillators", PET clinics **15**, 439–452 (2020) (cited on pages 4, 56).

[48] E. Timakova, M. Bazalova-Carter, and S. Zavgorodni, "Characterization of a 0.8 mm3 Medscint plastic scintillator detector system for small field dosimetry", Physics in Medicine & Biology **68**, 175040 (2023) (cited on pages 4, 56).

[49] E. Ciarrocchi, E. Ravera, A. Cavalieri, M. Celentano, D. Del Sarto, F. Di Martino, S. Linsalata, M. Massa, L. Masturzo, A. Moggi, et al., "Plastic scintillator-based dosimeters for ultra-high dose rate (UHDR) electron radiotherapy", Physica Medica **121**, 103360 (2024) (cited on pages 4, 56).

[50] Z. Lin, S. Lv, Z. Yang, J. Qiu, and S. Zhou, "Structured scintillators for efficient radiation detection", Advanced science **9**, 2102439 (2022) (cited on pages 4, 56).

[51] G. Konstantinou, L. Zhang, D. Bonifacio, R. Latella, J. M. Benlloch, A. J. Gonzalez, and P. Lecoq, "Semi-monolithic meta-scintillator simulation proof-of-concept, combining accurate DOI and TOF", IEEE Transactions on Radiation and Plasma Medical Sciences (2024) (cited on pages 4, 56).

[52] S. Kim and Y.-H. Seoung, "Fabrication and characterization of 3D printed polyvinyl toluene based plastic scintillator", Journal of the Korean Physical Society **75**, 953–956 (2019) (cited on pages 4, 56, 58, 62, 70).

[53] J. Son, D. G. Kim, S. Lee, J. Park, Y. Kim, T. Schaarschmidt, and Y. K. Kim, "Improved 3D printing plastic scintillator fabrication", Journal of the Korean Physical Society **73**, 887–892 (2018) (cited on pages 4, 56–58, 62, 70).

[54] D. G. Kim, K. Kim, S. Lee, and Y. K. Kim, "Enhanced characteristics of 3D-Printed plastic scintillators based on bisphenol fluorene diacrylates", Radiation Physics and Chemistry **198**, 110255 (2022) (cited on pages 4, 56, 58, 62, 70, 74).

[55] K. Gauda, S. Schneidewind, G. Drexlin, A. Fulst, V. Hannen, T. König, A. Lokhov, P. Oelpmann, H.-W. Ortjohann, W. Pernice, et al., "An active transverse energy filter to differentiate low energy particles with large pitch angles in a strong magnetic field", The European Physical Journal C **82**, 922 (2022) (cited on pages 4, 56, 66, 70).

[56] C. Roques-Carmes, N. Rivera, A. Ghorashi, S. E. Kooi, Y. Yang, Z. Lin, J. Beroz, A. Massuda, J. Sloan, N. Romeo, et al., "A framework for scintillation in nanophotonics", Science **375**, eabm9293 (2022) (cited on pages 4, 75).

[57] T. Anagnos, M. Trappen, B. C. K. Tiong, T. Feger, S. Yerolatsitis, R. J. Harris, J. Lozi, N. Jovanovic, T. A. Birks, S. Vievard, et al., "3D-M3: high-spatial-resolution spectroscopy with extreme AO and 3D-printed micro-lenslets", Applied Optics **60**, D108–D121 (2021) (cited on pages 8, 18).

[58] A. Kottaram Amrithanath and S. Krishnaswamy, "Efficient harnessing of light from nanoscale emitters deterministically placed through polymer-pen lithography at the focus of 3D-printed ellipsoidal micro-lenses", Optics Letters **46**, 4734–4737 (2021) (cited on pages 8, 18).

[59] K. Vanmol, A. Kandeel, G. Y. Belay, H. Thienpont, H. Ottevaere, and J. Van Erps, "Two-Photon Polymerization-based Direct Laser Writing and Characterization of Micro-Lenses for Optical Interconnect Applications", in 2021 26th Microoptics Conference (MOC) (2021), pp. 1–2 (cited on pages 8, 18).

[60] M. Schmid, F. Sterl, S. Thiele, A. Herkommer, and H. Giessen, "3D printed hybrid refractive/diffractive achromat and apochromat for the visible wavelength range", Optics Letters **46**, 2485–2488 (2021) (cited on pages 8, 18).

[61] S. Thiele, C. Pruss, A. M. Herkommer, and H. Giessen, "3D printed stacked diffractive microlenses", Optics Express **27**, 35621–35630 (2019) (cited on pages 8, 18).

[62] M. Malinauskas, A. Žukauskas, V. Purlys, K. Belazaras, A. Momot, D. Paipulas, R. Gadonas, A. Piskarskas, H. Gilbergs, A. Gaidukevičiūtė, et al., "Femtosecond laser polymerization of hybrid/integrated micro-optical elements and their characterization", Journal of Optics **12**, 124010 (2010) (cited on pages 8, 18).

[63] A. Žukauskas, M. Malinauskas, C. Reinhardt, B. N. Chichkov, and R. Gadonas, "Closely packed hexagonal conical microlens array fabricated by direct laser photopolymerization", Applied Optics **51**, 4995–5003 (2012) (cited on pages 8, 18).

[64] P. Somers, Z. Liang, J. E. Johnson, B. W. Boudouris, L. Pan, and X. Xu, "Rapid, continuous projection multi-photon 3D printing enabled by spatiotemporal focusing of femtosecond pulses", Light: Science & Applications **10**, 199 (2021) (cited on pages 8, 18).

[65] E. Hecht, P. Education, and K. Lippert, *Optik*, De Gruyter Studium (De Gruyter, 2023) (cited on page 9).

[66] *Optics and photonics-Preparation of draw- ings for optical elements and systems-Part 12: Aspheric surfaces*, Norm, Nov. 2019 (cited on page 10).

[67] M. F. Schumann, "Transformation optics for optoelectronic devices :" PhD thesis (Karlsruher Institut für Technologie (KIT), 2018) (cited on page 10).

[68] J. Weinacker, B. K. Bhandari, A. V. Rodriguez, C. West, F. De Angelis, F. Tantussi, N. Maccaferri, N. Goldman, and M. Wegener, "A protocol using compact 3D printed micro-optical elements for protein identification from low-intensity amino-acid Raman signals (under review)", Advanced Materials Technologies (2024) (cited on pages 11, 46, 47, 51, 53, 54, 81–84).

[69] P. Kiefer, "On Next-Generation Multi-Focus 3D Laser Printing", PhD thesis (Karlsruher Institut für Technologie (KIT), 2024), 175 pp. (cited on page 17).

[70] A. Marino, O. Tricinci, M. Battaglini, C. Filippeschi, V. Mattoli, E. Sinibaldi, and G. Ciofani, "A 3D real-scale, biomimetic, and biohybrid model of the blood-brain barrier fabricated through two-photon lithography", Small **14**, 1702959 (2018) (cited on page 18).

[71] M. Hippler, K. Weißenbruch, K. Richler, E. D. Lemma, M. Nakahata, B. Richter, C. Barner-Kowollik, Y. Takashima, A. Harada, E. Blasco, et al., "Mechanical stimulation of single cells by reversible host-guest interactions in 3D microscaffolds", Science advances **6**, eabc2648 (2020) (cited on page 18).

[72] R. Sun, X. Song, K. Zhou, Y. Zuo, R. Wang, O. Rifaie-Graham, D. J. Peeler, R. Xie, Y. Leng, H. Geng, et al., "Assembly of fillable microrobotic systems by microfluidic loading with dip sealing", Advanced Materials **35**, 2207791 (2023) (cited on page 18).

[73] G. von Freymann, "Recent progress and applications for 3D micro-printing", in Frontiers in Ultrafast Optics: Biomedical, Scientific, and Industrial Applications XXI, Vol. 11676 (SPIE, 2021), 116760A (cited on page 18).

[74] J. Lölsberg, J. Linkhorst, A. Cinar, A. Jans, A. J. Kuehne, and M. Wessling, "3D nanofabrication inside rapid prototyped microfluidic channels showcased by wet-spinning of single micrometre fibres", Lab on a Chip **18**, 1341–1348 (2018) (cited on page 18).

[75] Y. Chen, J. L. Schneider, M. F. Groß, K. Wang, S. Kalt, P. Scott, M. Kadic, and M. Wegener, "Observation of Chirality-Induced Roton-Like Dispersion in a 3D Micropolar Elastic Metamaterial", Advanced Functional Materials **34**, 2302699 (2024) (cited on page 18).

[76] T. Bückmann, M. Kadic, R. Schittny, and M. Wegener, "Mechanical metamaterials with anisotropic and negative effective mass-density tensor made from one constituent material", physica status solidi (b) **252**, 1671–1674 (2015) (cited on page 18).

[77] T. Frenzel, M. Kadic, and M. Wegener, "Three-dimensional mechanical metamaterials with a twist", Science **358**, 1072–1074 (2017) (cited on page 18).

[78] A. Kyriazis, K. Vanmol, G. Y. Belay, H. Thienpont, and J. Van Erps, "Design, laser direct writing prototyping, and characterization of fan-out diffractive optical elements for optical interconnect applications", in 3D Printed Optics and Additive Photonic Manufacturing III, Vol. 12135 (SPIE, 2022), pp. 30–38 (cited on page 18).

[79] H. Wang, H. Wang, W. Zhang, and J. K. Yang, "Toward near-perfect diffractive optical elements via nanoscale 3D printing", ACS nano **14**, 10452–10461 (2020) (cited on page 18).

[80] F. Seiboth, A. Kubec, A. Schropp, S. Niese, P. Gawlitza, J. Garrevoet, V. Galbierz, S. Achilles, S. Patjens, M. E. Stuckelberger, et al., "Rapid aberration correction for diffractive X-ray optics by additive manufacturing", Optics Express **30**, 31519–31529 (2022) (cited on page 18).

[81] J. Sandford O'Neill, P. Salter, Z. Zhao, B. Chen, H. Daginawalla, M. J. Booth, S. J. Elston, and S. M. Morris, "3D Switchable Diffractive Optical Elements Fabricated with Two-Photon Polymerization", Advanced Optical Materials **10**, 2102446 (2022) (cited on page 18).

[82] X. Porte, N. U. Dinc, J. Moughames, G. Panusa, C. Juliano, M. Kadic, C. Moser, D. Brunner, and D. Psaltis, "Direct (3+ 1) D laser writing of graded-index optical elements", Optica **8**, 1281–1287 (2021) (cited on page 18).

[83] V. Hahn, S. Kalt, G. M. Sridharan, M. Wegener, and S. Bhattacharya, "Polarizing beam splitter integrated onto an optical fiber facet", Optics express **26**, 33148–33157 (2018) (cited on page 18).

[84] H. Gao, G. F. Chen, P. Xing, J. W. Choi, H. Y. Low, and D. T. Tan, "High-resolution 3D printed photonic waveguide devices", Advanced Optical Materials **8**, 2000613 (2020) (cited on page 18).

[85] P. Kiefer, V. Hahn, M. Nardi, L. Yang, E. Blasco, C. Barner-Kowollik, and M. Wegener, "Sensitive photoresists for rapid multiphoton 3D laser micro-and nanoprinting", Advanced Optical Materials **8**, 2000895 (2020) (cited on page 18).

[86] T. Frenzel, "On 3D Chiral Mechanical Metamaterials", PhD thesis (Karlsruher Institut für Technologie (KIT), Karlsruhe, 2020) (cited on page 19).

[87] T. Aderneuer, O. Fernández, and R. Ferrini, "Two-photon grayscale lithography for free-form micro-optical arrays", Optics express **29**, 39511–39520 (2021) (cited on pages 20, 22).

[88] J. Weinacker, S. Kalt, P. Kiefer, P. Rietz, and M. Wegener, *Quandalf program*, (2023) https://gitlab.kit.edu/kit/aph/AGW/quandalf (visited on 10/11/2024) (cited on page 24).

[89] J. D'Errico, *inpaint_nans – File Exchange – MATLAB Central*, (2012) https://de.mathworks.com/matlabcentral/fileexchange/4551-inpaint_nans (visited on 07/31/2024) (cited on page 31).

[90] W. Commons, *Ramanscattering*, (2007) https://commons.wikimedia.org/wiki/File:Ramanscattering.svg (visited on 07/24/2024) (cited on page 36).

[91] *IP-S Tables*, https://support.nanoscribe.com/hc/en-gb/articles/360009156133-IP-S-Tables (visited on 08/01/2024) (cited on pages 41, 49, 73).

[92] A. Franzen, *Component Library*, (2006) http://www.gwoptics.org/ComponentLibrary/ (visited on 07/18/2024) (cited on pages 45, 52).

[93] B. K. Bhandari and N. Goldman, "A generalized protein identification method for novel and diverse sequencing technologies", NAR Genomics and Bioinformatics **6**, lqae126 (2024) (cited on page 48).

[94] J. Weinacker, S. Kalt, A. Huber, N. Gutknecht, J. L. G. Schneider, N. M. Bojanowski, T. Geigle, M. Steidl, and M. Wegener, "Multi-Photon 3D Laser Micro-Printed Plastic Scintillators for Applications in Low-Energy Particle Physics", Advanced Functional Materials, 2413215 (2024) (cited on pages 55–57, 63–65, 67, 86, 89, 90).

[95] H. Yang, G. Luo, T. Yu, S. Zhao, B. Hu, Z. Huang, H. Shen, L. Yang, Y. Chen, and J. Tang, "MuGrid: A scintillator detector towards cosmic muon absorption imaging", Nuclear Instruments and Methods in Physics Research Section A: Accelerators, Spectrometers, Detectors and Associated Equipment **1042**, 167402 (2022) (cited on page 56).

[96] G. Konstantinou, P. Lecoq, J. M. Benlloch, and A. J. Gonzalez, "Metascintillators for ultrafast gamma detectors: A review of current state and future perspectives", IEEE Transactions on Radiation and Plasma Medical Sciences **6**, 5–15 (2021) (cited on page 56).

[97] *Nanoguide*, https://support.nanoscribe.com/hc/en-gb (visited on 08/20/2024) (cited on pages 58, 61).

[98] C. Buck, B. Gramlich, M. Lindner, C. Roca, and S. Schoppmann, "Production and properties of the liquid scintillators used in the STEREO reactor neutrino experiment", Journal of Instrumentation **14**, P01027 (2019) (cited on page 64).

[99] M. L. Juan, M. Righini, and R. Quidant, "Plasmon nano-optical tweezers", Nature photonics **5**, 349–356 (2011) (cited on page 73).

[100] J. C. Ndukaife, Y. Xuan, A. G. A. Nnanna, A. V. Kildishev, V. M. Shalaev, S. T. Wereley, and A. Boltasseva, "High-resolution large-ensemble nanoparticle trapping with multifunctional thermoplasmonic nanohole metasurface", ACS nano **12**, 5376–5384 (2018) (cited on page 73).

[101] S. Kerman, C. Chen, Y. Li, W. Van Roy, L. Lagae, and P. Van Dorpe, "Raman fingerprinting of single dielectric nanoparticles in plasmonic nanopores", Nanoscale **7**, 18612–18618 (2015) (cited on page 73).

[102] J. Canning, C. Clark, M. Dayao, D. de LaMela, M. Logozzo, and J. Zhao, "Anti-reflection coatings on 3D-printed components", Coatings **11**, 1519 (2021) (cited on page 73).

[103] L. Grineviciute, C. Babayigit, D. Gailevičius, M. Peckus, M. Turduev, T. Tolenis, M. Vengris, H. Kurt, and K. Staliunas, "Nanostructured multilayer coatings for spatial filtering", Advanced Optical Materials **9**, 2001730 (2021) (cited on page 73).

[104] L. Grineviciute, J. Nikitina, C. Babayigit, and K. Staliunas, "Fano-like resonances in nanostructured thin films for spatial filtering", Applied Physics Letters **118** (2021) (cited on page 73).

[105] D. Astrauskytė, K. Galvanauskas, D. Gailevičius, M. Drazdys, M. Malinauskas, and L. Grineviciute, "Anti-reflective coatings produced via atomic layer deposition for hybrid polymer 3D micro-optics", Nanomaterials **13**, 2281 (2023) (cited on page 73).

[106] S. Ristok, P. Flad, and H. Giessen, "Atomic layer deposition of conformal anti-reflective coatings on complex 3D printed micro-optical systems", Optical Materials Express **12**, 2063–2071 (2022) (cited on page 73).

[107] *IP-Visio*, https://support.nanoscribe.com/hc/en-gb/articles/360011709499-IP-Visio (visited on 08/30/2024) (cited on page 73).

[108] *IP-n162*, https://support.nanoscribe.com/hc/en-gb/articles/360016675899-IP-n162 (visited on 08/30/2024) (cited on page 73).

[109] M. Hasan and S. Blair, "Maximizing transmittance in two-photon 3D printed materials for micro-optics in the visible", Optical materials express **12**, 895–906 (2022) (cited on page 73).

[110] J. Bauer, C. Crook, and T. Baldacchini, "A sinterless, low-temperature route to 3D print nanoscale optical-grade glass", Science **380**, 960–966 (2023) (cited on page 73).

[111] F. Kotz, A. S. Quick, P. Risch, T. Martin, T. Hoose, M. Thiel, D. Helmer, and B. E. Rapp, "Two-photon polymerization of nanocomposites for the fabrication of transparent fused silica glass microstructures", Advanced Materials **33**, 2006341 (2021) (cited on page 73).

[112] X. Wen, B. Zhang, W. Wang, F. Ye, S. Yue, H. Guo, G. Gao, Y. Zhao, Q. Fang, C. Nguyen, et al., "3D-printed silica with nanoscale resolution", Nature Materials **20**, 1506–1511 (2021) (cited on page 73).

[113] J. Köpfler, T. Frenzel, J. Schmalian, and M. Wegener, "Fused-Silica 3D Chiral Metamaterials via Helium-Assisted Microcasting Supporting Topologically Protected Twist Edge Resonances with High Mechanical Quality Factors", Advanced Materials **33**, 2103205 (2021) (cited on page 73).

[114] Y. Yao, M. Docter, J. Van Ginkel, D. De Ridder, and C. Joo, "Single-molecule protein sequencing through fingerprinting: computational assessment", Physical biology **12**, 055003 (2015) (cited on pages 74, 80).

[115] V. Hahn, T. Messer, N. M. Bojanowski, E. R. Curticean, I. Wacker, R. R. Schröder, E. Blasco, and M. Wegener, "Two-step absorption instead of two-photon absorption in 3D nanoprinting", Nature Photonics **15**, 932–938 (2021) (cited on page 75).

[116] X. Liu, C. Ding, X. Gao, X. Shen, M. Tang, Z. Yang, L. Xu, C. Kuang, and X. Liu, "High-resolution 3D nanoprinting based on two-step absorption via an integrated fiber-coupled laser diode", Optics Letters **48**, 4300–4303 (2023) (cited on page 75).

[117] T. Messer, M. Hippe, J. L. Gao, and M. Wegener, "A shoe-box-sized 3D laser nanoprinter based on two-step absorption", Light: Advanced Manufacturing **5**, 269–276 (2024) (cited on page 75).

[118] J. Fischer and M. Wegener, "Three-dimensional optical laser lithography beyond the diffraction limit", Laser & Photonics Reviews **7**, 22–44 (2013) (cited on page 75).

[119] J. Fischer and M. Wegener, "Three-dimensional direct laser writing inspired by stimulated-emission-depletion microscopy", Optical Materials Express **1**, 614–624 (2011) (cited on page 75).

Acknowledgments

At this point I want to take the chance to thank all the people that supported me directly or indirectly during my research for this thesis. Without this support, it would not have been possible for me to complete the tasks I presented on these pages.

At first, I would like to thank Prof. Dr. Martin Wegener for supervising me during my PhD thesis. He gave me the opportunity to join the cluster of excellence 3D matter made to order, which enabled me to meet many interesting people and learn a lot about different research topics around 3D printing. Additionally, his advises, during the group meeting, but also whenever necessary, were essential for me to complete my thesis.

Next, I want to thank Prof. Dr. Carsten Rockstuhl for being the co-referee of my PhD thesis. Additionally, during my mentoring committee meeting, his comments and questions were a very useful and interesting input during my writing period.

Now, I want to give credit to Prof. Dr. Francesco De Angelis, Dr. Francesco Tantussi, and Dr. Michele Dipalo for the management and organization of the EU project ProID which did not only give me founding, but also a great opportunity to work in a project with many contributor and aiming at a useful application. The discussions were always very constructive and helpful for my decisions how to approach the issues on my way. I am looking forward to see the final results of the work done by all of us within the project.

During the end phase of my thesis, I visited the research group of Prof. Dr. Nicolò Maccaferri in Umeå for the testing experiments of the SROE. I performed the experiments with Alba Viejo Rodriguez in the lab and I want to thank both of them for the intense support during these days. At this point, I also want to thank the rest of Nicolò's research group for the warm welcome in Sweden.

In addition to the experiments, the support from the theoretical side was also very important for me. Therefore, I want to acknowledge the work of Bikash Kumar Bhandari and Prof. Dr. Nick Goldman, who supported me by performing the optimization of the spectral regions for the amino acid discrimination. Additionally, I

want to point out the easy and comfortable communication with both of them.

Concerning the scintillator project, I want to thank Prof. Dr. Guido Drexlin for the initiation of this interesting topic. I want to point out the huge support I got from Sebastian Kalt, Dr. Maximilian Bojanowski, and Dr. Anton Huber during the work in the lab. I am very happy that we got nice results out of this project even though it will probably not be used in the KARTIN experiment. I also want to thank all other people from the research group of Guido Drexlin, who worked on this project.

Next, I want to acknowledge all the done paperwork by the institute's secretary, namely Petra Bauer, Gloria Zanda, Ursula Mösle, and Monika Brenkmann. Without their support in organizing all the bureaucracy work, I would not have been able to do so many thing that contributed to my thesis.

For the technical support, I want to thank Johann Westhauser, our institute's technician. Additionally, I thank the mechanical workshop, organized by Frank Landhäuser and later Maik Nothdurft, who made uncountable mechanical parts necessary for my experiments. This work would not have been possible without such competent and fast mechanical support.
On the other hand, also the electronics workshop was essential for my work. Here, I want to thank Michael Hippe, Helmut Lay, and Werner Gilde for the fabrication of small electronic components, like the LED board for characterizing the VPSE detector, as well as the maintenance of the IT infrastructure, which was the basis of my thesis.

Furthermore, I am very thankful to all people that helped me improving this thesis through proofreading. Namely, I want to mention Dr. Pascal Kiefer, Sebastian Kalt, Jonathan Schneider, and Pascal Rietz. I am pretty sure that your comments improved the readability and understandability of this work a lot.
Naturally, I want to thank the rest of the group members too. It was a pleasure to work with all of you and I will always remember the constructive discussions about research topics, as well as our private events. Here, I want to point out the fruitful programming sessions I had together with Pascal Kiefer, Sebastian Kalt, and Pascal Rietz when developing out precompensation program we named Quandalf. Especially the support from Sebastian Kalt for making SEM images from the micro-lens array samples contributed to this work. These sessions were a very pleasant time for me I will always like to remember.

Finally, I want to thank the people in my private surrounding, supporting me at any time and strengthen me during hard times. Your impact on this thesis is probably larger, than one might think. Namely, I want to point out my parents, Susanne

and Rudi Weinacker, and my brother, Florian Weinacker, who were always open for discussions and advice, even about my research topics, if possible. I am very happy to have people around my, I can share such thoughts with. Additionally, I want to thank my girlfriend, Julia Vautz, for the moral boot I sometimes needed during lean periods of the end phase of my thesis.